

# Unsteady aerodynamics and optimal control of an airfoil at low Reynolds number

Thesis by

Jeesoon Choi

In Partial Fulfillment of the Requirements

for the Degree of

Doctor of Philosophy

The logo for the California Institute of Technology, featuring the word "Caltech" in a bold, orange, sans-serif font.

California Institute of Technology

Pasadena, California

2016

(Defended April 14 2016)

© 2016

Jeesoon Choi

All Rights Reserved

# Acknowledgements

I am more than grateful for the opportunity and support that were given by my family, mentors, friends, and coworkers, which enabled me to stand where I am. Among many others, I would like to greatly acknowledge my advisor, professor Tim Colonius, for his guidance, patience, and encouragement during my graduate program. It was my fortune to work with an enthusiastic and optimistic mentor who have motivated me to stay focussed on my research. With his guidance, I was able to experience the diverse aspects of research and enjoy my graduate studies. I would also like to express my gratitude to Professors Beverley McKeon, David Williams, and Guillaume Blanquart for serving as committee members and also providing with the constructive comments that have enhanced the quality of this thesis.

During my stay in Caltech, I was very fortunate to collaborate with many researchers. Professor David Williams guidance on unsteady aerodynamics and helpful feedback during the meetings and email discussions have enlarged the spectrum of our research. Thanks are also due to Dr. Thibault Flinois for developing the frameworks of the adjoint optimal control code, and to Dr. Thierry Jardin for his useful comments regarding vortex dynamics.

I would also like to thank the members of our computational flow physics group: Oliver Schmidt, George Rigas, Vedran Coralic, Sebastian Liska, Mathew Inkman, Jomela Meng, Aaron Towne, Hsieh-Chen Tsai, Ed Burns, Andres Goza, Jay Qi, Kazuki Maeda, Phillippe Tosi, and André Fernando de Castro da Silva. I truly value the time we spent in our offices and I will miss it.

Also, thanks to my Korean friends: Hyoung Jun Ahn, Seyoon Kim, Yonil Jung, Min Seok Jang, Seung Ah Lee, Kun Woo Kim, Kiyoul Yang, Mooseok Jang, Taeyong Kim, and others. Your company has made my life in Caltech and K-town most enjoyable.

Financial support from the Gwanjeoung Educational Foundation and the Air Force of Scientific Research are gratefully acknowledged.

Last, but most important, I would like to express my deepest gratitude to my parents, Jongho Choi and Eunsil An, for their endless support. Also, thanks to my little brother Jimmy Choi.

# Abstract

As opposed to conventional air vehicles that have fixed wings, small birds and insects are known to flap their wings at higher angles of attack. The vortex produced at the tip of the wing, known as the leading-edge vortex (LEV), plays an important role to enhance lift during its flight. In this thesis, we analyze the influence of these vortices on aerodynamic forces that could be beneficial to micro-air vehicle performance and efficiency. The flow structures associated with simple harmonic motions of an airfoil are first investigated. The characteristics of the time-averaged and fluctuating forces are explained by analyzing vortical flow features, such as vortex lock-in, leading-edge vortex synchronization, and vortex formation time. Specific frequency regions where the wake instability locks in to the unsteady motion of the airfoil are identified, and these lead to significant changes in the mean forces. A detailed study of the flow structures associated with the LEV acting either in- or out-of-phase with the quasi-steady component of the forces is performed to quantify the amplification and attenuation behavior of the fluctuating forces. An inherent time scale of the LEV associated with its formation and detachment (LEV formation time) is shown to control the time-averaged forces. With these results, several optimal flow control problems are formulated. Adjoint-based optimal control is applied to an airfoil moving at a constant velocity and also to a reciprocating airfoil with no forward velocity. In both cases, we maximize lift by controlling the pitch rate of the airfoil. For the former case, the static map of lift at various angles of attack is additionally examined to find the static angle that provides maximum lift and also to confirm whether the optimizations perform according to the static map. For the latter case, we obtain a solution of the optimized motion of the flapping airfoil which resembles that of a hovering insect.

# Published content

The material presented in chapter 3 is based on the following publications:

1. Choi, J., Colonius, T. & Williams, D., R. 2013 Dynamics and energy extraction of a surging and plunging airfoil at low Reynolds number. *AIAA paper* 2013-0672.

DOI: <http://dx.doi.org/10.2514/6.2013-672>

2. Choi, J., Colonius, T. & Williams, D., R. 2015 Surging and plunging oscillations of an airfoil at low Reynolds number. *Journal of Fluid Mechanics* **763**, 237-253.

DOI: <http://dx.doi.org/10.1017/jfm.2014.674>

# Contents

<b>Acknowledgements</b>	<b>iii</b>
<b>Abstract</b>	<b>v</b>
<b>Published content</b>	<b>vi</b>
<b>List of Figures</b>	<b>x</b>
<b>List of Tables</b>	<b>xvi</b>
<b>Nomenclature</b>	<b>xvii</b>
<b>1 Introduction</b>	<b>1</b>
1.1 Energy extraction and unsteady aerodynamics at low Reynolds number . . . . .	2
1.2 Flow models of unsteady aerodynamics . . . . .	4
1.3 Application to flow control problems . . . . .	8
1.4 Thesis outline . . . . .	10
<b>2 Numerical Methods</b>	<b>12</b>
2.1 Immersed boundary fractional step method . . . . .	12
2.2 Adjoint-based optimal control . . . . .	17
2.2.1 Optimal control theory . . . . .	17
2.2.2 Optimization procedure . . . . .	20
2.2.3 Gradient derivations . . . . .	22
2.2.3.1 Basic definitions . . . . .	22

2.2.3.2	Adjoint equations . . . . .	26
2.2.3.3	Gradients . . . . .	32
<b>3</b>	<b>Low-Amplitude Surging and Plunging Airfoils</b>	<b>33</b>
3.1	Problem description . . . . .	33
3.2	Surging . . . . .	37
3.2.1	Vortex lock-in and time-averaged lift . . . . .	37
3.2.2	The leading-edge vortex and fluctuating lift . . . . .	38
3.2.3	LEV growth and detachment . . . . .	46
3.3	Plunging . . . . .	48
3.3.1	Time-averaged lift . . . . .	48
3.3.2	Fluctuating lift . . . . .	50
3.4	Summary . . . . .	52
<b>4</b>	<b>High-Amplitude Surging Airfoils</b>	<b>55</b>
4.1	Problem description . . . . .	55
4.2	Features of non-oscillatory flows at different $Re$ ( $\sigma_x = 0$ ) . . . . .	57
4.3	Forces and flow fields . . . . .	60
4.4	Mechanism of mean lift enhancement . . . . .	61
4.5	Square waveform streamwise velocity . . . . .	69
4.6	Summary . . . . .	74
<b>5</b>	<b>Optimal Control of an Airfoil</b>	<b>78</b>
5.1	Test problem . . . . .	78
5.2	Flapping flight . . . . .	81
<b>6</b>	<b>Concluding Remarks</b>	<b>88</b>
6.1	Summary and conclusions . . . . .	88
6.2	Suggestions for future work . . . . .	90

<b>A</b>	<b>Flow fields of rigid body motion in non-inertial frame of reference</b>	<b>92</b>
<b>B</b>	<b>Checkpointing algorithm</b>	<b>95</b>
	<b>Bibliography</b>	<b>97</b>

# List of Figures

1.1	Real, $F(k)$ , and Imaginary, $G(k)$ , part of the Theodorsen's function, $C(k)$ . . . . .	5
1.2	Fluctuating amplitude (left) and phase (right) of lift relative to velocity. The results of Greenberg's model (Greenberg, 1947) and the discrete-vortex model (DVM) from Tchieu & Leonard (2011) are presented. . . . .	6
2.1	Flow diagram of the gradient-based optimization procedure, and a comparison of the convergence of conjugate gradient method (red line) with steepest decent method (green line). . . . .	21
2.2	Free body diagram of an airfoil with an actuator near the trailing edge. Gravity and resultant fluid force are depicted. . . . .	25
3.1	Hopf bifurcation at $Re_{\text{crit}} = 254$ (simulation). Fluctuating ranges (gray area) and mean values (dashed line) are shown for $250 < Re < 290$ . Flat plate, $\alpha = 15^\circ$ . . . . .	36
3.2	Critical Reynolds numbers ( $Re_{\text{crit}}$ ) and corresponding vortex shedding reduced frequencies ( $k_{\text{VS, crit}}$ ) at different angles of attack. The subscript $p$ refers to quantities made dimensionless by the projected chord length, $c \sin \alpha$ . . . . .	36
3.3	Representative cases with (left and right) and without (center) lock-in. Surging amplitude is $\sigma_x = 0.05$ and the phase plot of lift coefficient and x-velocity are shown with the frequency spectra for 50 periods of surging frequency, $k$ . Flat plate, $Re = 300$ , $\alpha = 15^\circ$ and $k_{\text{VS}} = 1.62$ . . . . .	38
3.4	Lock-in regions (left) and mean lift force (right) for a surging airfoil at $Re = 300$ and $\alpha = 15^\circ$ . Lock-in regions are defined where $\gamma < 10^{-2}$ . $L_0$ is the mean lift for $\sigma_x = 0$ . . . . .	39

3.5	Time-averaged lift for $0.1 < \sigma_x < 0.8$ . Vertical line indicates the vortex shedding frequency of steady flow ( $\sigma_x = 0$ ). Flat plate, $\alpha = 15^\circ$ , $Re = 300$ . . . . .	39
3.6	Fluctuating amplitude of lift. Aerodynamic response is nearly independent of $\sigma_x$ for $\sigma_x \leq 0.2$ . Vertical line indicates the vortex shedding frequency of steady flow ( $\sigma_x = 0$ ). Flat plate, $\alpha = 15^\circ$ , $Re = 300$ . . . . .	40
3.7	Amplitude (left) and phase (right) of the fluctuating lift at various $Re$ and $\alpha$ . Simulation results (S), $Re \in [100, 500]$ , are compared with the experiment results (E), $Re = 57,000$ . Vertical lines indicate the vortex shedding frequency of steady flow ( $\sigma_x = 0$ ) at corresponding $Re$ . Airfoil is a flat plate for the simulations and NACA 0006 for experiments. $\sigma_x$ was set to 0.1 for all cases. . . . .	42
3.8	Snapshots of flow field at $Re = 500$ (left, simulation) and $Re = 57,000$ (right, experimental) for $\alpha = 20^\circ$ and $\sigma_x = 0.1$ . Top and bottom rows correspond to the flow field at the maximum $u = U(1 + \sigma_x)$ and minimum $u = U(1 - \sigma_x)$ velocity, respectively. Reduced frequencies are chosen to reveal flow fields when the fluctuations are amplified ( $k = 0.7$ ) and attenuated ( $k = 1.2$ ). For the simulations, streaklines are depicted on top of the color contours of vorticity, $\omega c/U \in [-10, 10]$ . . . . .	43
3.9	Vorticity contours and velocity vectors at various Reynolds number. Left and right columns shows the flow field at the maximum $u = U(1 + \sigma_x)$ , and minimum $u = U(1 - \sigma_x)$ velocity, respectively. $\alpha = 15^\circ$ , $\sigma_x = 0.2$ and $k = 0.5$ . . . . .	44
3.10	Same as figure 3.9 but at $k = 1.26$ . . . . .	45
3.11	Strength of maximum shed LEV and its occurring phase. Snapshots reveal the strength and size decreasing with increasing $k$ . Flat plate, $\alpha = 15^\circ$ , $Re = 300$ and $\sigma_x = 0.2$ . $\omega c/U \in [-10, 10]$ . . . . .	47

3.12	Streamlines (dashed lines), streaklines (solid lines), and stagnation points (diamond symbols) on the upper surface are plotted on top of vorticity contours at the maximum velocity, $u = U(1 + \sigma_x)$ , for $k = 0.25, 0.5, 0.78$ , and $1.26$ . For each case, vorticity values on the upper surface during the advancing portion of the motion are plotted on the right. Flat plate, $Re = 300, \alpha = 15^\circ$ , and $\sigma_x = 0.2$ . $\omega c/U \in [-10, 10]$ . Flat plate is rotated $15^\circ$ to align its chord with the x-axis. . . . .	49
3.13	Lock-in regions (left) and mean lift force (right) for $Re = 300$ and $\alpha = 15^\circ$ . $L_0$ is the mean lift for $\sigma_y = 0$ . . . . .	50
3.14	Time-averaged lift for $0.1 < \sigma_y < 0.8$ . Vertical line indicates the vortex shedding frequency of steady flow ( $\sigma_y = 0$ ). Flat plate, $\alpha = 15^\circ, Re = 300$ . . . . .	51
3.15	Fluctuating amplitude of lift at various reduced frequencies, $k$ . Flat plate, $\alpha = 15^\circ$ and $\sigma_y = 0.05$ . . . . .	52
3.16	Fluctuating amplitude of lift (plunging). Aerodynamic response is nearly linear for $\sigma_y = 0.2$ . Vertical lines indicate the vortex shedding frequency of steady flow ( $\sigma_y = 0$ ). Flat plate, $\alpha = 15^\circ, Re = 300$ . . . . .	53
4.1	The square box near the leading edge is enlarged to show control volume geometry (region inside the dotted line) and vorticity flux of $\omega < 0$ through the control surface. Flat plate, $\alpha = 20^\circ, k = 0.5, \sigma = 0.4$ at $Re = 1000$ . . . . .	57
4.2	Lift spectrum of uniform flow at $\alpha = 20^\circ$ . $\hat{C}_L$ is the magnitude of the Discrete-Fourier Transform of the fluctuating lift coefficient. The red dashed line corresponds to a frequency of $St_{VS} = fc \sin \alpha / U = 0.2$ . . . . .	58
4.3	Time history of lift coefficient at $Re = 100, 500$ , and $1000$ . . . . .	59
4.4	Mean drag (left) and lift (right) coefficients of uniform flow at $\alpha = 20^\circ$ . . . . .	59

4.5 Time-averaged lift coefficient,  $\bar{C}_L$ , of streamwise oscillating flow at various reduced frequencies ( $\alpha = 20^\circ$ ). Simulation (S) are run at  $Re = 1000$  and compared with experimental data (E) from Gursul & Ho (1992),  $Re = 5 \times 10^4$ . Dashed line corresponds to the frequency of maximum lift of experiment results (at  $k = 0.8$ ). The time-averaged lift coefficient of uniform flow at  $Re = 1000$  is  $\bar{C}_{L0} = 1.15$ . . . . . 60

4.6 Snapshots of flow fields at  $Re = 1000$  (top, simulation) and  $Re = 50,000$  (bottom, experimental) for  $\sigma_x = 0.7$ . The reduced frequencies for the simulation and experiment are  $k = 0.75$  and  $k = 0.7$ , respectively. The maximum velocity,  $u_{\max} = U(1 + \sigma_x)$ , occurs at  $t/T = 0.25$  and the minimum velocity,  $u_{\min} = U(1 - \sigma_x)$ , at  $t/T = 0.75$ . Vorticity contours and streamlines are compared to experimental flow visualizations (Gursul & Ho, 1992).  $\omega c/U \in [-20, 20]$ . . . . . 61

4.7 Time history of lift coefficient,  $C_L$ , for 2 oscillating periods of the motion. Increasing sequence of reduced frequency from  $k = 0.25$  to  $k = 0.75$ .  $u'$  is the fluctuating velocity of the airfoil's motion.  $\alpha = 20^\circ$ ,  $Re = 1000$ , and  $\sigma_x = 0.4$ . . . . . 64

4.8 Corresponding flow field of figure 4.7.  $\omega c/U \in [-20, 20]$ . . . . . 65

4.9 LEV formations during the advancing period.  $\alpha = 20^\circ$ ,  $Re = 1000$  and  $\sigma_x = 0.4$ . . . . 66

4.10 The dynamic formation time,  $T_{df}$ , at various  $\sigma_x$ . The dynamic formation time is measured from the start of the advancing phase, i.e.,  $t_0 = 0$ . . . . . 67

4.11 LEV formation time,  $T^*$ , is measured at various reduced frequencies (blue circle line). The formation time evaluated using the period of the motion,  $\pi/k$ , is also shown as the upper bound (black solid line). Flat plate,  $\alpha = 20^\circ$  and  $\sigma = 0.4$  at  $Re = 1000$ . . . . . 68

4.12 Total and max LEV circulation at various reduced frequencies. Flat plate,  $\alpha = 20^\circ$  and  $\sigma = 0.4$  at  $Re = 1000$ . Circulation is non-dimensionalized as  $\Gamma^* = \Gamma/Uc$ . For the range of  $0.38 < k < 1$ , the LEV is grown to its maximum strength and the rest of the total vorticity is analogous to the vortices in the trailing jet in the vortex ring case (Gharib *et al.*, 1998). . . . . 69

4.13	Flow fields shown as a series of increasing convective time, $tU/c$ , for $k = 0.25$ , $k = 0.5$ , and $k = 0.75$ . Time is measured from the start of the advancing motion. Left and right pointed arrows indicate the advancing and retreating portion of the period, respectively. Double horizontal line is associated with the LEV formation time, which occurs at $3 < T^* < 4$ . Single horizontal line indicates the end of one period of the motion. $\alpha = 20^\circ$ , $Re = 1000$ , and $\sigma_x = 0.4$ . . . . .	70
4.14	Same as figure 4.13, but at $k = 1$ , 1.25, and 2.01. . . . .	71
4.15	Sinusoidal and square waveform of streamwise velocity. $\sigma_x = 0.4$ . . . . .	72
4.16	Time-averaged lift coefficient, $\bar{C}_L$ . Black solid line shows the result obtained using the square waveform streamwise velocity. . . . .	73
4.17	Time history of lift coefficient at various reduced frequencies. Only the advancing portion of the period, $0 < t/T < 0.5$ , is shown. . . . .	74
4.18	Same as figure 4.19, but with square waveform of streamwise velocity. Results are shown at $k = 0.25$ , 0.5, and 0.63. . . . .	75
4.19	Same as figure 4.19, but with square waveform of streamwise velocity. Results are shown at $k = 0.75$ , 1, and 1.51. . . . .	76
5.1	Schematic of the test problem. Flat plate moving at a constant velocity, $U$ , with the rotational axis located 0.3 chord length from the leading-edge. $\Omega$ is the angular velocity of the body. . . . .	79
5.2	Drag and lift coefficient of uniform flow at various angles of attack. Shaded region shows the range of values, and the dash line, the average. Flat plate, $Re = 500$ . Aerodynamic forces measured at every $2^\circ$ . Transition from a stable equilibrium to periodic vortex shedding occurs at $10^\circ$ . . . . .	79

5.3	Optimization results of a flat plate at $\alpha = 0^\circ$ (black), $15^\circ$ (red), $30^\circ$ (green), and $60^\circ$ (blue). Angle of attack (left) and lift coefficient (right) is plotted as a function of time. Dashed line indicates the case before control and solid line, after. Optimization leads the airfoil to rotate towards the angle that maximizes lift, which is near $45^\circ$ . Control time horizon, $T$ , is 40 convective time units. . . . .	80
5.4	Flapping motion of a wing element in 2D. Downstroke phase indicated by the dotted line and upstroke by the solid line. The stroke plane is inclined at an angle $\beta$ , with an amplitude of $A_0$ . $a$ is the distance of the rotating axis from the leading edge, and $\alpha$ , the pitch angle. . . . .	83
5.5	Flapping motions before (left) and after (right) optimization. . . . .	84
5.6	Vorticity field of the optimized wing motion at $\beta = 0^\circ$ . . . . .	85
5.7	Time history of the vertical force coefficient, $C_y$ , for the optimized result of $\beta = 0^\circ$ . Dashed line indicates the data before optimization, and solid line, after. Shaded region indicates the stroke moving from right to left. . . . .	86
5.8	Time history of power, $P$ , for the optimized result of $\beta = 0^\circ$ . Shaded region indicates the stroke moving from right to left. . . . .	87
A.1	Coordinate systems of fixed (inertial) and (non-inertial) rotating frame or reference. . . . .	92
B.1	Checkpointing algorithm developed by Wang <i>et al.</i> (2009). Evolution of the algorithm assuming a total of 25 time steps. 5 checkpoints are assigned to save the forward variables. Copyright ©2009 Society for Industrial and Applied Mathematics. Reprinted with permission. . . . .	96

# List of Tables

- 5.1 Summary of optimization results.  $\bar{C}_L$  is the time-averaged lift coefficient after control, and  $\bar{C}_{L0}$  before. The integrated control cost is defined as  $\int_0^T Q_R \Omega^2 dt$ , and reference lift coefficient normalized as  $C_{L,\text{ref}} = 2F_{L,\text{ref}}/\rho U^2 c$ .  $T$  is the control horizon. . . . . 81
- 5.2 Summary of optimization results.  $A_0 = 2.5c$ ,  $a = 0.3c$ , and  $Re = 100$  for all cases. Time-averaged normalized forces,  $\bar{C}_x = 2F_x/(\rho U^2 c)$ , and  $\bar{C}_y = 2F_y/(\rho U^2 c)$ , in the x and y direction are given, respectively. Time-averaged power is also presented in the table, where  $\bar{P}$  includes both the rotational and translational power. The subscript with 0 indicates the values for cases before optimization. Control horizon,  $T$ , is set to 40 convective time units, which is close to 5 flapping period. . . . . 84

# Nomenclature

$A$	peak-to-peak amplitude of unsteady airfoil motion
$C_D$	drag coefficient
$C_L$	lift coefficient
$L_{\text{am}}$	added mass lift
$L_{\text{qs}}$	quasi-steady lift
$L_0$	mean lift at a constant velocity
$\bar{L}$	mean lift
$\hat{L}_k$	magnitude of Fourier coefficient of lift at frequency $k$
$Re$	Reynolds Number, $(cU/\nu)$
$Re_{\text{crit}}$	Critical Reynolds Number
$St_c$	Strouhal number scaled with airfoil chord length $(fc/U)$
$St_A$	Strouhal number scaled with peak-to-peak amplitude $(fA/U)$
$T$	Period of oscillation or control time horizon
$T_{df}$	dynamic formation time
$T^*$	universal formation time
$U$	reference velocity
$c$	airfoil chord length
$k$	reduced frequency, $(\pi fc/U = \pi St_c)$
$k_{\text{vs}}$	reduced frequency corresponding to vortex shedding
$k_{\text{vs, crit}}$	reduced frequency corresponding to vortex shedding at $Re_{\text{crit}}$
$u$	streamwise airfoil velocity

$v$	transverse airfoil velocity
$x_0$	center of rotation
$\Gamma$	circulation
$\Omega$	angular velocity
$\alpha$	angle of attack
$\nu$	fluid kinematic viscosity
$\rho$	fluid density
$\sigma_x$	amplitude of oscillating streamwise velocity with respect to the reference velocity
$\sigma_y$	amplitude of oscillating transverse velocity with respect to the reference velocity
$\phi$	phase of lift leading velocity
$\omega$	vorticity
DVM	Discrete vortex model
IBFM	Immersed boundary fractional step method
LEV	Leading-edge vortex
MAV	Micro-air vehicle
TEV	Trailing-edge vortex

# Chapter 1

## Introduction

As a new class of air vehicles that operate at low Reynolds number, micro-air vehicles (MAVs) face unique challenges different from conventional aircraft. In this low Reynolds number regime, air vehicles are exposed to high drag coefficients ( $C_D$ ), due to laminar flow separation. For their small size and low flight speed, encountering a gust leads to a unsteady flow field, and in some occasions, to stall. Furthermore, transitions from steady to unsteady flow and from laminar to turbulent flow are a frequently encountered phenomenon that conventional aircraft do not experience.

Perhaps for these reasons, birds have adapted to fly with agility at low Reynolds number by utilizing flapping wings (Dickinson & Gotz, 1993; Ellington *et al.*, 1996; Wang, 2005; Pesavento & Wang, 2009).

Regardless of whether a wing is flapping or steadily translating through a gusting flow, better understanding of unsteady aerodynamics at low Reynolds number is required to design efficient and effective MAVs. In this study, we identify distinct features of unsteady flows at low Reynolds number, and implement an optimal control strategy for controlling aerodynamic forces in unsteady flow.

## 1.1 Energy extraction and unsteady aerodynamics at low Reynolds number

Birds have evolved to efficiently transfer energy from the surrounding environment to improve their flight performance and maneuverability. An albatross exploits energy from the velocity gradients of the oceanic boundary layer through dynamic soaring (Denny, 2009), and numerous kinds of birds take advantage of the spatial and temporal gradients of the atmospheric gust to remain aloft without flapping their wings. Extracting energy from the atmospheric gusts during its migration, an Alpine swift is known to continue its journey for 200 consecutive days without being on the ground or in water (Liechti *et al.*, 2013). Thermals and the upward drafts created by the topology also provide additional sources of energy (Weimerskirch *et al.*, 2003).

Recently, there have been several attempts to understand the coupling between the flight mechanics and the underlying fluid dynamics to improve unsteady flight performance of unmanned or micro-air vehicles. Lissaman (2005) considered small vehicles whose flight speed is comparable to atmospheric wind variations. The lift-to-drag ratio was found to be the primary parameter for achieving neutral energy cycles for a vehicle flying through a sinusoidal vertical gust (Lissaman & Patel, 2007), and a state feedback controller that measures current wind speed and its gradient has shown energy gains for both sinusoidal and turbulent gusts (Langelaan, 2009). However, in each of these studies, the models were based on quasi-steady flow approximations where the forces are determined by the instantaneous state of the flow through a static map. Recent studies, discussed more fully below, cast doubt upon this approximation.

While classical unsteady potential flow models effectively describe the dynamical effects on fluid forces through the added mass and trailing-edge Kutta condition (Theodorsen, 1935; Von Karman & Sears, 1938; Greenberg, 1947; Tchieu & Leonard, 2011), these cases are restricted to small changes in velocity at low angle of attack and high Reynolds number, and no comprehensive theory is available for higher angles when the flow separates. MAVs, in particular, are vulnerable to flow separation since laminar boundary layers are less resistant than turbulent boundary layers to the

adverse pressure gradient, and small scaled vehicles would experience separations more frequently than conventional aircraft.

Unsteadiness in conventional air vehicles is considered a deficit since the unsteady motion can lead to separation, instabilities, and flow-structure interactions that are difficult to control. However, with clear understanding of the flow, unsteady effects associated with separations can be utilized to improve maneuverability and performance of MAVs (Pesavento & Wang, 2009). The unsteady motion associated with the flapping flight of insects and birds produces much higher lift than the corresponding steady case (Ellington *et al.*, 1996), and a number of studies have focused on this topic to understand the corresponding flow structures (Dickinson & Gotz, 1993; Ellington *et al.*, 1996; Wang, 2005; Pesavento & Wang, 2009), that could be potentially useful for MAVs. The presence of a leading-edge vortex (LEV) was found to be essential for providing sufficient lift in insect flight (Dickinson & Gotz, 1993; Ellington *et al.*, 1996), and the aerodynamic power required in flapping motions was reduced by capturing its own wake that was generated in the previous stroke cycle (Pesavento & Wang, 2009). Williams *et al.* (2011) have also shown that combining vertical motions of an airfoil with a streamwise oscillating gust produces a net energy gain of the airfoil that is positive when the lift and drag fluctuations are large enough.

The interaction between the wing and the previously shed vortices, sometimes termed ‘wake capture’ when the wing exploits energy from the shed vortices, is also a mechanism to enhance lift. The shed LEV may immediately move far from the wing without causing any notable changes to the force history, or stay close to the airfoil so that the airfoil can take advantage of the low pressure region that is induced by the LEV. For instance, at the end of each forward and backward stroke, fruit flies are known to gain sufficient lift from the lingering wake that was generated from the previous stroke (Dickinson *et al.*, 1999).

For MAVs at high-angles of attack, large-scale vortices associated with separation, such as the LEV or the dynamic-stall vortex, significantly alter the behavior of the aerodynamic forces. Gursul & Ho (1992) and Gursul *et al.* (1994) examined a NACA 0012 airfoil immersed in a temporally varying freestream, and the peak time-averaged lift occurred at a frequency associated with the

shed LEV inducing high pressure gradients normal to the wing during the retreating portion of the cycle. A similar time-averaged behavior of lift has been investigated for transverse airfoil motions (Andro & Jacquin, 2009; Calderon *et al.*, 2013; Cleaver *et al.*, 2011, 2013), and the peak occurred at a frequency where the shed LEV remained close to the airfoil during its convection.

The structure of the LEV over a pitch / surge combined motion has also been investigated by Tsai & Colonius (2015) and Dunne & McKeon (2015) on a two-dimensional vertical-axis wind turbine. Tsai & Colonius (2015) observed that the vortex pair that traveled along with the airfoil substantially decreased lift in the presence of the Coriolis force. For an equivalent planar motion (without the Coriolis effect), the growth and separation of the LEV were described by the interactions of the primary and secondary dynamic separation modes that corresponded to the first and second harmonic frequencies of the motion (Dunne & McKeon, 2015).

## 1.2 Flow models of unsteady aerodynamics

When the flow is attached, classical potential flow models can be utilized to effectively describe the aerodynamic forces of a moving airfoil. Theodorsen (1935) was one of the pioneers to develop an unsteady potential model in 2D to predict the aerodynamic loads on a fluttering airfoil. The main assumptions of his approach are as follows:

- Flow is considered at high Reynolds number flow, and the viscous effects neglected.
- Fluttering amplitude and frequency of the thin airfoil are small enough such that the flow remains attached throughout the entire motion.
- The separation point is only at the trailing edge of the airfoil, and the amount of vorticity in the wake is determined by satisfying the Kutta condition.
- The wake convects with the same speed as the freestream velocity.

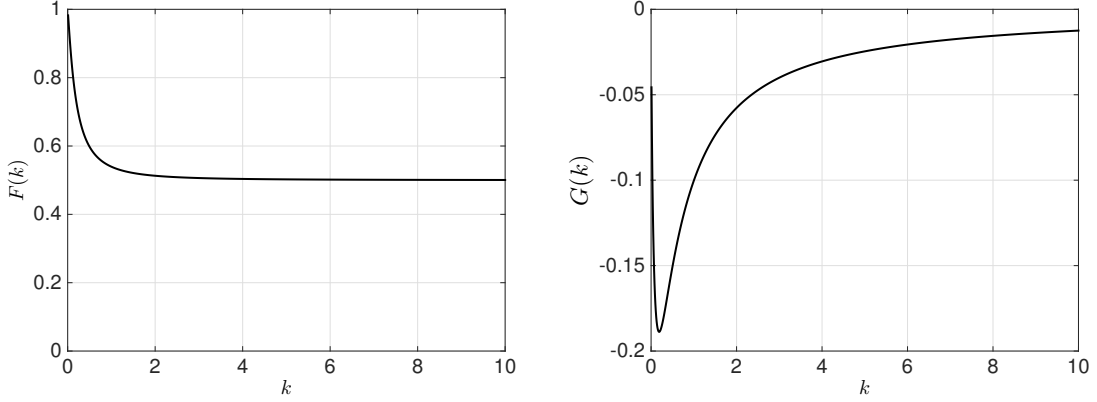


Figure 1.1: Real,  $F(k)$ , and Imaginary,  $G(k)$ , part of the Theodorsen's function,  $C(k)$ .

With these assumption, the lift coefficient,  $C_L$ , of a thin flat plate under harmonic plunging and pitching can be expressed as,

$$C_L = \underbrace{\frac{\pi}{2} [-\dot{y}_b - x_0 \ddot{\alpha} + \dot{\alpha}]}_{C_L^{\text{AM}}} + \underbrace{\mathcal{C}(k) 2\pi \left[ \alpha - \dot{y}_b + \left( \frac{1}{4} - x_0 \right) \dot{\alpha} \right]}_{C_L^{\text{QS}}}, \quad (1.1)$$

where,  $x_0$  is the pitch axis location respect to the mid-chord (pitching about the leading edge corresponds to  $x_0 = -0.5$ , whereas the trailing edge is at  $x_0 = 0.5$ ), and  $y_b$  the transverse movement of the airfoil. The equation is nondimensionalized by normalizing length, velocity, and time by the chord length,  $c$ , freestream velocity,  $U$ , and convective time unit,  $c/U$ , respectively. The first term of equation 1.1 correspond to the non-circulatory part of lift due to the reaction forces of the ambient fluid being accelerated (known as the added mass). The second term accounts for the bound circulation that is induced by the wake vortices. The Theodorsen function,  $C(k) = F(k) + iG(k)$ , which is solely a function of the reduced frequency,  $k = \pi f c / U$ , can be understood as a transfer function that attenuates and lags the phase of lift by an amount that depends on the frequency of the oscillations. Figure 1.1 plots the real and imaginary part of  $C(k)$  as a function of the reduced frequency. In the limit of  $k$  going to zero and infinity,  $C_L$  asymptotically reaches the quasi-steady value,  $C_L^{\text{QS}}$ , and the added mass lift  $C_L^{\text{AM}}$ , respectively.

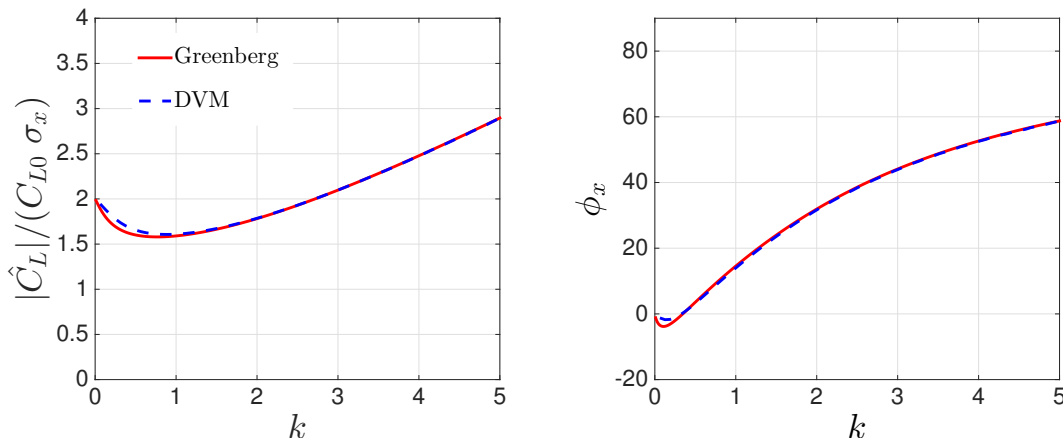


Figure 1.2: Fluctuating amplitude (left) and phase (right) of lift relative to velocity. The results of Greenberg’s model (Greenberg, 1947) and the discrete-vortex model (DVM) from Tchieu & Leonard (2011) are presented.

Greenberg (1947) extended Theodorsen’s model to include the effects of an oscillating freestream on the unsteady lift. With pure freestream oscillation of  $U_\infty = U(1 + \sigma_x \sin \omega_x t)$ , the lift coefficient in Greenberg’s formula can be derived as,

$$\frac{C_L}{C_{L0}} = 1 + \sigma_x \underbrace{\left[ \sqrt{\left(\frac{k}{2} + G\right)^2 + (1 + F)^2} \right]}_{\hat{C}_L(k)} \sin(\omega_x t + \phi_x) + O(\sigma_x^2), \quad (1.2)$$

$$\phi_x = \tan^{-1} \left( \frac{k}{2} + G \right) / (F + 1). \quad (1.3)$$

In equation 1.2, the instantaneous lift coefficient is normalized by the quasi-steady lift coefficient,  $C_{L0} = 2\pi\alpha$ , and high order terms are neglected for  $\sigma_x \ll 1$  (otherwise the flow would not stay attached). According to this model, the time-averaged lift remains independent of  $k$ ; however, the fluctuating amplitude and phase of lift are greatly effected by the reduced frequency. Figure 1.2 plots the normalized amplitude and phase of lift relative to the freestream velocity.  $\hat{C}_L$  is the Fourier component of the fluctuating lift coefficient at the corresponding oscillating frequency,  $k$ . Note that the normalized amplitude,  $|\hat{C}_L|/(C_{L0} \sigma_x)$ , and phase of lift,  $\phi_x$ , are solely a function of  $k$ , and interestingly, the fluctuations are minimized near a frequency of  $k = 0.8$ .

In a similar fashion, the lift coefficient of a plunging airfoil,  $u_y = U\sigma_y \sin(\omega_y t)$ , with constant freestream velocity,  $U_\infty = U$ , can be derived as,

$$\frac{C_L}{C_{L0}} = 1 + \frac{\sigma_y}{\alpha} \left[ \sqrt{\left(\frac{k_x}{2} + G\right)^2 + F^2} \right] \sin(\omega_y t + \phi_y) + O(\sigma_y^2), \quad (1.4)$$

$$\phi_y = \tan^{-1} \left( \left(\frac{k}{2} + G\right)/F \right). \quad (1.5)$$

Using the basic concepts of vortex theory, Von Karman & Sears (1938) derived a formula similar to Theodorsen's model (Theodorsen, 1935), avoiding the complicated mathematical derivations that previous studies possessed. With the same assumptions given as in the Theodorsen's model, they were able to compute the aerodynamic loads on oscillating airfoils as well as on sharp-edge gusts.

Recently, Tchieu & Leonard (2011), assuming discrete vortices in the wake rather than a continuous distribution of vorticity, developed a discrete version of the Von Karman & Sears (1938) model, which in this study is referred to as the discrete vortex model (DVM). The nascent vortex moves at a speed that satisfies the Brown and Michael equation (Brown & Michael, 1954), and sheds whenever it reaches its maximum strength. After the vortex is shed, it convects at the same speed as the freestream velocity. Along with Greenberg's formula, the fluctuating lift coefficient of DVM for the case of streamwise varying velocity is shown in figure 1.2. Despite the convecting speed of the nascent vortex and the discretization of the wake, most of the assumptions that are used to construct the DVM are the same as for the Greenberg's model, and the results are similar. In chapter 3, the lift coefficient obtained from these models will be compared with equivalent computational and experimental results of attached and separated flows.

Although classical unsteady flow models effectively compute the fluid forces on an airfoil (Theodorsen, 1935; Von Karman & Sears, 1938; Greenberg, 1947; Tchieu & Leonard, 2011), the assumptions of the models restrict the flow to be valid only at low angles of attack, high  $Re$ , and small changes of amplitude in motion. For MAVs that operate at high angles of attack and low  $Re$ , viscous effects are no longer negligible, and the flow around the airfoil experiences separation more frequently. At present, no comprehensive theory is available for a fully stalled flow; however, many studies have

attempted to develop a model that covers a wider range of flows than the classical flow models. Enforcing a Kutta condition also at the leading edge, low-order point vortex models have been developed to additionally include the contribution of a LEV on the aerodynamic forces (Wang & Eldredge, 2013; Darakananda *et al.*, 2016). The full description of an inviscid model with multiple Kutta conditions is beyond the scope of this study, and we recommend the reader to refer to Hemati *et al.* (2014) and Darakananda *et al.* (2016) for further details.

The process of a dynamic stall, in general, occurs on a smaller time scale than the development of a full stall (Wang & Eldredge, 2013), and the transient response of the fluid forces to the airfoil motion above the stall angle have also been studied extensively. Related models that are associated with low  $Re$  forward and flapping flights are summarized by Taha *et al.* (2014).

### 1.3 Application to flow control problems

Depending on whether the system requires the input of energy, flow control strategies can be categorized as either *passive* or *active*. Passive control devices modify the geometry of the surface to satisfy a control objective. Among many passive devices, dimples (Bearman & Harvey, 1993; Choi *et al.*, 2006), splitter plates (Anderson & Szewczyk, 1997), riblets (Bechert *et al.*, 2000), and spoilers (Beaudoin & Aider, 2008) are the successful examples that reduce drag or enhance stability. However, there is no systematic way to design devices that meet a given objective, and their shape must be determined through laborious experiments on numerous prototypes.

Active control, on the other hand, requires energy input of the system by the actuator. Whether the output of the system is fed back to the input or not, active control can be classified as either *open-loop* or *closed-loop control* (passive control devices are open-loop controllers). Active open-loop control uses various forcing devices that control the motion of the body (Tokumaru & Dimotakis, 1991) or effectively change the flow around the body (Wu *et al.*, 1998; Greenblatt & Wygnanski, 2000; Post & Corke, 2006). As for passive control methods, a deep understanding of the flow system is required to obtain successful control outputs.

Recently, there has been more interest in closed-loop active control methods, whereby the ac-

tuator (input) is continuously modified by the response of the system. Closed-loop control has an advantage over open-loop control in terms of stability, because it is less sensitive to disturbances and uncertainties. Feedback control using proportional-integral-derivative controllers (Zhang *et al.*, 2004) as well as reduced-order models (Ahuja & Rowley, 2010) has been successfully applied to nonlinear unstable flow problems. Kerstens *et al.* (2011) also applied closed-loop control to suppress lift fluctuations in an unsteady freestream. Feedback control, in general, performs better than open-loop control systems, but, in nonlinear fluid problems, it is sometimes difficult to choose the best feedback signal that enhances the performance.

The feedback control approach used in this study is *adjoint-based optimal control*, where the control inputs that minimize a cost function are determined, under the constraint that the dynamics satisfy the governing differential equations. Adjoint variables are introduced as Lagrange multipliers enforcing the system to satisfy the constraint equations. With an initial guess of the control inputs, this method finds the optimal control that locally minimizes the cost over a given time horizon,  $T$ . One advantage of this method, numerically, is that the computational cost to compute the gradient does not increase with the number of controls. For example, Bewley *et al.* (2001) used every point in the flow domain as an actuator for blowing and suction, re-laminarizing a turbulent channel flow. Unlike other passive and active control approaches, optimal control does not require *a priori* knowledge of the physical mechanism that minimizes the cost, and the optimal solutions themselves often illuminate aspects of the underlying flow physics that would not otherwise have been appreciated.

Currently, due to their high computation cost, adjoint methods are considered as an offline optimization scheme. However, in the future, the development of high performance computers and efficient numerical tools will reduce the time required to compute the solutions, and the adjoint method can perform as a real-time feedback controller. Also, as with the development of lidar (a radar that uses light from a laser) that is capable of measuring upstream flows (Schmitt *et al.*, 2007), the adjoint method can provide estimates of best or worst control strategies during aviation. The further the laser sensor can measure upstream, the further we are capable of predicting the future

with long-term control strategies.

Adjoint based control also arises in shape optimization problems. Pioneered by Jameson (1988), efforts to find the airfoil geometry that minimizes a given cost function were conducted by various researchers (Reuther *et al.*, 1999; Giles *et al.*, 2003). The primary goal in most of these studies was to maximize the lift-to-drag ratio,  $L/D$ , as a measure of the aerodynamic efficiency. Nevertheless, these cases were limited to high  $Re$  and low angle of attack, where the aerodynamic forces were highly effected by the airfoil geometry. For unsteady motions of an airfoil at low  $Re$ , owing to the fact that viscous effects are more severe and flows being more vulnerable to separation than higher  $Re$  flows, aerodynamic forces are less sensitive to the change of airfoil geometry. At  $Re \sim 10^2 - 10^3$ , viscous effects are relatively large, causing high drag and limiting  $L/D$  to be an order of magnitude less than higher  $Re$  ( $> 10^5$ ) cases (Lissaman, 1983). Insects flap their wings at high angles of attack ( $\alpha > 30^\circ$ ), and the flows around their wings are likely to be separated. As a consequence, airfoil shape optimization in low  $Re$  flights may not guarantee the promising results obtained at high  $Re$  cases. Instead, for unsteady flows at low  $Re$ , finding the optimal parameters of the airfoil's motion (kinematic optimization) may be a better strategy to achieve high aerodynamic performance.

## 1.4 Thesis outline

In chapter 2, we discuss the numerical method used to solve unsteady, incompressible flows around airfoils at low Reynolds number, and derive equations for implementing optimal control. In addition, numerical subtleties such as discrete operators, multi-grid techniques, checkpointing algorithms, conjugate gradient method, and line minimization are as well discussed.

In chapter 3, the flow structure and the aerodynamic forces associated with small-amplitude streamwise (surging) and transverse (plunging) oscillating of an airfoils at low Reynolds number are investigated. For simplicity, two-dimensional flows are simulated and we restrict the Reynolds number to  $O(10^2 - 10^3)$  such that, depending on the specific values of angle of attack and Reynolds number, the flow can be subcritical, steady flow, or supercritical, with respect to the usual wake instability associated with a bluff body. The mean and fluctuating behavior of the aerodynamic forces

associated with vortical structure of the wake (vortex lock-in, LEV) are discussed and compared with the experimental results.

High-amplitude surging motions are considered in chapter 4. As the variation in the Reynolds number associated with the motion is large, non-oscillatory uniform flows are first investigated over a wide range of Reynolds number. For the high-amplitude surging motions, the mechanism that leads to the time-averaged peak of lift is of a particular interest, and we investigate this problem by examining vortex strength and flow fields. The time-averaged lift of a motion with square-wave streamwise velocity is also investigated to understand the flow behaviors that are associated with high accelerations.

In chapter 5, using the optimal control framework developed in chapter 2, a simple example that obtains the optimal angle of a flat plate that maximizes lift is presented as a test problem. Optimal control is also applied to flapping motions, where the optimized motion resembles that of a flying insect.

# Chapter 2

## Numerical Methods

The immersed boundary fractional-step method (IBFS), which is used as our fluid solver, is described. Optimal control theory using adjoint equations is also introduced, and used to compute the gradients of the design parameters that minimize a predefined cost function.

### 2.1 Immersed boundary fractional step method

The immersed boundary fractional-step method (IBFS) (Taira & Colonius, 2007; Colonius & Taira, 2008) has been used to solve a two dimensional incompressible flow in the (non-inertial) reference frame of the body (appendix A). The method solves the vorticity-streamfunction formulation of the Navier-Stokes equations and the body is represented by a discrete set of (regularized) surface forces to enforce the no-slip condition. We review the derivations by considering the continuous version of the incompressible Navier-Stokes equations with boundary force,  $f$ , and no-slip condition (Peskin, 1972, 2002):

$$\frac{\partial u}{\partial t} + u \cdot \nabla u = -\nabla p + \frac{1}{Re} \nabla^2 u + \int_s f(\xi(s, t)) \delta(\xi - x) ds, \quad (2.1)$$

$$\nabla \cdot u = 0, \quad (2.2)$$

$$u(\xi(s, t)) = \int_x u(x) \delta(x - \xi) dx = u_b(\xi(s, t)). \quad (2.3)$$

The convolutions with the Dirac delta function,  $\delta$ , are used to exchange information between the Eulerian fluid grid and the Lagrangian body points. Discretizing the above equations, using the

Adams-Bashforth 2nd order scheme on advection term and the Crank-Nicolson method on viscous term (Taira & Colonius, 2007), the terms can be collected to form a matrix such as:

$$\begin{bmatrix} \hat{A} & \hat{G} & -\hat{H} \\ \hat{D} & 0 & 0 \\ \hat{E} & 0 & 0 \end{bmatrix} \begin{pmatrix} u^{n+1} \\ \phi \\ f\Delta t \end{pmatrix} = \begin{pmatrix} \hat{r}^n \\ 0 \\ u_B^{n+1} \end{pmatrix} + \begin{pmatrix} \hat{bc}_1 \\ bc_2 \\ 0 \end{pmatrix}, \quad (2.4)$$

where

$$\hat{A} \equiv I - \frac{\Delta t}{2} \hat{L} \quad \text{and} \quad \hat{r}^n \equiv \left[ I + \frac{\Delta t}{2} \hat{L} \right] u^n - \frac{3\Delta t}{2} \hat{N}(u^n) + \frac{\Delta t}{2} \hat{N}(u^{n-1}). \quad (2.5)$$

Here,  $\hat{G}$  and  $\hat{D}$  are the discrete gradient and divergence operator, respectively. The regularization ( $\hat{H}$ ) and interpolation ( $\hat{E}$ ) operators smear the immersed forces over a few cells and interpolate velocities back to the Lagrangian body points with the specific form of delta function designed by Roma *et al.* (1999).  $\hat{L}$  is the standard 5-point stencil 2nd order Laplacian operator and  $\hat{N}$  the operator relating to the nonlinear term.

Introduce the scaling operators  $R$  and  $\hat{M}$ :

$$R \equiv \begin{bmatrix} \Delta y_j & 0 \\ 0 & \Delta x_i \end{bmatrix} \quad \text{and} \quad \hat{M} \equiv \begin{bmatrix} \frac{1}{2}(\Delta x_i + \Delta x_{i-1}) & 0 \\ 0 & \frac{1}{2}(\Delta y_j + \Delta y_{j-1}) \end{bmatrix}. \quad (2.6)$$

equation (2.4) can be written as:

$$\begin{bmatrix} A & G & -H \\ D & 0 & 0 \\ \hat{E}R^{-1} & 0 & 0 \end{bmatrix} \begin{pmatrix} q^{n+1} \\ \phi \\ f\Delta t \end{pmatrix} = \begin{pmatrix} r^n \\ 0 \\ u_B^{n+1} \end{pmatrix} + \begin{pmatrix} bc_1 \\ bc_2 \\ 0 \end{pmatrix}, \quad (2.7)$$

where

$$\begin{aligned} A &\equiv \hat{M}\hat{A}R^{-1}, \quad G \equiv \hat{M}\hat{G}, \quad H \equiv \hat{M}\hat{H}, \\ D &\equiv \hat{D}R^{-1} = -G^T, \quad r^n \equiv \hat{M}\hat{r}^n, \quad bc_1 \equiv \hat{M}b\hat{c}_1, \quad \text{and } q^{n+1} \equiv Ru^{n+1}. \end{aligned}$$

Also, the mass matrix and the Laplacian are additionally defined as  $M \equiv \hat{M}R^{-1}$  and  $L \equiv \hat{M}\hat{L}R^{-1}$  such that  $A = M - \frac{\Delta t}{2}L$ . We note that  $A$  is symmetric and positive-definite by construction.

For the null space approach in Colonius & Taira (2008), the vorticity-streamfunction formula of the Navier-Stokes equation is solved instead of the primitive variables on a uniform Cartesian grid. The discrete streamfunction,  $s$ , is used that satisfies  $q = Cs$ .  $C$  represents the discrete curl operator, which is constructed with column vectors corresponding to the basis of the null space of  $D$ . Therefore, these operators enjoy the following relation:

$$DC \equiv 0, \tag{2.8}$$

which mimics the continuous identity  $\nabla \cdot \nabla \times \equiv 0$ .

We also introduce another discrete curl operation,  $C^T$ , that is defined as,

$$\gamma = C^T q, \tag{2.9}$$

which is a second-order accurate approximation of the circulation in each dual cell. For the Laplacian,

$$Lq = -\frac{1}{Re\Delta x^2}CC^Tq = -\frac{1}{Re\Delta x^2}C\gamma \equiv -\beta C\gamma, \tag{2.10}$$

provided that  $Dq = 0$ , where  $\beta = \frac{1}{Re\Delta x^2}$ . This identity mimics the continuous identity  $\nabla^2 \mathbf{u} =$

$$\nabla(\nabla \cdot \mathbf{u}) - \nabla \times \nabla \times \mathbf{u} = -\nabla \times \nabla \times \mathbf{u}.$$

Taking the curl of the momentum equation, which we multiply  $C^T$  at both sides of the equation in the first row of the matrix in equation (2.7), the pressure variable is eliminated ( $C^T G = -(DC)^T = 0$ ) and the incompressible constraint is automatically satisfied. The matrix form can be rewritten in the following form:

$$\begin{bmatrix} I + \frac{\beta}{2}\Delta t C^T C & C^T \hat{E}^T \\ \hat{E}C(C^T C)^{-1} & 0 \end{bmatrix} \begin{pmatrix} \gamma^{n+1} \\ f\Delta t \end{pmatrix} = \begin{pmatrix} C^T r^n \\ u_B^{n+1}\Delta x \end{pmatrix} + \begin{pmatrix} \beta\Delta t bc_\gamma \\ 0 \end{pmatrix}. \quad (2.11)$$

Decomposing the left-hand side matrix into a Lower and Upper triangular matrix (Perot, 1993),

$$LU = \begin{bmatrix} I + \frac{\beta}{2}\Delta t C^T C & C^T \hat{E}^T \\ \hat{E}C(C^T C)^{-1} & 0 \end{bmatrix} \quad (2.12)$$

the corresponding matrices are,

$$L = \begin{bmatrix} I + \frac{\beta}{2}\Delta t C^T C & 0 \\ \hat{E}C(C^T C)^{-1} & -\hat{E}C(C^T C)^{-1} \left( I + \frac{\beta}{2}\Delta t C^T C \right)^{-1} C^T \hat{E}^T \end{bmatrix}, \quad (2.13)$$

$$U = \begin{bmatrix} I & \left( I + \frac{\beta}{2}\Delta t C^T C \right)^{-1} C^T \hat{E}^T \\ 0 & I \end{bmatrix}. \quad (2.14)$$

We first solve,

$$L \begin{pmatrix} \gamma^* \\ f \end{pmatrix} = \begin{pmatrix} C^T r^n \\ u_B^{n+1}\Delta x \end{pmatrix} + \begin{pmatrix} \beta\Delta t bc_\gamma \\ 0 \end{pmatrix}, \quad (2.15)$$

which leads to the equation,

$$\begin{aligned}
S \left( I + \frac{\beta \Delta t}{2} \Lambda \right) S \gamma^* &= C^T r^n \\
&= \left( I - \frac{\beta \Delta t}{2} C^T C \right) \gamma^n + \frac{\Delta t}{2 \Delta x^2} \left( 3 C^T N(q^{(k)^n}) - C^T N(q^{(k)^{n-1}}) \right) \\
&\quad + \beta \Delta t b c_\gamma.
\end{aligned} \tag{2.16}$$

The matrix  $C^T C$  is now diagonalized with discrete sin transform  $C^T C = S \Lambda S$  for computational efficiency. To implement the multi-domain technique, equation (2.16) will be modified so that  $\gamma^*$  is now computed on a progressively coarsifying grids with the corrected boundary condition (Colonius & Taira, 2008):

$$\begin{aligned}
S \left( I + \frac{\beta \Delta t}{2} \Lambda \right) S \gamma^{(k)*} &= S \left( I - \frac{\beta \Delta t}{2} \Lambda \right) S \gamma^{(k)^n} + \frac{\Delta t}{2 \Delta x^2} \left( 3 C^T N(q^{(k)^n}) - C^T N(q^{(k)^{n-1}}) \right) \\
&\quad + \frac{\beta \Delta t}{2} b c_\gamma \left( [P^{(k+1) \rightarrow (k)}(\gamma^{(k+1)*})] + [P^{(k+1) \rightarrow (k)}(\gamma^{(k+1)^n})] \right)
\end{aligned} \tag{2.17}$$

$$\begin{aligned}
\implies \gamma^{(k)*} &= S \left( I + \frac{\beta \Delta t}{2} \Lambda \right)^{-1} \left\{ S \left[ \frac{3 \Delta t}{2 \Delta x^2} C^T N(q^{(k)^n}) - \frac{\Delta t}{2 \Delta x^2} C^T N(q^{(k)^{n-1}}) \right] \right. \\
&\quad \left. + \frac{\beta \Delta t}{2} b c_\gamma \left( [P^{(k+1) \rightarrow (k)}(\gamma^{(k+1)*})] + [P^{(k+1) \rightarrow (k)}(\gamma^{(k+1)^n})] \right) \right\} \\
&\quad + \left( I - \frac{\beta \Delta t}{2} \Lambda \right) S \gamma^{(k)^n} \left. \right\}.
\end{aligned} \tag{2.18}$$

Then we solve for the immersed boundary forces,  $f$ , by computing the second row of the equation 2.15.

$$\hat{E} C \left( S \Lambda^{-1} \left( I + \frac{\beta}{2} \Lambda \right)^{-1} S \right) C^T \hat{E}^T f \Delta t = \hat{E} C S \Lambda^{-1} S \gamma^* - u_B^{n+1} \Delta x \tag{2.19}$$

$$\implies f \Delta t = \left( \hat{E} C S \Lambda^{-1} S S \left( I + \frac{\beta}{2} \Lambda \right)^{-1} S C^T \hat{E}^T \right)^{-1} \left( \hat{E} C S \Lambda^{-1} S \gamma^* - u_B^{n+1} \Delta x \right). \tag{2.20}$$

If the body is not moving with respect to the grid, Cholesky decomposition of the term  $\hat{E} C \left( S \Lambda^{-1} \left( I + \frac{\beta}{2} \Lambda \right)^{-1} S \right) C^T \hat{E}^T$  can be performed (since it is symmetric and does not change during the computation), and solve the equation (2.20) efficiently. Finally, the vorticity for the next

time step is computed as,

$$\gamma^{n+1} = \gamma^* - S \left( I + \frac{\beta \Delta t}{2} \Lambda \right)^{-1} S C^T \hat{E}^T f \Delta t. \quad (2.21)$$

Also, we note that since  $C^T N(q) = -C^T \mathcal{N}(q, \gamma)$ , where  $\mathcal{N}(q, \gamma)$  is the discrete operator of  $q \times \gamma$ , we interchange  $N(q)$  with  $\mathcal{N}(q, \gamma)$  in our further derivations of the adjoint equations. This comes from the identity,

$$\nabla \times (u \cdot \nabla u) = \nabla \times \left( \nabla \frac{1}{2} (|u|^2) - u \times \omega \right) = -\nabla \times (q \times \omega). \quad (2.22)$$

## 2.2 Adjoint-based optimal control

### 2.2.1 Optimal control theory

Optimal control via the adjoint method is an active area of research in computational fluid dynamics (Luchini & Bottaro, 2014). The cost of computing the adjoint equation, and thus evaluating the gradient of a cost function, is approximately the same as computing the original forward simulation. Since the computational cost of deriving the gradient is nearly independent of the number of inputs, this approach is much faster than the classical finite-difference methods that compute the Jacobian matrix  $(d\mathcal{J}/d\mathbf{u})$  with respect to each of the control inputs. The adjoint method is based on the calculus of variation (Pontryagin's minimum principle), where the optimal conditions are met by minimizing the control Hamiltonian,  $\mathcal{H}$ . In this section, we review the basic steps of deriving the gradient of a cost function (or functional) using the adjoint approach.

Consider the problem,

$$\begin{aligned} \underset{\phi}{\text{minimize}} \quad & \mathcal{J}, \quad \mathcal{J} = \int_0^T r(x, \phi) dt + v(x(T)) \\ \text{subject to} \quad & \dot{x} = h(x, \phi). \end{aligned} \quad (2.23)$$

We denote  $x$  as the state variable,  $\phi$  as the input or control variable, and  $\mathcal{J}$ , the cost function that represents the objective of the control in a mathematical expression. The goal of this problem is to find the optimal control units that minimizes the cost function subjected to constraints  $\dot{x} = h(x, \phi)$ . The method converges to one of the local minimum solutions that are close to the initial condition. For a flow control problem, the velocity field, vorticity field, or the aerodynamic loads are candidates for the state variable. Various goals can be achieved by controlling the optimal angles of the airfoil, actuator propulsion, and imposing body forces near the body. The constraints that need to be satisfied are the governing equation of the flow variables (the Navier-Stokes equation), and the equation of motions (rigid body dynamics) if the body interacts with the fluid forces.

The function,  $\mathcal{J}$ , that we make an effort to minimize consists of two terms, where  $r(x, \phi)$  is a term that is integrated during the whole control horizon, and  $v( x(T) )$  is the end condition. The first step for obtaining the optimal solution is to derive the gradients of a cost function with respect to the controls. For this purpose, a Lagrange function (or Lagrangian),  $\mathcal{L}$ , is defined with the Lagrange multiplier,  $\lambda$ , to handle the constraints,

$$\begin{aligned} \mathcal{L} &= \int_0^T [r(x, \phi) + \lambda^T (h(x, \phi) - \dot{x})] dt + v( x(T) ) \\ &= \int_0^T [\mathcal{H}(x, \phi, \lambda) - \lambda^T \dot{x}] dt + v( x(T) ). \end{aligned} \quad (2.24)$$

Here we set the control Hamiltonian,  $\mathcal{H}(x, \phi, \lambda) = r(x, \phi) + \lambda^T h(x, \phi)$ , where  $\lambda^T$  is the transpose of  $\lambda$ . Further, expanding the term,  $\lambda^T \dot{x}$ , using integration by parts,

$$\mathcal{L} = \int_0^T [\mathcal{H}(x, \phi, \lambda) + \dot{\lambda}^T x] dt - [\lambda^T x]_0^T + v( x(T) ). \quad (2.25)$$

Taking the total derivative of  $\mathcal{L}$  with respect to  $\phi$ ,

$$\frac{d\mathcal{L}}{d\phi} = \int_0^T \left[ \left( \frac{\partial \mathcal{H}}{\partial x} + \dot{\lambda}^T \right) \frac{\partial x}{\partial \phi} + \frac{\partial \mathcal{H}}{\partial \phi} \right] dt + \left[ \frac{\partial v( x(T) )}{\partial x} - \lambda(T)^T \right] \frac{\partial x(T)}{\partial \phi}. \quad (2.26)$$

In most cases, the term,  $\frac{\partial x}{\partial \phi}$ , is a large dense matrix that is expensive to compute. To circumvent

this expensive calculation, the terms regarding the Lagrange multipliers are instead set to zero,

$$\frac{\partial \mathcal{H}}{\partial x} + \dot{\lambda}^T = 0 \quad (\text{adjoint equation, evolves backwards in time}) \quad (2.27)$$

$$\frac{\partial v(x(T))}{\partial x} - \lambda(T)^T = 0 \quad (\text{initial value of } \lambda), \quad (2.28)$$

which gives an ODE for computing the Lagrange multipliers (equation 2.27). Given the initial values of  $\lambda(T)$  from equation 2.28, the Lagrange multipliers, or the adjoint variables, are computed backwards in time. In this case, the total computation cost of solving the relevant adjoint equation is approximately the same as solving the original forward ODE,  $\dot{x} = h(x, \phi)$ .

Finally, after the adjoint variables are computed, the gradient of the cost function can be computed with the remaining term,

$$\frac{d\mathcal{J}}{d\phi} = \frac{d\mathcal{L}}{d\phi} = \int_0^T \frac{\partial \mathcal{H}}{\partial \phi} dt. \quad (2.29)$$

This gradient, unless it is zero, provides information on how controls should be updated to minimize the cost function. Marching along the direction of the gradient and iterating the process (similar to the process of steepest decent and conjugate gradient methods), the solution eventually converges to the local extremum. The control problem is solved by finding the sets of controls that minimizes  $\mathcal{H}$ , which is known as ‘the control Hamiltonian’. As with the usual Hamiltonian defined in classical mechanics, the control Hamiltonian has a structure of the time evolving system as,

$$\dot{\lambda} = -\frac{d\mathcal{H}}{dx} \quad (2.30)$$

$$\dot{x} = \frac{d\mathcal{H}}{d\lambda}. \quad (2.31)$$

When the optimal condition is achieved the following equation is also satisfied.

$$0 = \frac{d\mathcal{H}}{d\phi}. \quad (2.32)$$

### 2.2.2 Optimization procedure

In this section, the general procedure of obtaining a time-dependent nonlinear optimal solution based on the adjoint method is described. Adjoint solvers were developed based on the earlier works of Ahuja & Rowley (2010) and Joe *et al.* (2010), and fully implemented / coded for the IBFM setup by Flinois & Colonius (2015). As introduced in the previous section (§ 2.2.1), the cost function,  $\mathcal{J}$ , computes a integrated (scalar) value along the control time horizon,  $T$ ,

$$\mathcal{J}(x, \phi) = \int_0^T r(x, \phi) dt + v(x(T)). \quad (2.33)$$

Figure 2.1 depicts the flow diagram of the optimization process used in Flinois & Colonius (2015), and the overall procedure can be outlined as follows (we denote the index  $k$  as the iteration number):

**Step 1:** Guess an initial waveform of the control,  $\phi_0$ , simply by setting it to zero or imposing specific values that are likely to give better solutions. ( $k = 0$ )

**Step 2:** Run the forward simulation with the current control,  $\phi_k$ , to compute the cost,  $\mathcal{J}_k$ .

**Step 3:** Solve the adjoint simulation, to obtain the gradient,  $\left(\frac{\partial \mathcal{H}}{\partial \phi}\right)_k$ .

**Step 4:** Find the distance (scalar value),  $d$ , that minimizes the cost along the direction of the gradient using a line minimization algorithm.

**Step 5:** Update the control waveform by,  $\phi_{k+1} = \phi_k - d \left(\frac{\partial \mathcal{H}}{\partial \phi}\right)_k$ .

**Step 6:** If  $|\phi_{k+1} - \phi_k| > \epsilon$ , increase iteration number  $k = k + 1$  and repeat step 2-6. Else, the control has converged to the optimal condition,  $\phi^*$ .

For simplicity, the procedure described above is the steepest decent method; however, in our computations, the conjugate gradient method, which has proven to be much more efficient, is instead used for the optimization. Among various conjugate gradient algorithms, the Polak-Ribiere formula (Polak, 1970) is known to converge faster than other conjugate algorithms (Shewchuk, 1994), and appears to be the best suited for our non-convex and nonlinear optimization problem. This formula

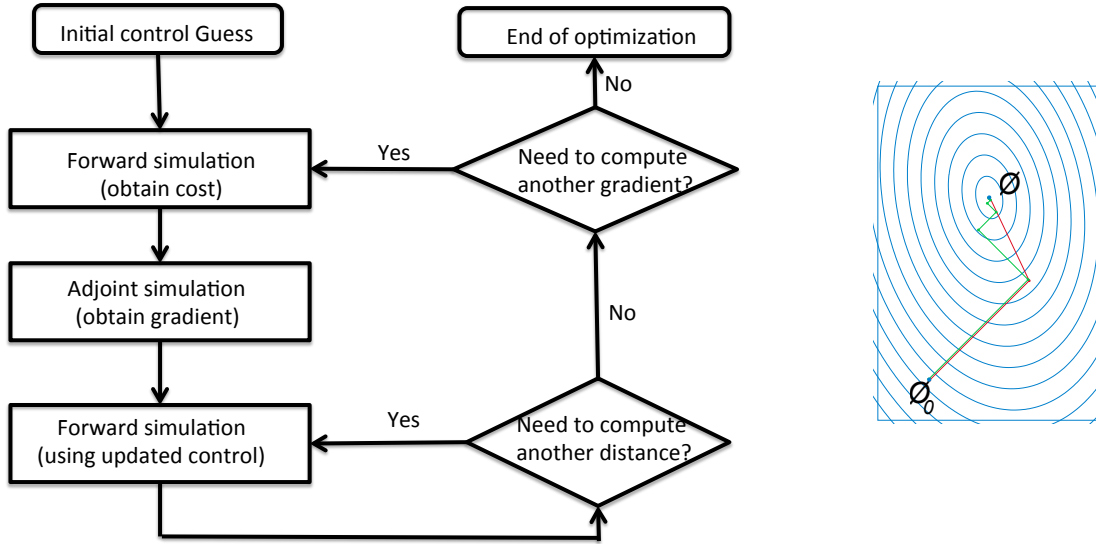


Figure 2.1: Flow diagram of the gradient-based optimization procedure, and a comparison of the convergence of conjugate gradient method (red line) with steepest decent method (green line).

has also been used in other flow control problems, giving promising results (Bewley *et al.*, 2001; Flinois & Colonius, 2015). The conjugate gradient,  $\omega$ , is computed as follows:

$$\omega_{k+1} = \gamma_{k+1} + \beta \omega_k, \quad (2.34)$$

where  $\gamma$ , and  $\beta$  are defined as,

$$\gamma_k = \left( \frac{\partial \mathcal{H}}{\partial \phi} \right)_k, \quad (2.35)$$

$$\beta = \frac{\gamma_{k+1}^T (\gamma_{k+1} - \gamma_k)}{\gamma_k^T \gamma_k}. \quad (2.36)$$

For the detailed line search algorithm used in our computations (step 4 above), we refer the readers to Flinois & Colonius (2015), where a generalized Brent's search algorithm was developed using parallel computing. Each evaluation of a cost respect to a certain control is equal to running one forward simulation, and it is important to develop parallel algorithms that can evaluate the cost

simultaneously.

Another technical challenge related to the adjoint method is the efficient use of memory. While computing the adjoint equation (equation 2.30),

$$\dot{\lambda} = -\frac{d\mathcal{H}}{dx} = -\underbrace{\frac{d}{dx}(r(x, \phi))}_{a(x, \phi)} - \lambda^T \underbrace{\frac{d}{dx}(h(x, \phi))}_{b(x, \phi)}, \quad (2.37)$$

where the forward state variable,  $x$ , is required to compute the coefficients,  $a(x, \phi)$  and  $b(x, \phi)$ , and to evolve the adjoint equation. If there is sufficient memory to store the forward variables at every time step, then the adjoint equation can be solved without any recalculating or interpolations of the forward variables. However, simulations require both large numbers of time steps and grid points such that it is impractical to store the forward variables at every time step. Checkpointing schemes have been developed to mitigate this issue (Griewank, 1992; Griewank & Walther, 2000; Wang *et al.*, 2009). In our computations, the algorithm developed by Wang *et al.* (2009) is implemented to solve the adjoint equations (appendix B). For problems that are too expensive even for the checkpointing schemes, we use linear interpolation to reduce the cost of the reconstruction. Every  $n$  time step is saved such that the error associated with the interpolation is negligible over computing the gradients.

### 2.2.3 Gradient derivations

Obtaining the gradient is an essential part of the overall optimization process. The mathematical expression of the gradient depends on the specific formula of the cost function and the constraint equations, and we introduce how adjoint equations and gradients are derived for the problems considered in these studies.

#### 2.2.3.1 Basic definitions

We first introduce the variables and operators that are used throughout the derivations. The immersed boundary method realizes the surface of the body as discrete numbers of immersed boundary

points, and associated variables are defined as,

$$\text{body : } \mathbf{x}_{b/cm} = \begin{pmatrix} x_{b1/cm} \\ \vdots \\ x_{bn/cm} \\ y_{b1/cm} \\ \vdots \\ y_{bn/cm} \end{pmatrix}, \quad \mathbf{u}_b = \begin{pmatrix} u_{b1} \\ \vdots \\ u_{bn} \\ v_{b1} \\ \vdots \\ v_{bn} \end{pmatrix}, \quad \mathbf{f}_b = \begin{pmatrix} f_{xb1} \\ \vdots \\ f_{xbn} \\ f_{yb1} \\ \vdots \\ f_{ybn} \end{pmatrix}. \quad (2.38)$$

$n$  is the number of total immersed boundary points of the body, and  $\mathbf{x}_{b/cm}$ ,  $\mathbf{u}_b$ , and  $\mathbf{f}_b$  has a dimension of  $(2n \times 1)$ . A vector with a subscript,  $/cm$ , indicates that the variable is expressed in the non-inertial reference frame, which the frame moves with the body, and the origin, attached to the body's center of mass. Although the frame moves with the body's translational velocity it does not rotate. Variables without any subscript are defined respect to the inertial frame of reference with zero frame velocity.  $\mathbf{f}_b$  is the force that is exerted from the fluid to the body, and  $\mathbf{u}_b$  the velocity of IB points.

Actuators can also be realized as IB points, and relevant variables defined as,

$$\text{actuator : } \mathbf{x}_{a/cm} = \begin{pmatrix} x_{a1/cm} \\ \vdots \\ x_{am/cm} \\ y_{a1/cm} \\ \vdots \\ y_{am/cm} \end{pmatrix}, \quad \mathbf{u}_a = \begin{pmatrix} u_{a1} \\ \vdots \\ u_{am} \\ v_{a1} \\ \vdots \\ v_{am} \end{pmatrix}, \quad \mathbf{u}_{a/cm} = \begin{pmatrix} u_{a1/cm} \\ \vdots \\ u_{am/cm} \\ v_{a1/cm} \\ \vdots \\ v_{am/cm} \end{pmatrix}, \quad \mathbf{f}_a = \begin{pmatrix} f_{ax1} \\ \vdots \\ f_{axm} \\ f_{ay1} \\ \vdots \\ f_{aym} \end{pmatrix}, \quad (2.39)$$

where  $m$  is the number of immersed boundary points of an actuator. Similarly,  $\mathbf{f}_a$  is the force exerted from fluid to actuator (thrust), and  $\mathbf{u}_a$ , actuator velocity. The only difference between the IB point that represents a body and an actuator is that for an actuator, an arbitrary velocity other than the body velocity,  $\mathbf{u}_b$ , can be prescribed.  $\mathbf{u}_{a/cm}$  represents the relative actuator velocity with

respect to  $\mathbf{u}_b$ .

Additional variables that we consider are the center of mass velocity and body force (gravity):

$$\mathbf{u}_{cm} = \begin{pmatrix} u_{cm} \\ v_{cm} \end{pmatrix}, \quad \mathbf{g} = \begin{pmatrix} 0 \\ -g \end{pmatrix}, \quad (2.40)$$

where the velocity of each IB points of the body and actuator are now expressed as,

$$\mathbf{u}_b = \mathbf{S}_b \mathbf{u}_{cm} + \Omega \mathbf{R}_b \mathbf{x}_{b/cm}, \quad (2.41)$$

$$\mathbf{u}_a = \mathbf{S}_a \mathbf{u}_{cm} + \mathbf{u}_{a/cm} + \Omega \mathbf{R}_a \mathbf{x}_{a/cm}. \quad (2.42)$$

Operators  $\mathbf{S}_b, \mathbf{S}_a$  of size  $(2n \times 2), (2m \times 2)$ , and  $\mathbf{R}_b, \mathbf{R}_a$   $(2n \times 2n), (2m \times 2m)$  are defined as,

$$\mathbf{S} = \begin{pmatrix} 1 & 0 \\ \vdots & \vdots \\ 1 & 0 \\ 0 & 1 \\ \vdots & \vdots \\ 0 & 1 \end{pmatrix}, \quad \mathbf{R} = \begin{pmatrix} 0 & \dots & 0 & -1 & \dots & 0 \\ \vdots & \ddots & \vdots & \vdots & \ddots & \vdots \\ 0 & \dots & 0 & 0 & \dots & -1 \\ 1 & \dots & 0 & 0 & \dots & 0 \\ \vdots & \ddots & \vdots & \vdots & \ddots & \vdots \\ 0 & \dots & 1 & 0 & \dots & 0 \end{pmatrix}. \quad (2.43)$$

Using the operators defined above, equation of motions regarding the translational and rotation velocity of the rigid body can be expressed as follows:

$$m \dot{\mathbf{u}}_{cm} = \Delta x (\mathbf{S}_b^T \mathbf{f}_b + \mathbf{S}_a^T \mathbf{f}_a) + m \mathbf{g}, \quad (2.44)$$

$$\mathbf{I}_{cm} \dot{\Omega} = \Delta x (\mathbf{x}_{b/cm}^T \mathbf{R}_b^T \mathbf{f}_b + \mathbf{x}_{a/cm}^T \mathbf{R}_a^T \mathbf{f}_a). \quad (2.45)$$

A free-body diagram is illustrated in figure 2.2 to describe these equations.

Now, with the basic definitions of the variables, we introduce the cost function that is used in

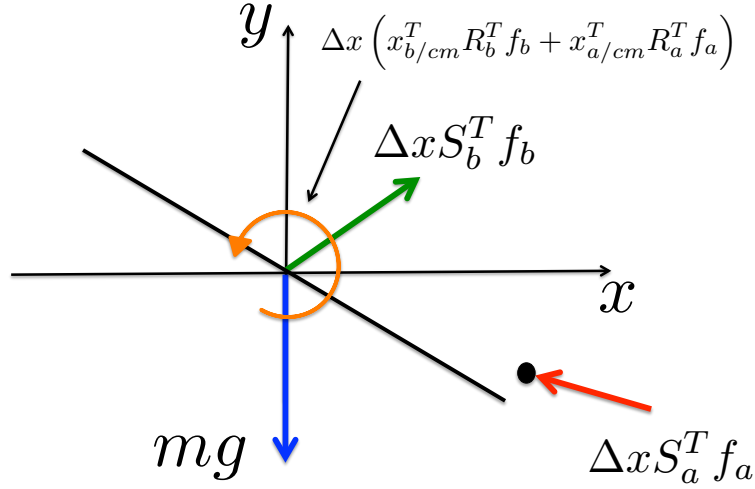


Figure 2.2: Free body diagram of an airfoil with an actuator near the trailing edge. Gravity and resultant fluid force are depicted.

these studies,

$$\begin{aligned}
 \mathcal{J}_{\mathbf{F}} &= \frac{1}{2} \int_0^T (\mathbf{F} - \mathbf{F}_{\text{ref}})^2 dt \\
 &= \frac{1}{2} \int_0^T (\mathbf{F}^2 - 2\mathbf{F}\mathbf{F}_{\text{ref}} + \mathbf{F}_{\text{ref}}^2) dt.
 \end{aligned} \tag{2.46}$$

The cost function,  $\mathcal{J}_{\mathbf{F}}$ , minimizes the difference of the integrated x and y forces to the reference value, where  $F$  is the integrated forces,

$$F = \Delta x (\mathbf{S}_b^T \mathbf{f}_b + \mathbf{S}_a^T \mathbf{f}_a). \tag{2.47}$$

It can be used to minimize drag or maximize lift by setting the components of  $F_{\text{ref}}$  to a very low or high value. Expanding the terms of the quadratic cost function (equation 2.46), the optimization process minimizes the root mean square of  $F$  by the term that corresponds to  $\mathbf{F}^2$ , and at the same time maximizes  $\mathbf{F}$  by the term  $-2\mathbf{F}\mathbf{F}_{\text{ref}}$ .  $\mathbf{F}_{\text{ref}}$  acts as a weighting factor between these two terms.

### 2.2.3.2 Adjoint equations

With the cost function defined, we derive the relevant adjoint equations. Since the IBFM code computes the variables in a rotating frame of reference and variables in the cost function are sometimes defined in a non-rotating reference frame, we introduce a rotational matrix,  $\mathbf{B}(\theta)$ , that transforms a vector expressed in a lab frame to the body-fixed frame. What we refer here as the ‘lab frame’ is the frame of reference that we mentioned in the previous section (§ 2.2.3.1), where the frame of reference moves with the body, but does not, however, rotate (similar to a wind-tunnel experiment).  $\mathbf{B}(\theta)^T$  transforms a vector in body fixed coordinate to the lab frame coordinate.

$$\mathbf{B}(\theta) = \begin{pmatrix} \cos \theta & \sin \theta \\ -\sin \theta & \cos \theta \end{pmatrix}, \quad \text{lab frame} \rightarrow \text{body-fixed frame} \quad (2.48)$$

$$\mathbf{B}(\theta)^T = \begin{pmatrix} \cos \theta & -\sin \theta \\ \sin \theta & \cos \theta \end{pmatrix}, \quad \text{body-fixed frame} \rightarrow \text{lab frame} \quad (2.49)$$

According to this setup, we have the following relations:

$$\tilde{\mathbf{q}}_c(\theta, t) = \Delta x \mathbf{S}_q \mathbf{B}(\theta) \mathbf{u}_{cm}(t) \quad (2.50)$$

$$\tilde{\mathbf{q}}_\Omega(t) = \Delta x \Omega(t) \tilde{\mathbf{x}}_\Omega \quad (2.51)$$

$$\tilde{\mathbf{q}}_{a/cm}(t) = \Delta x \sum_{j=1}^{na} (A_{xj}(t) \tilde{\mathbf{u}}_{axj} + A_{yj}(t) \tilde{\mathbf{u}}_{ayj}) \quad (2.52)$$

$$= \Delta x \sum_{j=1}^{na} \mathbf{B}(\theta) (A_{xjL}(t) \tilde{\mathbf{u}}_{axjL} + A_{yjL}(t) \tilde{\mathbf{u}}_{ayjL}). \quad (2.53)$$

Tilde is assigned for variables in the rotating body-fixed coordinate. The grid velocity flux,  $\mathbf{q} = \Delta x \mathbf{u}$ , is a vector of  $(Nq \times 1)$ , where  $Nq$  is the total number of cell faces of the Eulerian grid.  $\mathbf{q}_c$  and  $\mathbf{q}_\Omega$  are the velocity fluxes that originate from the translational and rotational motion of the body, respectively.  $\mathbf{S}_q$  has a dimension of  $(Nq \times 2)$ , and  $\tilde{\mathbf{x}}_\Omega$  has elements equal to  $-\tilde{y}$  for the x fluxes and  $\tilde{x}$  for the y fluxes, that is  $\tilde{\mathbf{x}}_\Omega = \mathbf{R}\mathbf{B}(\theta)(\mathbf{x} - \mathbf{S}\mathbf{x}_{cm})$ .  $\mathbf{f}$  is a vector including the IB points of the

whole body and actuator points, and  $\tilde{\mathbf{u}}_{axj}, \tilde{\mathbf{u}}_{ayj}$  has the same dimension as  $\mathbf{f}$ , whose elements are either one or zero, effectively selecting the corresponding actuator body points.  $A_{xj}(t)$  and  $A_{yj}(t)$  are the controls that need to be specified initially and evaluated along the procedure. Since it would be easy to interpret or specify the control units in the lab frame, we additionally define  $A_{xjL}(t)$  and  $\bar{\mathbf{u}}_{axjL}$  which are control magnitudes and velocity unit vectors in the lab frame, respectively. The actuator velocity vector,  $\tilde{\mathbf{q}}_{a/cm}$ , has the same dimension as  $\mathbf{f}$ , and is not zero only at the components that corresponds to the actuator IB point (note that the velocity is the relative velocity respect to the body).

The augmented cost function of  $\mathcal{J}_F$  can be represented as:

$$\begin{aligned}
\mathcal{L} = \mathcal{J}_F & - \int_0^T \boldsymbol{\gamma}^\dagger{}^T (C^T C)^{-1} \left( \frac{d\boldsymbol{\gamma}}{dt} + F_{\text{lin}} + F_{\text{nl}} \right) dt \\
& - \int_0^T \mathbf{f}^\dagger{}^T (E(H\boldsymbol{\gamma} - \tilde{\mathbf{q}}_c - \tilde{\mathbf{q}}_\Omega) - \tilde{\mathbf{q}}_{a/cm}) dt \\
& - \int_0^T \mathbf{u}_{cm}^\dagger{}^T \left( \frac{d\mathbf{u}_{cm}}{dt} - \frac{\mathbf{S}^T \mathbf{f}}{m} - \mathbf{g} \right) dt \\
& - \int_0^T \Omega^\dagger \left( \frac{d\Omega}{dt} - \frac{\mathbf{x}_{/cm}^T \mathbf{R}^T \mathbf{f}}{I_{cm}} \right) dt \\
& - \int_0^T \theta^\dagger \left( \frac{d\theta}{dt} - \Omega \right) dt, \tag{2.54}
\end{aligned}$$

where

$$F_{\text{lin}} = -L\boldsymbol{\gamma} + C^T E^T \tilde{\mathbf{f}} \tag{2.55}$$

$$F_{\text{nl}} = -\frac{1}{h^2} C^T \mathcal{N}(H\boldsymbol{\gamma} - \tilde{\mathbf{q}}_c - \tilde{\mathbf{q}}_\Omega, \boldsymbol{\gamma}). \tag{2.56}$$

$\boldsymbol{\gamma}^\dagger, \mathbf{f}^\dagger, \mathbf{u}_{cm}^\dagger{}^T, \Omega^\dagger$ , and  $\theta^\dagger$  are the Lagrange multipliers that represent the adjoint circulation, force, translational body velocity, rotational angular velocity, and angle. The constraint equations are the Navier-stokes equation, no-slip boundary condition, and equation of motions of the rigid body.

Collecting the derivative terms,

$$\mathcal{L} = \int_0^T \mathcal{H} - \boldsymbol{\gamma}^{\dagger T} (C^T C)^{-1} \frac{d\boldsymbol{\gamma}}{dt} - \mathbf{u}_{cm}^{\dagger T} \frac{d\mathbf{u}_{cm}}{dt} - \Omega^{\dagger} \frac{d\Omega}{dt} - \theta^{\dagger} \frac{d\theta}{dt} dt, \quad (2.57)$$

where the control Hamiltonian,  $\mathcal{H}$ , is defined as,

$$\begin{aligned} \mathcal{H} = & + \frac{1}{2} (\mathbf{F} - \mathbf{F}_{\text{ref}})^2 \\ & - \boldsymbol{\gamma}^{\dagger T} (C^T C)^{-1} (F_{\text{lin}} + F_{\text{nl}}) \\ & - \mathbf{f}^{\dagger T} \left( E(H\boldsymbol{\gamma} - \tilde{\mathbf{q}}_c - \tilde{\mathbf{q}}_{\Omega}) - \tilde{\mathbf{q}}_{a/cm} \right) \\ & + \mathbf{u}_{cm}^{\dagger T} \left( \frac{\mathbf{S}_f^T \mathbf{B}_f^T \tilde{\mathbf{f}}}{m} + \mathbf{g} \right) \\ & + \Omega^{\dagger} \left( \frac{\tilde{\mathbf{x}}^T \mathbf{R}_f^T \tilde{\mathbf{f}}}{I_{cm}} \right) \\ & + \theta^{\dagger} \Omega. \end{aligned} \quad (2.58)$$

Previously, we have defined  $\mathbf{F}$  as the integrated x and y forces in equation 2.47, and with the presence of body rotation,

$$\mathbf{F} = \Delta x \mathbf{S}^T \mathbf{B}^T \tilde{\mathbf{f}}. \quad (2.59)$$

It is often desired to set the control variables and cost function in a non-rotating frame, and  $\mathcal{J}_F$  maximizes or minimizes the forces in the x and y direction that stay fixed regardless of the rotations.

From equation 2.30, adjoint equations can be derived as,

$$\begin{aligned} -\frac{d\gamma^\dagger}{dt} &= (C^T C) \left( \frac{\partial \mathcal{H}}{\partial \gamma} \right)^T \\ &= L\gamma^\dagger - C^T E^T f^\dagger + \frac{1}{\Delta x^2} C^T C \mathcal{N}(q^\dagger, q) + \frac{1}{\Delta x^2} C^T \mathcal{N}(\gamma, q^\dagger) \end{aligned} \quad (2.60)$$

$$\begin{aligned} 0 &= \left( \frac{\partial \mathcal{H}}{\partial \tilde{f}} \right)^T \\ &= \Delta x B_f S_f (F - F_{ref}) - E q^\dagger + \frac{1}{m} B_f S_f u_{cm}^\dagger + \frac{1}{I_{cm}} R_f \tilde{x}^T \Omega^\dagger \end{aligned} \quad (2.61)$$

$$\begin{aligned} -\frac{du_{cm}^\dagger}{dt} &= \left( \frac{\partial \mathcal{H}}{\partial \mathbf{u}_{cm}} \right)^T \\ &= \frac{1}{\Delta x^2} \left( \frac{\partial \mathcal{N}}{\partial u_{cm}} \right)^T q^\dagger + \Delta x B^T S_q^T E^T f^\dagger \end{aligned} \quad (2.62)$$

$$\begin{aligned} -\frac{d\Omega^\dagger}{dt} &= \left( \frac{\partial \mathcal{H}}{\partial \Omega} \right)^T \\ &= \frac{1}{\Delta x^2} \left( \frac{\partial \mathcal{N}}{\partial \Omega} \right)^T q^\dagger + \Delta x \tilde{x}_\Omega^T E^T f^\dagger + \theta^\dagger \end{aligned} \quad (2.63)$$

$$\begin{aligned} -\frac{d\theta^\dagger}{dt} &= \left( \frac{\partial \mathcal{H}}{\partial \theta} \right)^T \\ &= \Delta x \tilde{f}^T B'_f S_f (F - F_{ref}) + \frac{1}{\Delta x^2} \left( \frac{\partial \mathcal{N}}{\partial \theta} \right)^T q^\dagger + \Delta x f^{\dagger T} \left( E S_q B' u_{cm} + \frac{\partial \tilde{\mathbf{u}}_a}{\partial \theta} \right) + \frac{1}{m} \tilde{f}^T B_f S_f u_{cm}^\dagger \end{aligned} \quad (2.64)$$

where  $q^\dagger (=C(C^T C)^{-1}\gamma^\dagger)$  is the adjoint velocity flux. If no element is assigned to the operator  $\mathcal{N}$ , then we assume  $\mathcal{N} = \mathcal{N}(H\gamma - \tilde{q}_c - \tilde{q}_\Omega, \gamma)$ . The derivatives in the adjoint equations are,

$$\left( \frac{\partial \mathcal{N}}{\partial \mathbf{u}_{cm}} \right)^T q^\dagger = -\Delta x B^T S_q^T \mathcal{N}(\gamma, q^\dagger) \quad (2.65)$$

$$\left( \frac{\partial \mathcal{N}}{\partial \Omega} \right)^T q^\dagger = -\Delta x \tilde{x}_\Omega^T \mathcal{N}(\gamma, q^\dagger) \quad (2.66)$$

$$\left( \frac{\partial \mathcal{N}}{\partial \theta} \right)^T q^\dagger = -\Delta x \mathbf{u}_{cm}^T B'^T S_q^T \mathcal{N}(\gamma, q^\dagger) \quad (2.67)$$

$$\frac{\partial \tilde{\mathbf{u}}_a}{\partial \theta} = \sum_{j=1}^{na} \mathbf{B}'(\theta) (A_{xjL}(t) \tilde{\mathbf{u}}_{axjL} + A_{yjL}(t) \tilde{\mathbf{u}}_{ayjL}). \quad (2.68)$$

The above adjoint equations are solved backwards in time, and since there is no terminal condition

in the cost function, all values of the adjoint variables at  $t = T$  are zero.

$$\lambda(T) = \phi(T) = \epsilon(T) = \delta(T) = \psi(T) = 0. \quad (2.69)$$

Equation 2.60 is the governing equation of the adjoint flow variables, and equation 2.61 the adjoint no-slip boundary condition. Considering these equations as a set of equations similar to the forward system (equation 2.11):

$$\begin{bmatrix} I + \frac{\beta}{2}\Delta t C^T C & C^T \hat{E}^T \\ \hat{E}C(C^T C)^{-1} & 0 \end{bmatrix} \begin{pmatrix} \gamma^{\dagger n-1} \\ f^\dagger \end{pmatrix} = \begin{pmatrix} C^T r^n \\ \mu^{n-1} \end{pmatrix} + \begin{pmatrix} bc_\lambda \\ 0 \end{pmatrix}, \quad (2.70)$$

where  $\mu$  is the adjoint slip velocity defined as,

$$\mu^{n-1} = \Delta x B_f S_f (F - F_{ref}) + \frac{1}{m} B_f S_f u_{cm}^{\dagger n-1} + \frac{1}{I_{cm}} R_f \hat{x}^T \Omega^{\dagger n-1}. \quad (2.71)$$

The adjoint slip velocity depends on specific formula of the cost function and the constraint equations.

As with the forward simulation case, we perform a LU decomposition on this matrix, resulting the following set of equations:

$$\gamma^{\dagger*} = \left[ S \left( I + \frac{\beta \Delta t}{2} \Lambda \right) \right]^{-1} S C^T r^n + bc_\lambda, \quad (2.72)$$

$$f^\dagger \Delta t = \left( \hat{E} C S \Lambda^{-1} S S \left( I + \frac{\beta}{2} \Lambda \right)^{-1} S C^T \hat{E}^T \right)^{-1} \left( \hat{E} C S \Lambda^{-1} S \gamma^{\dagger*} - \mu^{n-1} \right), \quad (2.73)$$

$$\gamma^{\dagger n-1} = \gamma^{\dagger*} - S \left( I + \frac{\beta \Delta t}{2} \Lambda \right)^{-1} S C^T \hat{E}^T f^\dagger \Delta t. \quad (2.74)$$

During the evaluation of equation 2.73, equation 2.62 to 2.64 are solved to compute the adjoint slip velocity. Briefly describing this method,

**Step 1:** predict  $u_{cm}^\dagger$ ,  $\Omega^\dagger$ , and  $\theta^\dagger$  using explicit Euler:

$$u_{cm}^{\dagger n-1/2} = u_{cm}^{\dagger n} + \Delta t f_{u_{cm}^\dagger}(f^{\dagger n}) \quad (2.75)$$

$$\Omega^{\dagger n-1/2} = \Omega^{\dagger n} + \Delta t f_{\Omega^\dagger}(f^{\dagger n}, \theta^{\dagger n}) \quad (2.76)$$

$$\theta^{\dagger n-1/2} = \theta^{\dagger n} + \Delta t f_{\theta^\dagger}(f^{\dagger n}, u_{cm}^{\dagger n}) \quad (2.77)$$

$f_{u_{cm}^\dagger}(\phi^n)$  is the right-hand side of (equation 2.62), and the same for  $f_{\Omega^\dagger}$  and  $f_{\theta^\dagger}$ .

**Step 2:** Solve for  $f^{\dagger n-1/2}$  from

$$f^{\dagger n-1/2} \Delta t = \left( \hat{E}CS\Lambda^{-1}SS \left( I + \frac{\beta}{2}\Lambda \right)^{-1} SC^T \hat{E}^T \right)^{-1} \left( \hat{E}CS\Lambda^{-1}S\gamma^{\dagger*} - \mu^{n-1/2} \right) \quad (2.78)$$

**Step 3:** Correct  $u_{cm}^\dagger$ ,  $\Omega^\dagger$ , and  $\theta^\dagger$

$$u_{cm}^{\dagger*} = \frac{1}{2} \left( u_{cm}^{\dagger n-1/2} + u_{cm}^{\dagger n} \right) \quad (2.79)$$

$$\Omega^{\dagger*} = \frac{1}{2} \left( \Omega^{\dagger n-1/2} + \Omega^{\dagger n} \right) \quad (2.80)$$

$$f^{\dagger*} = \frac{1}{2} \left( f^{\dagger n-1/2} + f^{\dagger n} \right) \quad (2.81)$$

$$\theta^{\dagger*} = \frac{1}{2} \left( \theta^{\dagger n-1/2} + \theta^{\dagger n} \right) \quad (2.82)$$

and update

$$u_{cm}^{\dagger n-1} = u_{cm}^{\dagger*} + \Delta t f_{u_{cm}^\dagger}(f^{\dagger*}, \kappa^*) \quad (2.83)$$

$$\Omega^{\dagger n-1} = \Omega^{\dagger*} + \Delta t f_{\Omega^\dagger}(f^{\dagger*}, \psi^*) \quad (2.84)$$

$$\theta^{\dagger n-1} = \theta^{\dagger*} + \Delta t f_{\theta^\dagger}(f^{\dagger*}, u_{cm}^{\dagger*}) \quad (2.85)$$

**Step 4:** Get the next time step adjoint force  $f^{\dagger n-1}$ :

$$f^{\dagger n-1} \Delta t = \left( \hat{E}CS\Lambda^{-1}SS \left( I + \frac{\beta}{2}\Lambda \right)^{-1} SC^T \hat{E}^T \right)^{-1} \left( \hat{E}CS\Lambda^{-1}S\gamma^{\dagger*} - \mu^{n-1} \right) \quad (2.86)$$

After the corrected adjoint force is computed, the adjoint vorticity at time step  $n-1$  can be solved by equation 2.74. Knowing both the forward and adjoint variables, the gradient can be computed along with the adjoint solver. We note that the checkpointing algorithm developed by Wang *et al.* (2009) is implemented to minimize the recalculations of the forward variables (appendix B).

### 2.2.3.3 Gradients

Finally, the gradients of the cost function respect to the controls (actuator velocity, angular velocity) can be derived as (equation 2.29),

$$\left(\frac{\partial \mathcal{H}}{\partial A_{xjL}}\right) = -\Delta x \left(Q_{\text{pow}} \tilde{f}^T - f^{\dagger T}\right) \mathbf{B}_f \bar{\mathbf{u}}_{axjL} \quad (2.87)$$

$$\left(\frac{\partial \mathcal{H}}{\partial A_{yjL}}\right) = -\Delta x \left(Q_{\text{pow}} \tilde{f}^T - f^{\dagger T}\right) \mathbf{B}_f \bar{\mathbf{u}}_{ayjL} \quad (2.88)$$

$$\left(\frac{\partial \mathcal{H}}{\partial \Omega}\right) = -\Delta x \left(Q_{\text{pow}} \tilde{f}^T - f^{\dagger T}\right) E \tilde{x}_{\Omega} - \frac{1}{\Delta x^2} \left(\frac{\partial \mathcal{N}}{\partial \Omega}\right)^T + \theta^{\dagger}. \quad (2.89)$$

Note that the gradient has a term arising from the original cost function, and a term related to the adjoint solution.

## Chapter 3

# Low-Amplitude Surging and Plunging Airfoils

In this chapter, we investigate the forces and unsteady flow structures associated with low-amplitude harmonic oscillations of an airfoil in the streamwise (surging) and transverse (plunging) directions. Specific frequency regimes where the wake instability synchronizes to the unsteady motion are investigated as well as the regimes where the fluctuating forces are amplified and attenuated. A detailed study of the flow structure associated with LEV growth and detachment is used to relate this behavior.

### 3.1 Problem description

We model the airfoil as a thin flat plate; the immersed boundary method regularizes (smears) the thickness of the plate to a few grid cells. The computational domain extends to 32 and 48 chord lengths in the transverse and streamwise directions, respectively, and truncates the vorticity field with zero Dirichlet boundary conditions. Multiple grid resolutions are used for computational efficiency, and convergence tests were performed on a  $480 \times 320$  and  $960 \times 640$  grid resolution over the finest grid level. The  $240 \times 160$  grid resolution was sufficient for most of the cases reported, however, for the highest  $Re$  we used the finer grid. The time steps were chosen based on the CFL condition, which we set it to be less than 0.5. We have also investigated the response of a NACA 0006 airfoil; the results were substantially the same for both airfoils and in what follows, we only

present results for the thin flat plate. The angle of attack of the airfoil ( $\alpha$ ) is varied between  $\alpha = 5^\circ$  and  $20^\circ$ . For the thin airfoil at low Reynolds number, the flow separates at the leading-edge at  $\alpha = 15^\circ$  and  $20^\circ$ , but remains attached for the  $5^\circ$  case.

The  $x$  and  $y$  components of the motion of the body are specified as

$$u = U(1 + \sigma_x \sin(\omega t)) = U(1 + \sigma_x \sin(2ktU/c)) \quad (3.1)$$

$$v = U\sigma_y \sin(\omega t + \theta) = U\sigma_y \sin(2ktU/c + \theta), \quad (3.2)$$

where  $k$  is the reduced frequency ( $= \pi fc/U$ ) and  $U$  the mean velocity of the vehicle in the streamwise direction.  $U\sigma_x$  and  $U\sigma_y$  are the fluctuating velocities in the  $x$  (streamwise, surging) and  $y$  (transverse, plunging) directions, respectively, and  $\theta$  is the phase between plunge and surge. In this chapter, we consider surging and plunging separately, so  $\theta$  is not used. The normalized velocity amplitude,  $\sigma$ , is set to a constant as we increase the frequency, and, as a result, the amplitude of the motion decreases with increasing reduced frequency. We also note that when (typically plunging) motions are characterized by a peak-to-peak displacement,  $A$  ( $= 2\sigma c/\omega$ ), then the quantity  $St_A$  is related to  $\sigma$  by  $St_A = \frac{\sigma}{\pi}$ . Plunging involves oscillations in both the speed and the effective angle of attack,  $\alpha_e$ , given by

$$\alpha_e = \alpha + \tan^{-1} \left( \frac{\sigma_y U \sin \omega t}{U} \right) = \alpha + \tan^{-1}(\sigma_y \sin \omega t), \quad (3.3)$$

and the variation of  $\alpha_e$  is bounded by  $\sigma_y$ .

These unsteady airfoil motions can, in the present case, be reinterpreted as a temporally varying freestream velocity, representing a uniform stream with an oscillatory gust in the streamwise and transverse directions. This is because the apparent buoyancy force,  $\rho \dot{\mathbf{u}} V_b$ , where  $V_b$  is the volume of the body, is negligible for a thin airfoil in air for the range of reduced frequencies considered here.

To measure the resulting time-periodic forces on the plate, it was sufficient to compute about 10 periods of oscillation to eliminate the transient part of the time history, and the data reported below were collected after this time. When the oscillation frequency was close to the wake instability, we

needed more than 80 cycles to capture the low (beating) spectrum of the flow, however, in most cases, 20 periods were long enough to capture the response spectrum.

The reduced frequency is varied from zero to almost twice the value of the natural vortex shedding frequency (which was computed for steady motion of the plate independently) and amplitude,  $\sigma_x$  and  $\sigma_y$ , up to 80% (high-amplitude motions are described in more detailed in chapter 4) of the mean velocity,  $U$ , respectively.

Before examining the surging and plunging cases, it is informative to document the natural flow over the range of  $Re$  and  $\alpha$  considered. The Reynolds number,  $Re = Uc/\nu$ , is defined based on the mean streamwise velocity,  $U$ , the chord length,  $c$ , and the kinematic viscosity,  $\nu$ . At each  $\alpha$ , there is a critical Reynolds number,  $Re_{\text{crit}}$ , below which a steady, separated flow is obtained. At  $Re_{\text{crit}}$ , there is a supercritical Hopf bifurcation (Sreenivasan *et al.*, 1987) resulting in an oscillatory wake and at sufficiently high  $Re$ , vortex shedding. Hopf bifurcation at  $Re_{\text{crit}}$  is shown in figure 3.1 for  $\alpha = 15^\circ$ .

Both  $Re_{\text{crit}}$  and the initial instability frequency  $k_{\text{VS}}$  are plotted versus  $\alpha$  in figure 3.2. Most of the variation in  $Re_{\text{crit}}$  and  $k_{\text{VS}}$  can be understood as resulting from the varying projected area of the plate in the direction of flow, i.e. bluff body scaling (Fage & Johansen, 1927).  $Re_{\text{p,crit}}$  and, particularly,  $k_{\text{p,crit}}$ , both defined using the projected chord length,  $c \sin \alpha$ , are more nearly constant with  $\alpha$ . The nearly constant value of  $k_{\text{p,crit}}$  corresponds to a Strouhal number of 0.13, and according to Huang & Lin (1995), this value increases up to 0.2 at higher  $Re$ . The supercritical flows considered in this chapter fall into the category of laminar vortex shedding in Huang & Lin (1995), where boundary layers are separated from the upper surface without any shear-layer instability or turbulence. For reference below, the oscillatory flows we consider in the following sections have  $\alpha = 5^\circ, 15^\circ$  and  $20^\circ$ , where the critical Reynolds numbers are  $Re_{\text{crit}} = 1519, 254$  and  $164$ , respectively.

We understand that even for an infinite aspect-ratio wing, the two-dimensional flow assumption is not adequate to describe the transition of the wake that would occur at some of the super-critical values of  $Re$  we consider. However, a complete description of the bifurcations to three-dimensional flow in this geometry, especially in unsteady flow, is lacking and, despite the simplifications, the

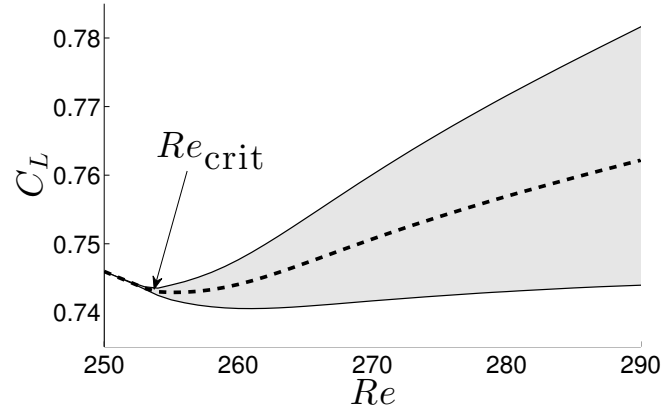


Figure 3.1: Hopf bifurcation at  $Re_{\text{crit}} = 254$  (simulation). Fluctuating ranges (gray area) and mean values (dashed line) are shown for  $250 < Re < 290$ . Flat plate,  $\alpha = 15^\circ$ .

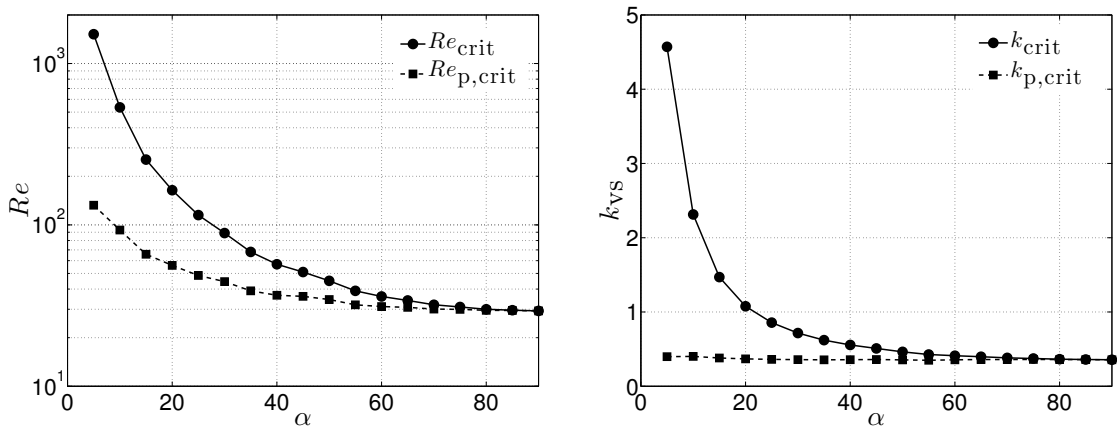


Figure 3.2: Critical Reynolds numbers ( $Re_{\text{crit}}$ ) and corresponding vortex shedding reduced frequencies ( $k_{\text{vs,crit}}$ ) at different angles of attack. The subscript  $p$  refers to quantities made dimensionless by the projected chord length,  $c \sin \alpha$ .

qualitative agreement between our results and experiments at much higher  $Re$  (section §3.2.2) leads us to believe that the mechanisms are the same.

## 3.2 Surging

Since most of the past work related to unsteady airfoil motions was focused on plunging (Jones *et al.*, 1996; Lewin & Haj-Hariri, 2003; Young & Lai, 2007; Andro & Jacquin, 2009; Cleaver *et al.*, 2011, 2012, 2013; Calderon *et al.*, 2013), surging is first considered in greater detail.

### 3.2.1 Vortex lock-in and time-averaged lift

Here we consider  $\alpha = 15^\circ$  and  $Re = 300 > Re_{\text{crit}}$ , and investigate lock-in regions with  $\sigma_x$  as the bifurcation parameter. Previous researchers characterized the flow as locked-in when the natural wake instability synchronized its frequency to the forcing frequency (Karniadakis & Triantafyllou, 1989; Young & Lai, 2007). We thus define vortex lock-in when the dominant peaks in the lift spectrum only occur at harmonic frequencies of the motion. Representative phase-space plots ( $C_L(t)$  versus  $U(t)$ ), and frequency spectra of  $C_L$  are shown in figure 3.3. Trajectories in the lift-velocity phase space collapse to a single curve for the lock-in cases (left and right) with dominant peaks occurring at the harmonic frequencies of the motion. However, for the quasi-periodic case (center), there is a phase shift with multiple peaks appearing in the lift spectrum that correspond to the sum and difference of the natural wake instability,  $k_{\text{VS}}$ , and the oscillating motion.

Lock-in regions are shown over a continuous range of reduced frequencies in figure 3.4 for relatively low velocity amplitudes,  $0 < \sigma_x < 0.1$ . We observe two independent branches at  $k/k_{\text{VS}} = 1/2$  and  $k/k_{\text{VS}} = 1$ . The lock-in regions grow with increasing surging amplitude, representing a V-shaped region that is known as the Arnold tongue or the resonance horn for parametric oscillators (Boyland, 1986). A clear correlation between the lift increment region of  $\bar{L}/L_0 > 1$  ( $\bar{L}$  is the averaged lift for the surging airfoil, and  $L_0$  the mean lift for the base flow) and lock-in state of the flow reveals that the time-averaged lift increases when the flow is locked-in. This type of resonance has also been previously investigated by Munday & Taira (2013) for a 2D circular cylinder with actuators on the

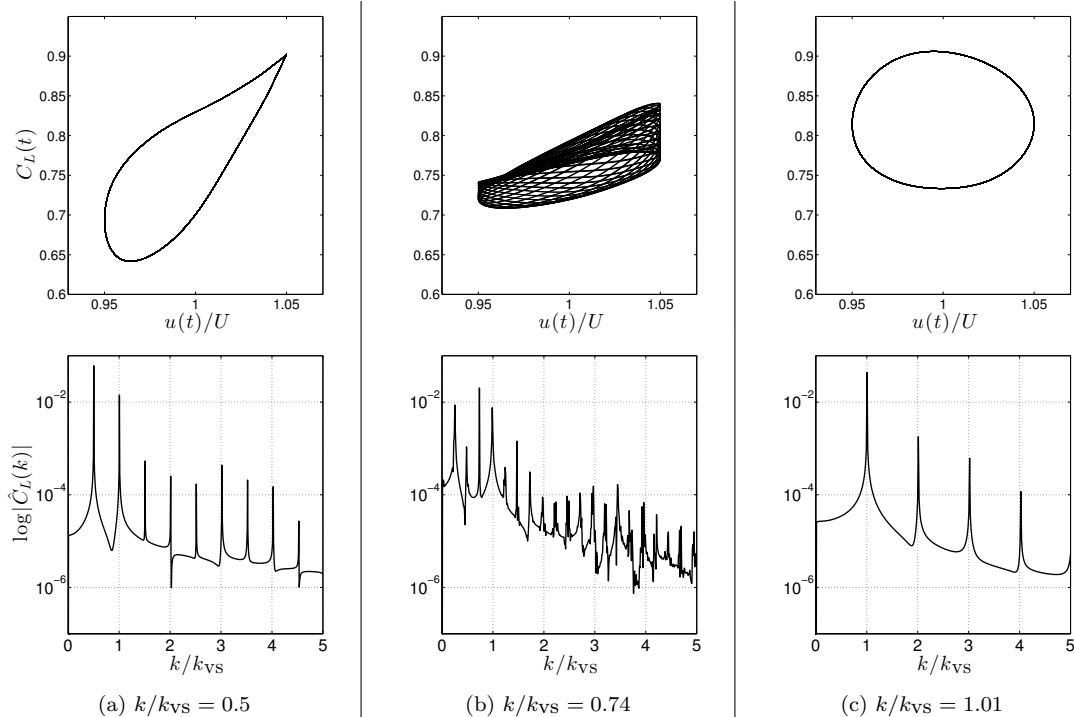


Figure 3.3: Representative cases with (left and right) and without (center) lock-in. Surging amplitude is  $\sigma_x = 0.05$  and the phase plot of lift coefficient and x-velocity are shown with the frequency spectra for 50 periods of surging frequency,  $k$ . Flat plate,  $Re = 300$ ,  $\alpha = 15^\circ$  and  $k_{VS} = 1.62$ .

rear part of the body, and only one tongue near  $k/k_{VS} = 1$  appeared compared to two for a flat plate. Drag forces are also excited at these lock-in regions; it is primarily the force normal to the flat plate that is enhanced during lock-in.

With increasing  $\sigma_x$ , the time-averaged peak occurs at a frequency near  $k = 1$ , which is far from the natural shedding frequency,  $k_{VS} = 1.62$  (figure 3.5). For high-amplitude motions ( $\sigma_x > 0.2$ ), specific flow structures and behavior of mean lift will be described in chapter 4.

### 3.2.2 The leading-edge vortex and fluctuating lift

The fluctuating lift is now examined via a Fourier transform of the lift, from which the amplitude and phase are evaluated at each surging frequency. Following the unsteady potential model (Greenberg, 1947) we consider the quantity  $|\hat{L}_k|/(L_0\sigma_x)$ , where  $\hat{L}_k$  is the Fourier component of the fluctuating lift at the corresponding surging frequency,  $k$ , and where we normalize, in our case, by the base flow mean lift,  $L_0$ . Figure 3.6 shows that at  $Re = 300$  and  $\alpha = 15^\circ$ , the normalized lift fluctuation is

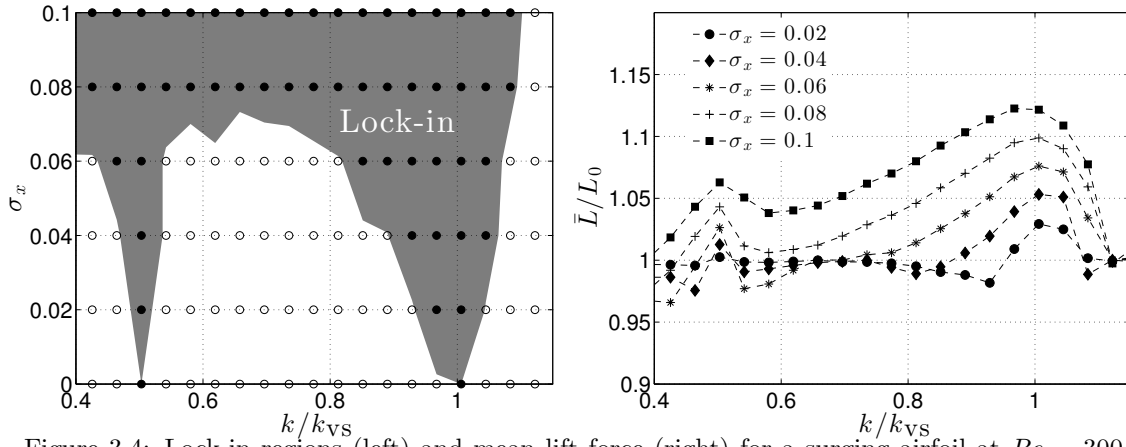


Figure 3.4: Lock-in regions (left) and mean lift force (right) for a surging airfoil at  $Re = 300$  and  $\alpha = 15^\circ$ . Lock-in regions are defined where  $\gamma < 10^{-2}$ .  $L_0$  is the mean lift for  $\sigma_x = 0$ .

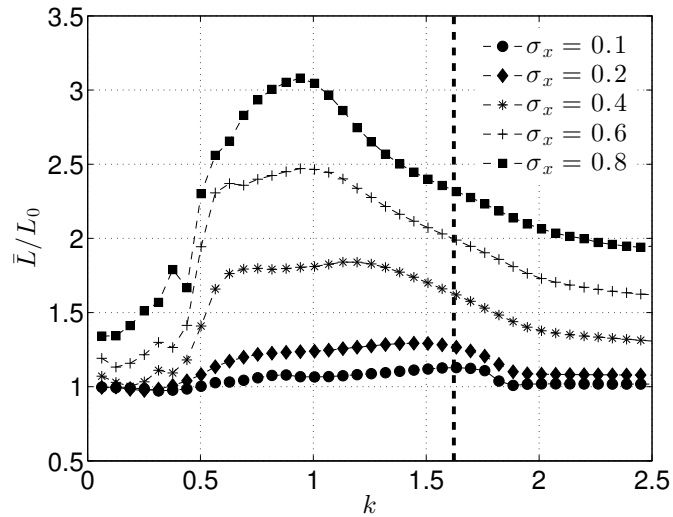


Figure 3.5: Time-averaged lift for  $0.1 < \sigma_x < 0.8$ . Vertical line indicates the vortex shedding frequency of steady flow ( $\sigma_x = 0$ ). Flat plate,  $\alpha = 15^\circ$ ,  $Re = 300$ .

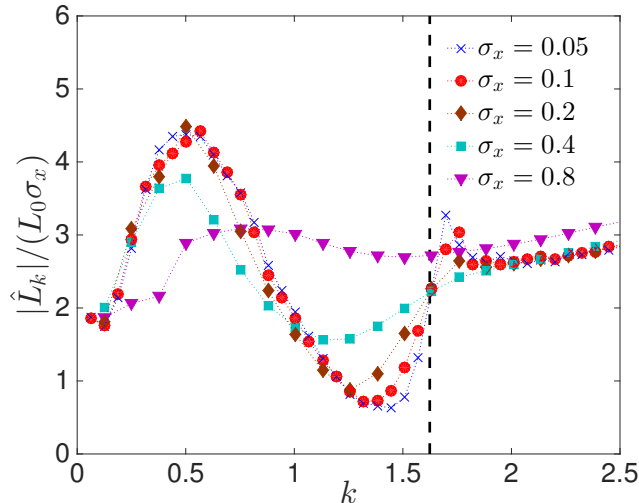


Figure 3.6: Fluctuating amplitude of lift. Aerodynamic response is nearly independent of  $\sigma_x$  for  $\sigma_x \leq 0.2$ . Vertical line indicates the vortex shedding frequency of steady flow ( $\sigma_x = 0$ ). Flat plate,  $\alpha = 15^\circ$ ,  $Re = 300$ .

nearly independent of velocity fluctuation amplitude for  $\sigma_x \leq 0.2$ ; the same is true for other values of  $Re$  and  $\alpha$  considered here. Figure 3.7 shows the lift fluctuations and their phase as a function of  $k$  for a range of angles of attack, and includes data from companion experiments at a higher  $Re$  of 57,000 conducted in an unsteady wind tunnel at the Illinois Institute of Technology (Granlund *et al.*, 2014). Also plotted are the theoretical (potential flow) results; note that when scaled this way, the theoretical fluctuating lift normalized by  $L_0$  and  $\sigma_x$  is independent of angle-of-attack (equation 1.2).

Numerical and experimental results follow the general trend of the potential flow result when the flow is attached (at  $\alpha = 5^\circ$ ). At higher  $\alpha$ , where the flow is separated, unsteady flow structures drastically alter this behavior (at  $\alpha = 15^\circ$  and  $20^\circ$ ). As  $\alpha$  is increased, two frequency bands emerge where the fluctuations are amplified and attenuated, respectively. For example, at  $\alpha = 15^\circ$ ,  $Re = 500$ , the fluctuating magnitude of lift at  $k = 0.6$  is more than twice the amplitude at  $k = 0$  (the quasi-steady limit value) and at  $k = 1.2$ , it is less than half. In the simulations, these trends are more pronounced with increasing  $Re$ . Near  $k_{VS}$ , a second maximum in fluctuations occurs which is related to the aforementioned lock-in phenomena. However, it is important to note that, by contrast, the  $k$  values where the first amplification and attenuation of fluctuations occur do not shift with the shifting vortex shedding frequency associated with the differing Reynolds numbers (see the vertical

lines on the plot). This suggests that these regimes are not associated with the wake instability, a conclusion that is further supported by the fact that for  $\alpha = 15^\circ$  and  $20^\circ$ , the amplification and attenuation behavior occurs at both sub- and super-critical values of  $Re$ .

The amplification and attenuation regimes are related to the formation and convection of an LEV, and now we examine the corresponding flow structures. Flow visualizations at the amplification ( $k = 0.7$ ) and attenuation ( $k = 1.2$ ) frequencies examined at  $Re = 500$  (simulations) and  $Re = 57,000$  (experiments) are shown in figure 3.8 for  $\alpha = 20^\circ$ . Streaklines from the simulations are compared to the smoke-wire images from the experiments at two phases of oscillation velocity, namely the maximum,  $u_{\max} = U(1 + \sigma_x)$  and the minimum,  $u_{\min} = U(1 - \sigma_x)$ . For the frequencies where the fluctuations are amplified ( $k = 0.7$ ), the lift enhancement attributed to the LEV occurs at the advancing portion of the cycle. A strong LEV is formed above the airfoil at  $u_{\max}$ , and the low pressure regions induced by the LEV enhances the lift higher than the quasi-steady case. At  $u_{\min}$ , on the other hand, the shear layer is deflected from the airfoil and the lift is reduced with the larger separation region. The LEV forms a dipole with the TEV, and because of the positioning and orientation of these two vortices their induced velocity is directed upstream, broadening the separated region (Calderon *et al.*, 2013). In this case, the incremental lift from the LEV is occurring in phase with the maximum quasi-static lift, and lift reduction due to flow separation is occurring at the minimum velocity. The lift fluctuations are thus amplified.

At  $k = 1.2$ , the situation is different. The LEV is still inducing low pressure regions above the airfoil; however, over the advancing portion of the cycle, the phase of its growth is delayed and at  $u_{\max}$ , the LEV has grown only to half the length of the chord. The LEV achieves its full extent at a later phase of the motion and is shed during the retreating portion of the oscillation cycle. However, as this shed vortex advects, it remains close to the airfoil, compared to the amplification case, and also produces a positive lift during the retreating portion of the cycle. Since the incremental lift by LEV occurs at a later phase of the motion, and the shed LEV offsets the negative quasi-steady component of lift, the fluctuations are suppressed. Despite the vast difference in  $Re$ , the behavior is qualitatively similar in experiment and simulation.

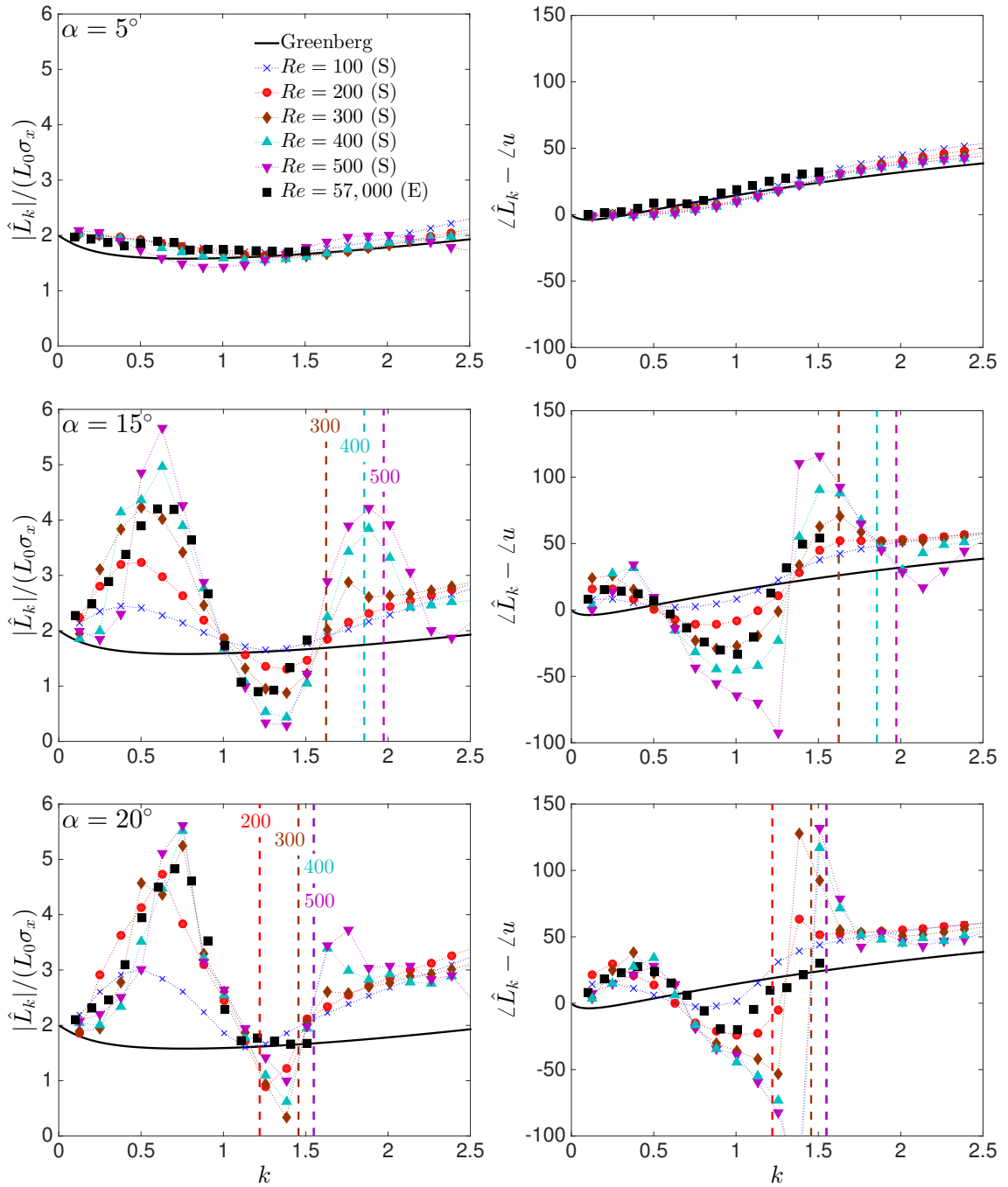


Figure 3.7: Amplitude (left) and phase (right) of the fluctuating lift at various  $Re$  and  $\alpha$ . Simulation results (S),  $Re \in [100, 500]$ , are compared with the experiment results (E),  $Re = 57,000$ . Vertical lines indicate the vortex shedding frequency of steady flow ( $\sigma_x = 0$ ) at corresponding  $Re$ . Airfoil is a flat plate for the simulations and NACA 0006 for experiments.  $\sigma_x$  was set to 0.1 for all cases.

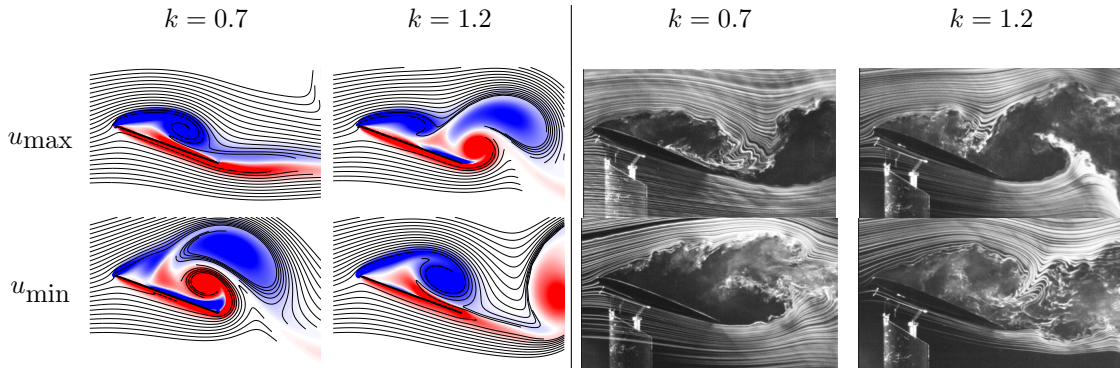


Figure 3.8: Snapshots of flow field at  $Re = 500$  (left, simulation) and  $Re = 57,000$  (right, experimental) for  $\alpha = 20^\circ$  and  $\sigma_x = 0.1$ . Top and bottom rows correspond to the flow field at the maximum  $u = U(1 + \sigma_x)$  and minimum  $u = U(1 - \sigma_x)$  velocity, respectively. Reduced frequencies are chosen to reveal flow fields when the fluctuations are amplified ( $k = 0.7$ ) and attenuated ( $k = 1.2$ ). For the simulations, streaklines are depicted on top of the color contours of vorticity,  $\omega c/U \in [-10, 10]$ .

The increasing amplification and attenuation of the fluctuating forces with increasing  $Re$  appears to be related to an increased circulation of the LEV. At least for the low  $Re$  considered in the simulations, the LEV structure becomes more distinct from the broad separated region, and the incremental lift by the LEV increases with increasing  $Re$ . Figure 3.9 and figure 3.10 demonstrates the changing vortical structure as a function of  $Re$  for both the amplification and attenuation frequency at  $\alpha = 15^\circ$ . The fluctuating feature described above becomes more prominent as increasing  $Re$ , reinforcing the amplification / attenuation behaviors. We interpret the trend with  $Re$  as suggesting that at higher  $Re$ ,  $Re > 500$ , viscous effects are becoming increasingly independent of  $Re$ . However, as we have mentioned before, two-dimensional simulations at higher  $Re$  are unrealistic due to three-dimensional instabilities, and a firm conclusion must await future three-dimensional simulations and experiments in the intermediate range of  $Re$ .

The added mass of the oscillating airfoil also contributes to the fluctuation lift. However, for the range of reduced frequencies considered, the contribution is not large enough to change the overall behavior of the fluctuating amplitude. In potential flow, the added mass lift of a surging flat plate normalized by  $L_0$  and  $\sigma_x$ , is close to  $\frac{k}{2}$  (Greenberg, 1947), and the amplitude linearly increases with the reduced frequency (equation 1.2 as  $k \rightarrow \infty$ ). Thus, at higher frequency regimes, the fluctuations are dominated by the added mass, and the curves in figure 3.7 asymptotically reach the slope of  $k = \frac{1}{2}$  with the phase of lift leading velocity by  $90^\circ$ . For the reduced frequencies considered in this

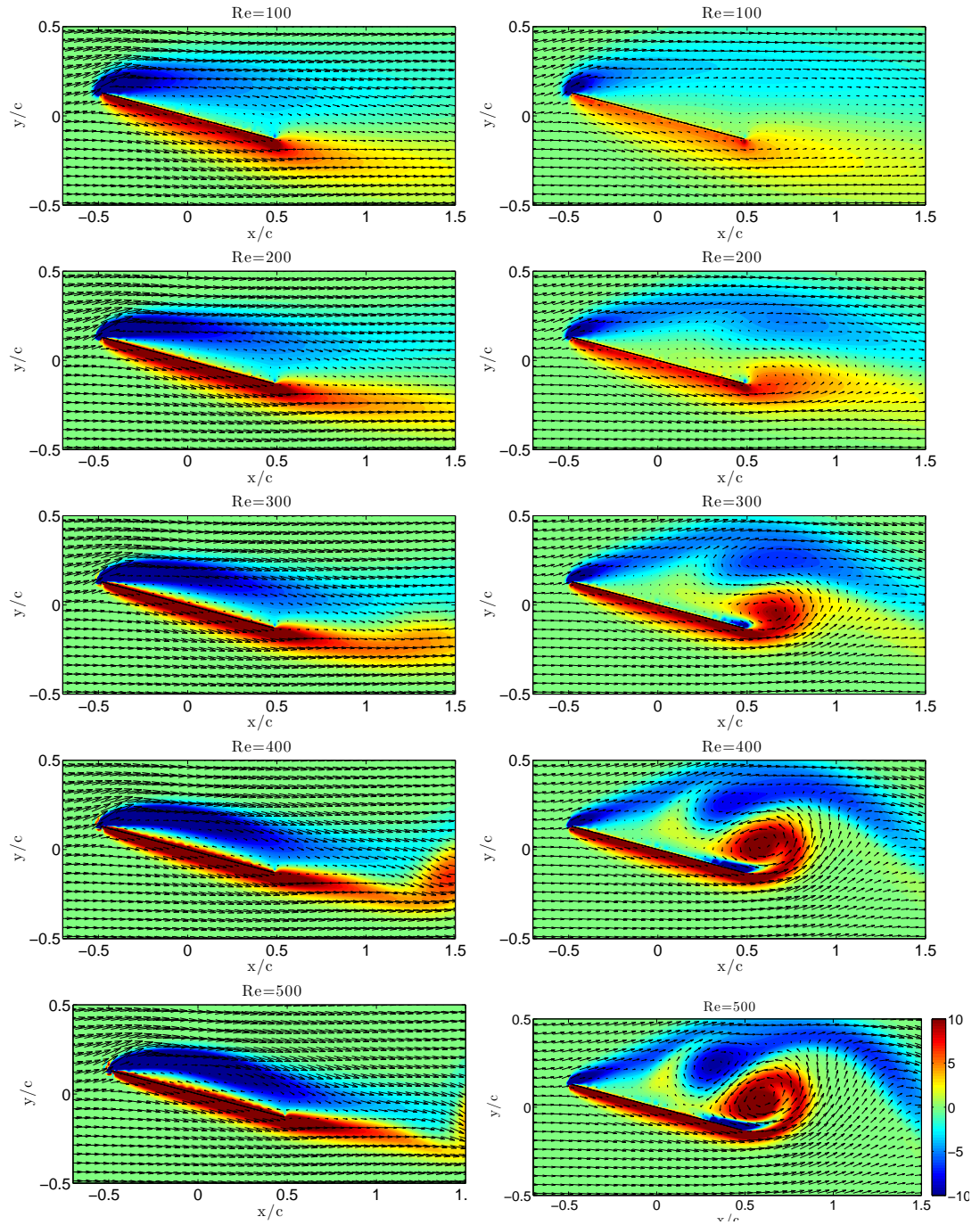
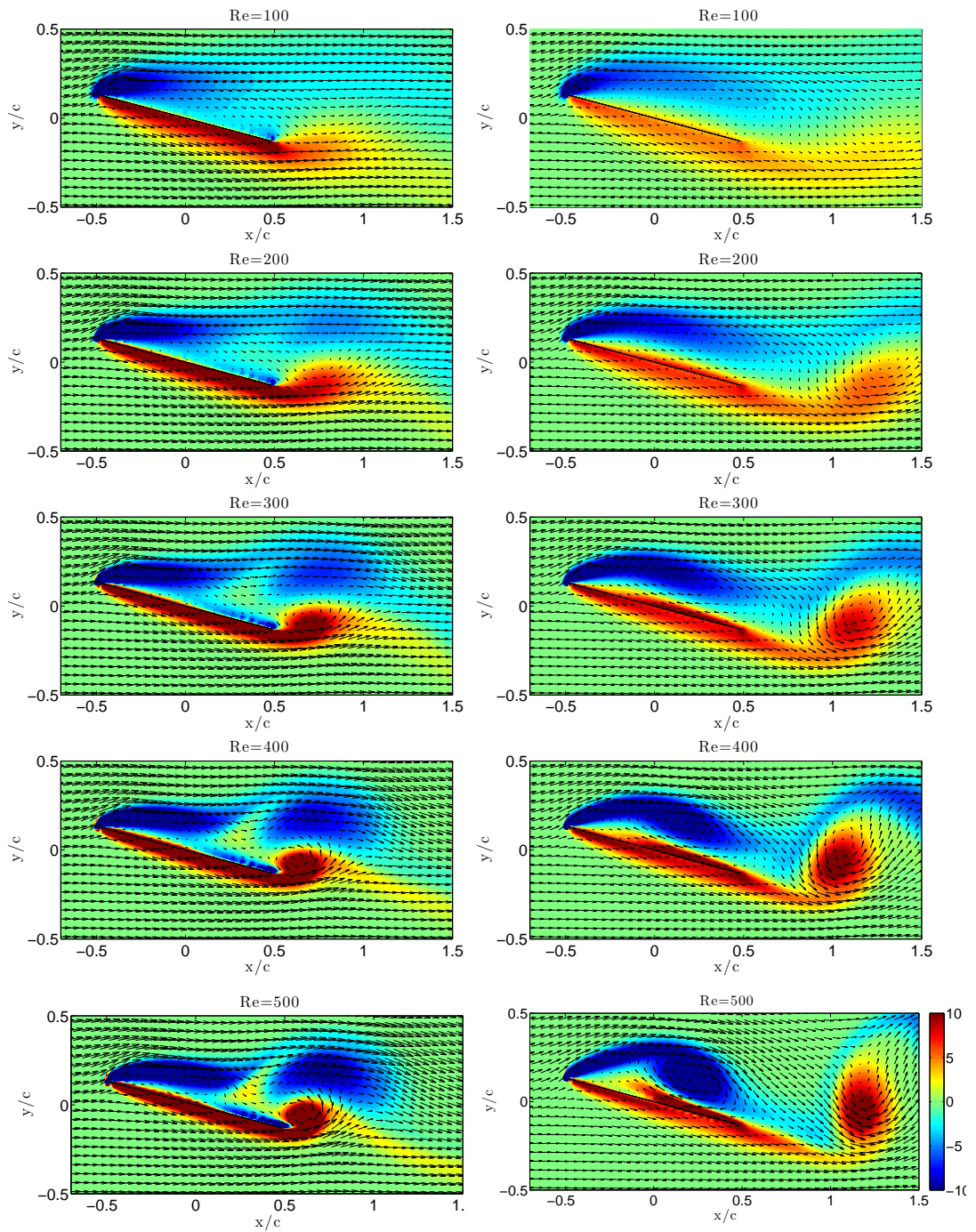


Figure 3.9: Vorticity contours and velocity vectors at various Reynolds number. Left and right columns shows the flow field at the maximum  $u = U(1 + \sigma_x)$ , and minimum  $u = U(1 - \sigma_x)$  velocity, respectively.  $\alpha = 15^\circ$ ,  $\sigma_x = 0.2$  and  $k = 0.5$ .

Figure 3.10: Same as figure 3.9 but at  $k = 1.26$ .

study, the fluctuations caused by the circulatory forces are much larger than the added mass, and the amplification / attenuation of the fluctuating forces can be solely described by the generation of LEV acting in- or out-of-phase with the oscillations.

For extremely low  $k$  values, the normalized amplitudes asymptotically reach a value of 2 (equation 1.2 as  $k \rightarrow 0$ ) for all cases, and the phase difference between lift and velocity disappears. In this low frequency regime, all dynamical effects are negligible, and lift is determined by the quasi-steady circulatory lift. This behavior was also discussed in Andro & Jacquin (2009).

### 3.2.3 LEV growth and detachment

In this section, we quantify growth and detachment of LEV by applying vortex identification methods and tracking the reattachment point along the upper surface of the airfoil. Figure 3.11 plots the circulation and phase of the LEV at the moment it is shed. Circulation,  $\Gamma/(Uc)$ , was measured based on the the vortex identification method proposed by Graftieaux *et al.* (2001), which captures the coherent swirling pattern in the velocity field. A vortex is defined as a region where  $|\Gamma_2|$  is larger than  $2/\pi$  (where rotation dominates shear) and we state the occurrence of LEV detachment as the time when the level set of  $|\Gamma_2| = 2/\pi$  separates into two closed contours near the leading-edge.  $\Gamma_2$  at a point  $P$  is defined as,

$$\Gamma_2(P) = \frac{1}{S} \int_{M \in S} \frac{[\mathbf{PM} \times (U_M - \bar{U}_P)] \cdot \mathbf{z}}{\|\mathbf{PM}\| \cdot \|U_M - \bar{U}_P\|} dS, \quad (3.4)$$

where  $S$  is the area around  $P$  and  $\bar{U}_P = (1/S) \int_S U dS$ .  $M$  lies in  $S$  and  $PM$ ,  $U_M$  are the radius vector from P to M, and the velocity vector at  $M$ , respectively. Measured circulations in figure 3.11 also represent the maximal circulation of the LEV; its strength continuously decreases as it convects downstream after shedding. The vortex strength measurement and its phase of detachment are consistent with what Baik *et al.* (2012) have observed experimentally over the range of  $Re = 5,000 \sim 20,000$  with their plunging and pitching airfoil. The size and strength of the forming LEV decreases with increased reduced frequency, and it also separates later during the phase of velocity. The

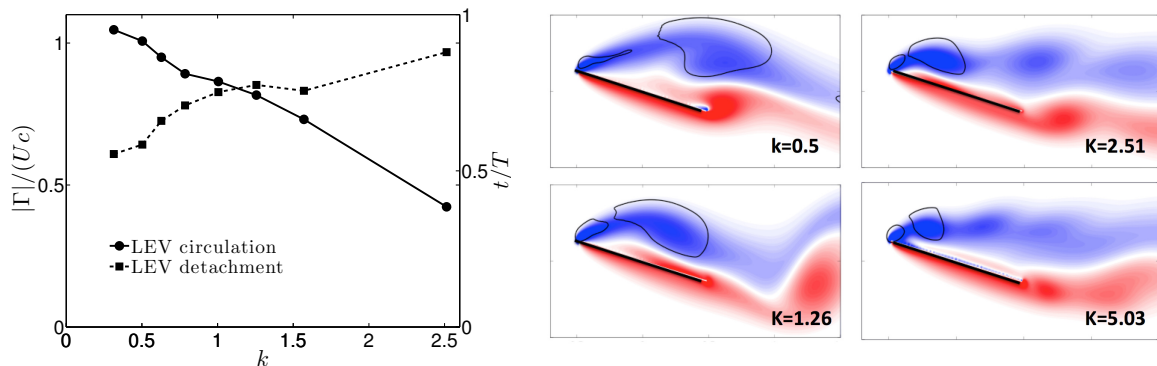


Figure 3.11: Strength of maximum shed LEV and its occurring phase. Snapshots reveal the strength and size decreasing with increasing  $k$ . Flat plate,  $\alpha = 15^\circ$ ,  $Re = 300$  and  $\sigma_x = 0.2$ .  $\omega c/U \in [-10, 10]$ .

flow topology is mostly determined by the reduced frequency,  $k$ , but to a lesser degree on Strouhal number,  $St_A = \sigma_x/\pi$ . This implies that the reduced frequency, which is the ratio of convective time scale to the surging period, determines the characteristic time for the LEV to develop and separate.

The growth of the LEV before separation can also be investigated by the location of the reattachment point reaching the trailing edge. Rival *et al.* (2013) defined the occurrence of LEV detachment as the instant where the rear stagnation point arrives at the trailing edge, since after its arrival, trailing-edge vortices are rapidly fed to cut off the LEV and limit its growth. Figure 3.12 plots the stagnation points at the upper surface of the airfoil for  $k = 0.25, 0.5, 0.78$ , and  $1.26$  at  $\alpha = 15^\circ$ . Vorticity values are measured at the upper surface, and the reattachment point is assumed to occur at the position where the vorticity changes from positive to negative (Rival *et al.*, 2013). Although this is not a rigorous definition of a reattachment point for the unsteady flow, the reattachment point is evolving slowly enough such that the stagnation points evaluated by the instantaneous vorticity field can provide useful information about the regions where the flow converges or diverges. An examination of the flow fields reveals that at about  $k = 0.5$ , the flow reattaches to the surface (there is no reattachment point for  $k = 0.25$ ), and forms a laminar separation bubble that remains for a certain portion of the cycle. This bubble grows until the reattachment point reaches the trailing edge, and the growth of LEV and its detachment coincide with its arrival to the trailing-edge. In figure 3.12, the rear stagnation point can be traced by the white line in the contour plot during the advance portion of the cycle,  $0 < t/T < 0.5$ . The reattachment point has reached the trailing-edge

at  $t/T = 0.25$  for  $k = 0.5$ . However, for  $k = 1.26$  LEV extends its length to only half of the chord length. After the arrival of reattachment point, the LEV detaches, and this event is just encountered at  $k = 0.5$ , while, on the other hand, for  $k = 0.78$  and  $1.26$ , this is delayed until  $t/T = 0.3$  and  $0.5$ .

### 3.3 Plunging

We now compare the aerodynamic forces for plunging and surging oscillations, and show that they are qualitatively similar. Quantitatively, for the same unsteady velocity amplitude,  $\sigma_x = \sigma_y$ , plunging generally produces a higher fluctuating amplitude of lift than surging, which seems natural as it has a larger added mass lift and the effective angle of attack now also changes with the oscillating velocity. For plunging, lock-in still occurs near the vortex shedding frequency and its sub harmonic, and there is an increment of the time-averaged forces within these regions. Fluctuating forces moreover show the same amplification and attenuation regimes depending on the LEV acting constructively or destructively with the phase of velocity.

#### 3.3.1 Time-averaged lift

For plunging motions, unsteady flows with wake instability can also lock-in to the harmonic components of the oscillating motion when the reduced frequency of plunging is close to the vortex shedding frequency,  $k_{VS}$ , or to its half,  $k_{VS}/2$ . These phenomena have been described above for the surging case, and previous studies (Young & Lai, 2007; Calderon *et al.*, 2013; Cleaver *et al.*, 2011, 2013) have investigated the time-averaged lift and lock-in regions for plunging at a higher  $Re$ . Lock-in leads to local maximum lift coefficients near the wake instability and its sub- or super-harmonics. Figure 3.13 compares the time-averaged lift and lock-in regions for plunging at  $Re = 300$ . We look at phase plots and frequency spectra of lift, and define lock-in as it was discussed for the surging case above.

In figure 3.13, there is an increment of the time-averaged lift when the wake instability locks on to the frequencies regarding the motion. Lock-in regions that originate from  $k_{VS}/2$  and  $k_{VS}$ , respectively, widen with increasing  $\sigma_y$  and merge at a value near  $\sigma_y = 0.035$  for plunging. Comparing lock-in

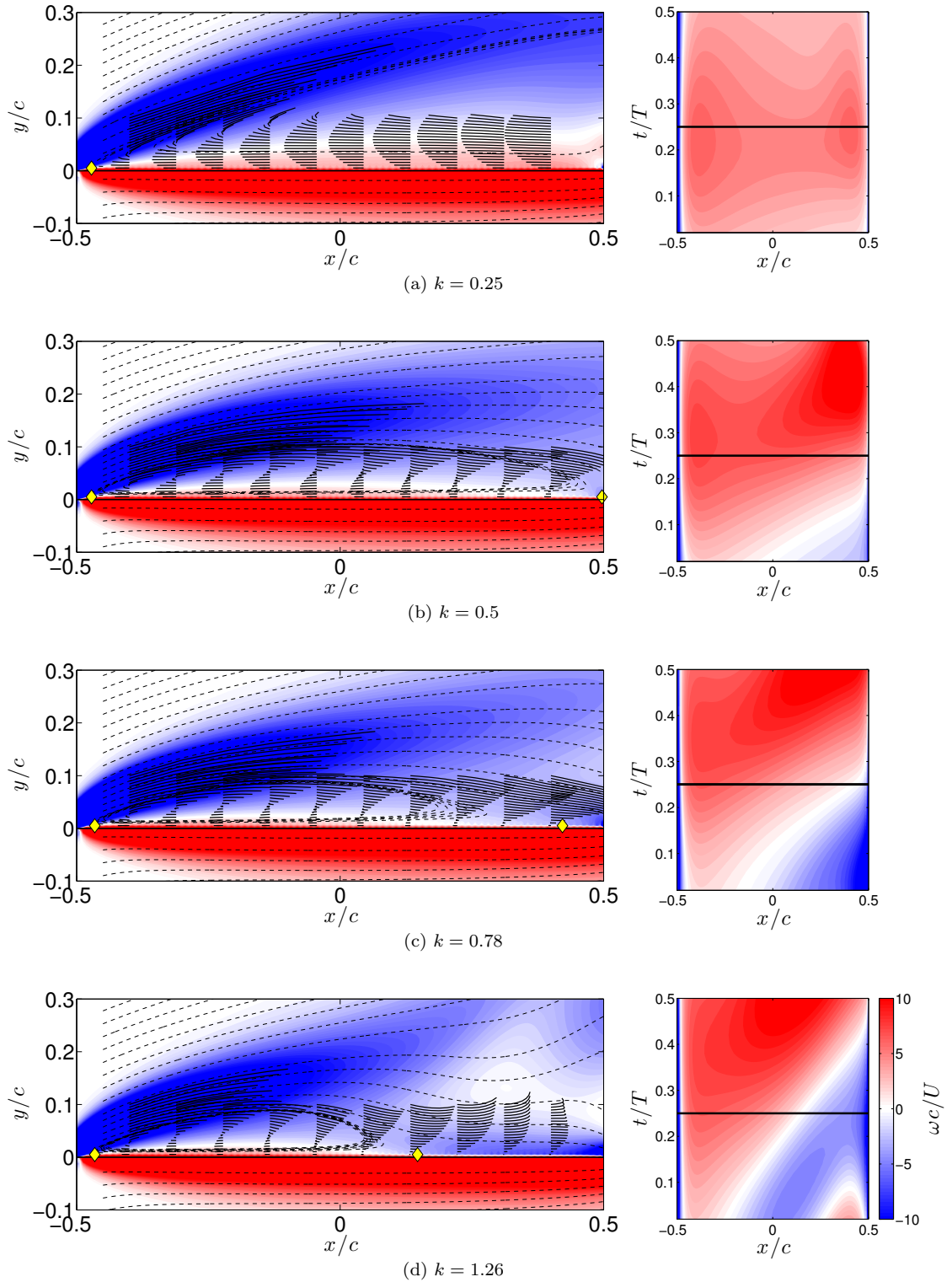


Figure 3.12: Streamlines (dashed lines), streaklines (solid lines), and stagnation points (diamond symbols) on the upper surface are plotted on top of vorticity contours at the maximum velocity,  $u = U(1 + \sigma_x)$ , for  $k = 0.25, 0.5, 0.78$ , and  $1.26$ . For each case, vorticity values on the upper surface during the advancing portion of the motion are plotted on the right. Flat plate,  $Re = 300$ ,  $\alpha = 15^\circ$ , and  $\sigma_x = 0.2$ .  $\omega c/U \in [-10, 10]$ . Flat plate is rotated  $15^\circ$  to align its chord with the x-axis.

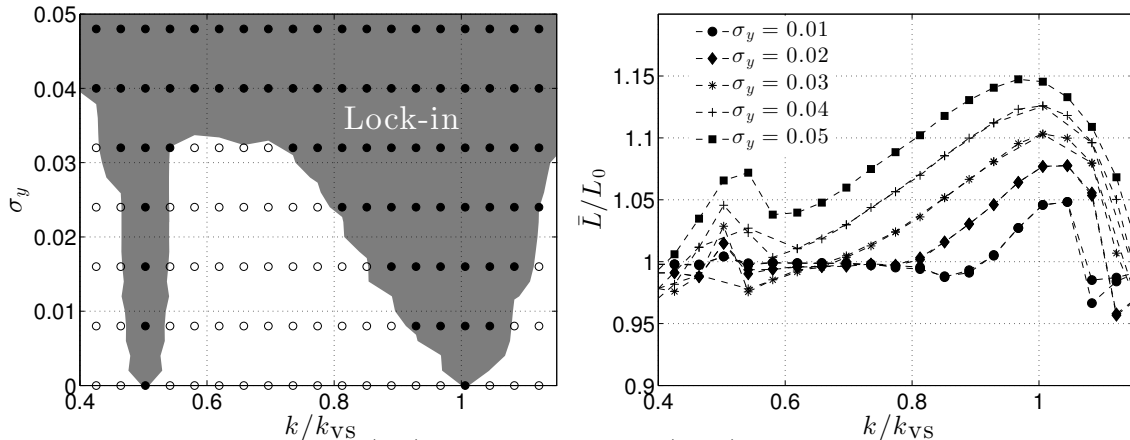


Figure 3.13: Lock-in regions (left) and mean lift force (right) for  $Re = 300$  and  $\alpha = 15^\circ$ .  $L_0$  is the mean lift for  $\sigma_y = 0$ .

regions with surging (figure 3.4), the width grows much faster for the plunging case. The resonance regions near the natural vortex shedding frequency and its sub-harmonic seem to persist over large range of  $Re$ . For example, they have been observed at  $Re = 10,000$  by Cleaver *et al.* (2011, 2013).

The time-averaged lift for plunging at higher amplitudes is investigated and shown in figure 3.14. A peak occurs at a frequency near  $k = 1.38$ , and as with surging, this peak is not related to the natural wake instability, but rather to the optimal phase of the LEV convecting along the upper surface during the upward motion (known as the ‘wake capture’ phenomenon). This phenomenon has been observed and widely addressed in previous literatures (Andro & Jacquin, 2009; Calderon *et al.*, 2013; Cleaver *et al.*, 2011, 2013).

### 3.3.2 Fluctuating lift

For surging, the amplification or attenuation were results of LEV acting on different phase of velocity, which became more pronounced with increasing  $Re$ . These phenomena also apply to the plunging case, and it is presented in figure 3.15.  $\hat{L}_k$  is the Fourier component of the fluctuating lift at the corresponding frequency of the motion,  $k$ , and the vertical lines indicate vortex shedding frequencies,  $k_{VS}$ , for the supercritical flows at  $\sigma_y = 0$ . For both surging and plunging, amplitudes are amplified and attenuated near the same frequency regime; however, for plunging, it has a much larger fluctuating amplitude than the surging case. The LEV is formed when the airfoil is moving

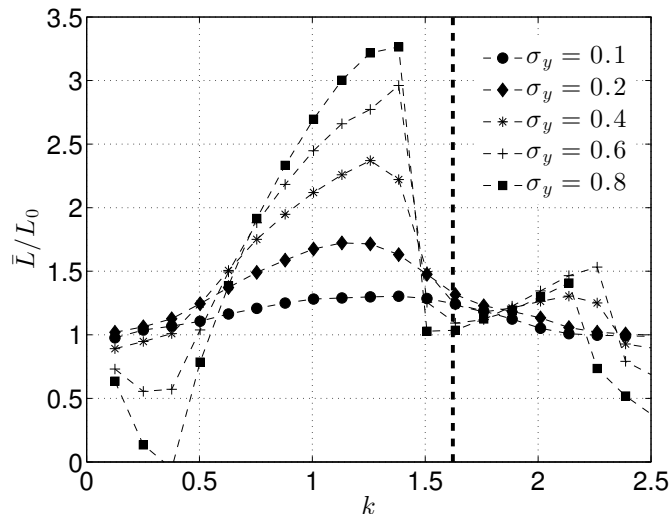


Figure 3.14: Time-averaged lift for  $0.1 < \sigma_y < 0.8$ . Vertical line indicates the vortex shedding frequency of steady flow ( $\sigma_y = 0$ ). Flat plate,  $\alpha = 15^\circ$ ,  $Re = 300$ .

downwards, and separation occurs at a later phase of the cycle with increasing  $k$ .

At  $k = 0.6$ , the low pressure region produced by LEV enhances lift during the advancing (downward) portion of the cycle, and lift at the maximum velocity is much higher than the quasi-steady case. During the retreating (upward) motion, on the other hand, the flow is encountered with a large separation region that reduces lift, and the fluctuations are amplified. For  $k = 1.2$ , where the fluctuations are attenuated, LEV induces low pressure regions above the airfoil for a longer portion of the cycle and stays close to the airfoil after it sheds. Since the shed LEV produces positive lift during the retreating (upward) portion of the oscillation, it offsets the negative quasi-steady component of lift and suppresses the fluctuations. At  $k$  values near  $k_{VS}$ , a local maximum in fluctuations can also be observed for  $Re = 400$  and  $Re = 500$ , where we expect resonance with the wake instability (lock-in).

Finally, in figure 3.16, fluctuating amplitudes of lift are presented with the variation of  $\sigma_y$ . Amplification and attenuation behaviors of the fluctuating lift, that were presented at low amplitude motions, are no longer obtained at high amplitude motions, however, are preserved for a certain degree of amplitudes.  $\hat{L}_k$ , increases almost linearly until  $\sigma_y = 0.2$  (for surging refer to figure 3.6), preserving the low-amplitude flow structures that are associated with the phase of LEV development at various reduced frequency. For  $\sigma_y$  above these values, strong interactions between the vortices and

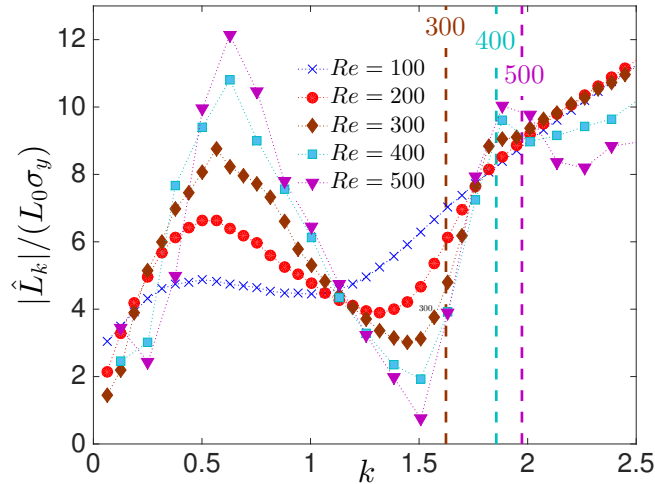


Figure 3.15: Fluctuating amplitude of lift at various reduced frequencies,  $k$ . Flat plate,  $\alpha = 15^\circ$  and  $\sigma_y = 0.05$ .

the body alters the topological structure of the flow that should be associated with high-amplitude motions.

### 3.4 Summary

In this chapter, we have investigated the unsteady aerodynamic forces and flow structures associated with harmonic oscillations superposed in the streamwise and transverse direction on a steady flow. Flows were limited to low Reynolds number near  $Re_{\text{crit}}$ , where the baseline flow first displayed wake instability, and the angle of the airfoil was sufficiently high so that the flows were fully separated. As the reduced frequency was varied, a number of interesting features that involved vortex lock-in and synchronization of the LEV with the oscillatory motion occurred.

For surging motions with relatively low amplitude, the wake instability with vortex shedding locked-in to the harmonic motion of the airfoil when the reduced frequencies were close to the vortex shedding frequency or its subharmonic. These lock-in regions, occurred within a continuous range of reduced frequencies and widened with increasing amplitude,  $\sigma_x$ , consistent with the resonance regions of a generic nonlinear oscillating known as the Arnold's tongue or resonance horn. Also, there existed a correlation with the time-averaged forces and lock-in regions, due to enhanced force

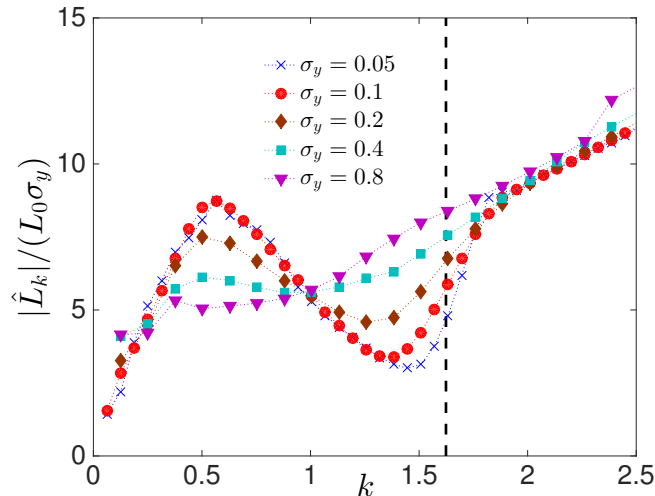


Figure 3.16: Fluctuating amplitude of lift (plunging). Aerodynamic response is nearly linear for  $\sigma_y = 0.2$ . Vertical lines indicate the vortex shedding frequency of steady flow ( $\sigma_y = 0$ ). Flat plate,  $\alpha = 15^\circ$ ,  $Re = 300$ .

in the direction normal to the flat plate. For higher velocity amplitudes,  $0.1 < \sigma_x < 0.8$ , the time-averaged peak occurred at a frequency that is not related to the natural wake instability, but rather to the optimal phase of the LEV convecting along the upper surface.

While the time-averaged forces were related to lock-in of vortex shedding, the formation of the leading-edge vortex (LEV) was found to be accountable for the amplification and attenuation of the fluctuating forces. There existed frequency regimes near  $k = 0.6$  and  $k = 1.2$  where the fluctuations were amplified and attenuated, and this behavior did not seem to be fundamentally related to wake instability, since the associated frequencies showed no significant dependence on the Reynolds number. Analysis of the flow structure revealed that fluctuating forces amplified when the incremental force by LEV added in-phase with the quasi-steady component of velocity, and attenuated when out-of-phase. At the  $k$  value associated with amplification, the LEV formed during the advancing portion of the cycle, extended to its full strength at the maximum velocity, and separated before the retreating portion of the cycle, whereas at the higher  $k$  value associated with attenuation, LEV developed for a much longer period of the cycle that separated during the retreating portion of the cycle. After this separation, it remained close to the airfoil and produced additional lift that cancels out the negative component of quasi-static lift and, therefore, suppressed

the fluctuations.

The reduced frequency,  $k$ , was identified as a parameter that controls the arrival of the reattachment point to the trailing edge, which in turn governs the growth of LEV and also its detachment. Applying a vortex identification method and tracking the reattachment points on the upper surface, we have shown that the strength of the LEV diminished and the phase of the detachment delayed with increasing reduced frequency. For the range of parameters concerned, the structure of the flow was mostly governed by the reduced frequency, and this parameter, which represents the ratio of convective time scale to the surging period, was believed to determine the characteristic time for the LEV to develop. A detailed study of the flow including snapshots of streamlines and vorticity fields revealed that the arrival of the rear stagnation point is delayed with increasing reduced frequency.

The aerodynamic forces that are associated with plunging motions were shown to produce similar behavior to the surging case, where lock-in occurred near the vortex shedding frequency and its sub harmonic, and fluctuations amplified or attenuated depending on the phase of LEV acting constructively or destructively with the quasi-steady component of the forces. These amplification / attenuation frequency regimes coincided with the ones in surging.

## Chapter 4

# High-Amplitude Surging Airfoils

In this chapter, we numerically investigate the unsteady aerodynamic forces and the vortical structures occurring during high-amplitude oscillations of a surging airfoil ( $\sigma_x > 0.2$ ). The emphasis in this chapter is on the behavior of the mean aerodynamic forces, particularly the lift. The same case was studied experimentally by Gursul & Ho (1992), who found a significant mean lift enhancement, compared to a steadily moving airfoil, over a range of reduced frequencies,  $0.8 < k < 1.0$ . They attributed this peak to a wake capturing phenomenon, where the LEV shed during the advancing phase of oscillation advects with (stays near) the airfoil during the retreating phase of the cycle. Here we investigate the mechanisms of lift enhancement by using techniques to identify, track, and measure the strength of any LEV that is formed during the oscillating motion, and describe the mechanism that leads to the peak frequency in a different aspect.

### 4.1 Problem description

As with in chapter 3, we implement the immersed boundary fractional-step method with the geometry of the airfoil as a flat plate. Aerodynamic forces of fully separated flows are less sensitive to the shape of the airfoil, and we compare the results of a flat plate to NACA 0012 used in Gursul & Ho (1992). The angle of attack of the airfoil is  $\alpha = 20^\circ$ , and the Reynolds number is set to  $Re = 1000$ . There is an order of magnitude difference in the Reynolds number between our simulations and the experiments at  $Re = 50,000$  (Gursul & Ho, 1992); however, flow fields and aerodynamic forces in the range of  $Re = 10^3 - 10^4$  were found to be less affected by the change of the Reynolds number

(Ol *et al.*, 2009; Eldredge *et al.*, 2009; Lian & Ol, 2010).

The streamwise velocity of the body is specified as in equation 3.1, and most of the simulation setup, except for the grid resolution, is identical to cases in chapter 3. For this particular problem, convergence tests were performed on a grid resolution up to  $720 \times 480$ , and it was found that  $600 \times 400$  (201 points per chord length) was sufficient.

To identify and measure the vortices that occur during the motion, we apply the  $\Gamma_2$  criterion (Graftieaux *et al.*, 2001), which was also used in chapter 3. LEV circulation is measured by integrating the vorticity contained within a contour level of  $|\Gamma_2| = 2/\pi$ .

As the source of vorticity contained in the LEV originates from the leading-edge separation, the total (clockwise negative sign) vorticity generated at the leading-edge during a period is also measured. Considering a small control volume that surrounds the leading edge, the net vorticity generated during a period of the motion can be evaluated by integrating the flux that passes through the control surface. The total circulation per cycle can be computed as:

$$\Gamma = \int_0^T \oint \omega(\mathbf{u} - \mathbf{u}_b) \cdot \mathbf{n} ds dt, \quad (4.1)$$

where  $\omega$  is the measured vorticity on the control surface. The inner integration represents the flux of vorticity, where the relative velocity respect to the body,  $\mathbf{u} - \mathbf{u}_b$ , is projected to the normal direction of the control surface. The total circulation,  $\Gamma$ , can be considered as a sum of  $\Gamma^+$  and  $\Gamma^-$ , where  $\Gamma^+$  only selects the positive value of vorticity on the control surface, and  $\Gamma^-$ , the negative vorticity. Figure 4.1 presents the geometry of the control volume and vorticity flux on the control surface. The magnitude of  $\Gamma^-$  is expected to be inversely proportional to the reduced frequency as the period of the motion decreases with increasing frequency. In the following sections, as the amount of vorticity transported through the leading-edge shear layer is of particular interest, we use the term ‘total circulation’ interchangeably with  $\Gamma^-$ .

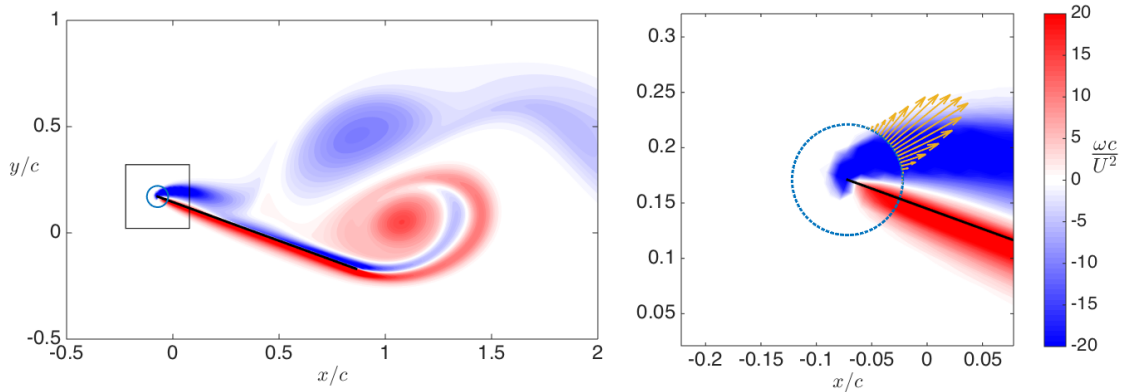


Figure 4.1: The square box near the leading edge is enlarged to show control volume geometry (region inside the dotted line) and vorticity flux of  $\omega < 0$  through the control surface. Flat plate,  $\alpha = 20^\circ$ ,  $k = 0.5$ ,  $\sigma = 0.4$  at  $Re = 1000$ .

## 4.2 Features of non-oscillatory flows at different $Re$ ( $\sigma_x = 0$ )

As the variation in the Reynolds number associated with high-amplitude motion is large, we investigate the non-oscillatory flows over a wide range of  $Re$ . Based on results from chapter 3, the critical Reynolds number,  $Re_{\text{crit}}$ , where a supercritical Hopf bifurcation occurs (Sreenivasan *et al.*, 1987), is  $Re_{\text{crit}} = 164$  for  $\alpha = 20^\circ$  (figure 3.2). Considering non-oscillatory flows of  $Re > Re_{\text{crit}}$ , figure 4.2 plots the magnitude of the discrete Fourier transform of the fluctuating lift coefficient for  $0 < Re < 2000$ . The frequency of the wake instability that corresponds to a Strouhal number (scaled with the projected chord length  $c \sin \alpha$ ) of 0.13 at  $Re_{\text{crit}}$  increases up to 0.2 at higher  $Re$ . The frequency of the wake instability remains nearly constant for  $400 < Re < 1400$ , being consistent with the results of Fage & Johansen (1927).

Above  $Re = 800$ , a subharmonic frequency of the wake instability is also excited near  $k = 1$ . In this regime, the flow is very sensitive to changes in  $Re$ , and further increasing  $Re$  leads to a chaotic flow through the route known as periodic-doubling cascade. Pulliam & Vastano (1990) observed the same behavior, computationally, on a 2D NACA 0012 airfoil at  $\alpha = 20^\circ$ , having the same cascade region of  $800 < Re < 1600$ . They reported that the subharmonic frequency above  $Re = 800$  is primarily caused by the irregular intensity of the shed vortices. Time series of lift at representative  $Re$  of 100, 500, and 1000 are shown in figure 4.3. For  $Re = 1000$ , the wavelength associated with

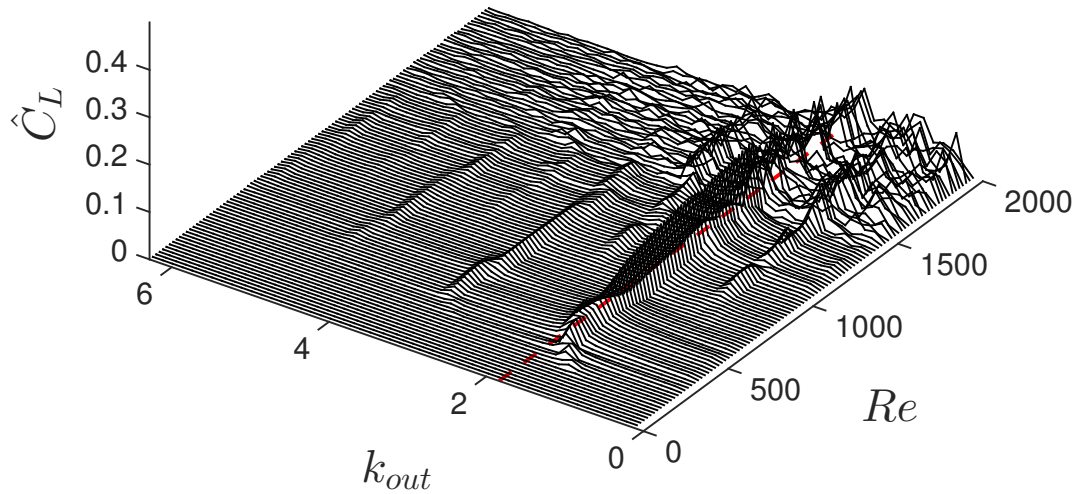


Figure 4.2: Lift spectrum of uniform flow at  $\alpha = 20^\circ$ .  $\hat{C}_L$  is the magnitude of the Discrete-Fourier Transform of the fluctuating lift coefficient. The red dashed line corresponds to a frequency of  $St_{vs} = fc \sin \alpha / U = 0.2$ .

the subharmonic frequency of the wake instability is clearly visible in the difference of the peak magnitudes.

In figure 4.4, the mean lift and drag coefficients of uniform flows are also examined over the range of  $0 < Re < 1700$ . At very low  $Re$ , the drag coefficient is asymptotically proportional to the inverse of the Reynolds number, and above  $Re_{crit}$ , the drag coefficient stays nearly constant for a wide range of  $Re$ .  $\bar{C}_L$  has a minimum value at  $Re_{crit}$ , and increases nearly monotonically with  $Re$ . The small oscillations evident at the highest  $Re$  are associated with a lack of convergence of the mean over the time series of the simulation, which is in turn related to sensitivity of the chaotic flow regime to the exact averaging period.

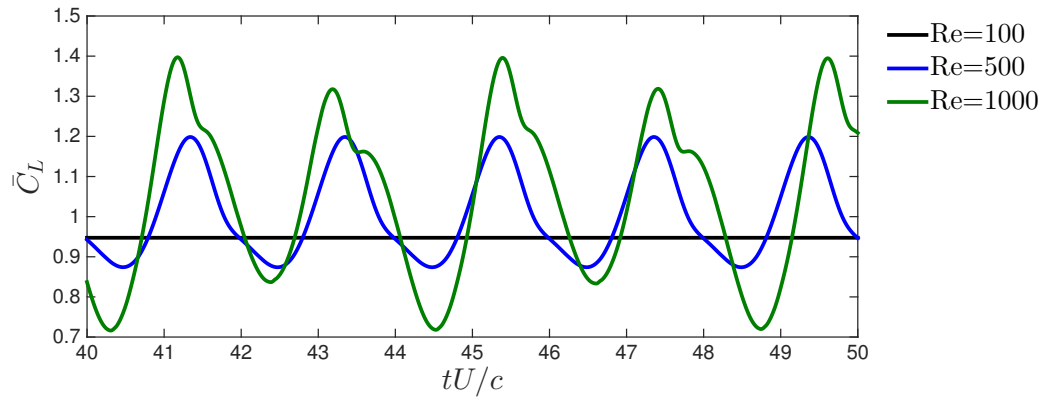


Figure 4.3: Time history of lift coefficient at  $Re = 100, 500,$  and  $1000$ .

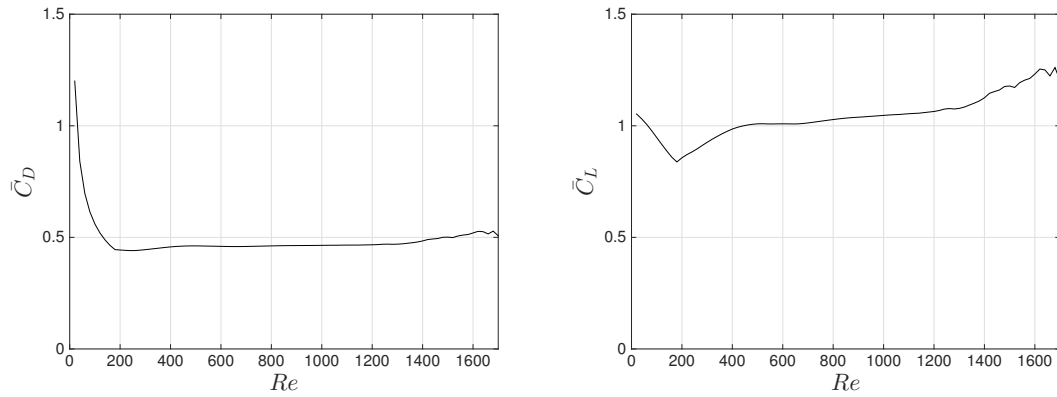


Figure 4.4: Mean drag (left) and lift (right) coefficients of uniform flow at  $\alpha = 20^\circ$ .

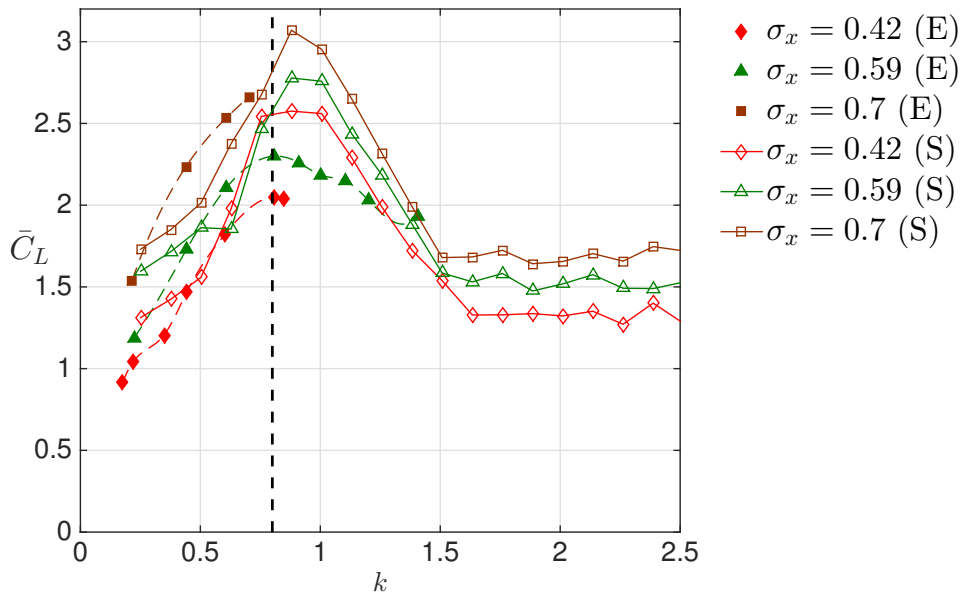


Figure 4.5: Time-averaged lift coefficient,  $\bar{C}_L$ , of streamwise oscillating flow at various reduced frequencies ( $\alpha = 20^\circ$ ). Simulation (S) are run at  $Re = 1000$  and compared with experimental data (E) from Gursul & Ho (1992),  $Re = 5 \times 10^4$ . Dashed line corresponds to the frequency of maximum lift of experiment results (at  $k = 0.8$ ). The time-averaged lift coefficient of uniform flow at  $Re = 1000$  is  $\bar{C}_{L0} = 1.15$ .

### 4.3 Forces and flow fields

Figure 4.5 plots the time averaged lift coefficient,  $\bar{C}_L = 0.5\bar{L}/\rho U^2 c$ , as a function of the reduced frequency,  $k$ , for a range of amplitudes, and includes data from experiments at  $Re = 5 \times 10^4$  (Gursul & Ho, 1992). Despite the significant difference in Reynolds number, the trends are similar and the peak of mean lift occurs at a frequency near  $k = 0.8$ . The maximum  $\bar{C}_L$  of  $\sigma = 0.7$  (at  $k = 0.9$ ) is almost three times larger than the baseline lift coefficient ( $\bar{C}_{L0} = 1.15$ ) corresponding to non-oscillatory flow. Mean drag has the same behavior as the mean lift, i.e., it is the normal force that is enhanced at the peak.

Flow visualizations near the peak frequency, at  $k = 0.75$  (simulations) and  $k = 0.7$  (experiments), are shown at  $Re = 1000$  and  $Re = 50,000$ , respectively, in figure 4.6 for  $\sigma_x = 0.7$ . Instantaneous streamlines and vorticity fields from the simulations are compared to instantaneous streamlines as approximated by the time-lapse motion of air bubbles from the experiments at four different phases of oscillation velocity. The maximum velocity,  $u_{\max} = U(1 + \sigma_x)$ , occurs at  $t/T = 0.25$ , and the

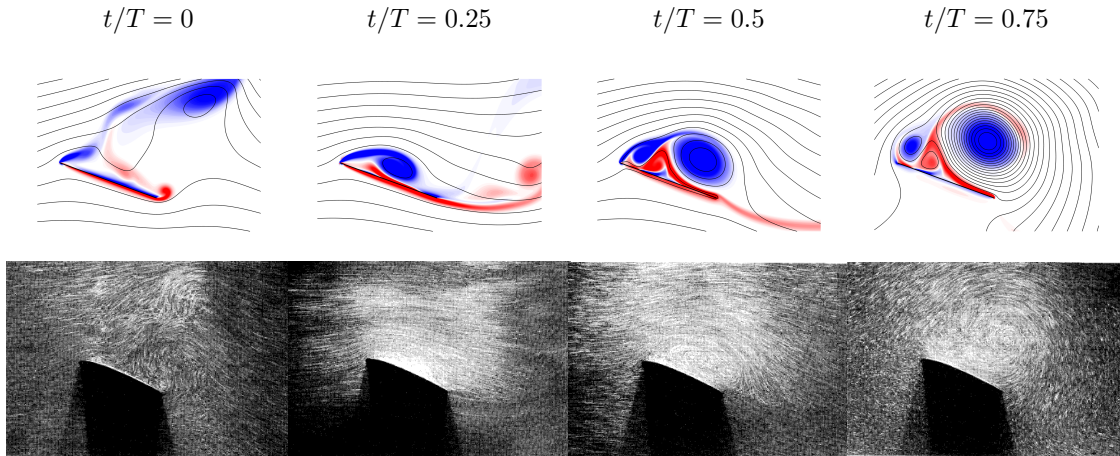


Figure 4.6: Snapshots of flow fields at  $Re = 1000$  (top, simulation) and  $Re = 50,000$  (bottom, experimental) for  $\sigma_x = 0.7$ . The reduced frequencies for the simulation and experiment are  $k = 0.75$  and  $k = 0.7$ , respectively. The maximum velocity,  $u_{\max} = U(1 + \sigma_x)$ , occurs at  $t/T = 0.25$  and the minimum velocity,  $u_{\min} = U(1 - \sigma_x)$ , at  $t/T = 0.75$ . Vorticity contours and streamlines are compared to experimental flow visualizations (Gursul & Ho, 1992).  $\omega c/U \in [-20, 20]$ .

minimum,  $u_{\min} = U(1 - \sigma_x)$ , at  $t/T = 0.75$ .

At the beginning of the advancing phase ( $t/T = 0$ ), the vortices generated during the previous period are located far from the airfoil. The leading edge shear layer rolls up during the early phase of the advancing portion, and the vortical structure is similar to the flow of an impulsive starting airfoil (see, for example, Chen *et al.* (2010)). Without any interaction or disturbance from previous shed vortices or shear layers, the airfoil grows a strong LEV for a significant portion of the period ( $0 < t/T < 0.5$ ).

During the retreating period ( $0.5 < t/T < 1$ ), this shed LEV stays near the airfoil and induces a low pressure region that is favorable for lift. Gursul & Ho (1992) hypothesized that the peak in the time-averaged lift is primarily associated with the wake capturing during the retreating portion of the period, and for the remaining sections, we make an effort to understand the mechanisms that lead to this result.

#### 4.4 Mechanism of mean lift enhancement

The time-averaged peak, which occurs within the frequency range of  $0.8 < k < 1.0$ , has no obvious relation to the frequency of the natural wake instability. Figure 4.2 shows that over the range of

Reynolds numbers experienced during surging, the natural flow has  $k_{VS} \approx 1.8$ . No corresponding peak is evident in the mean lift of figure 4.5. Resonance of the natural wake instability increased the time-averaged lift for small-amplitude ( $\sigma_x < 0.2$ ) cases (chapter 3); however, for high-amplitude motions, the flow experiences a large variation in the effective Reynolds number during an oscillation period, and considering the complexity of the spectrum of the non-oscillating flow in this range of Reynolds numbers, it appears that the flow cannot lock-in to a single frequency as it did in the lower  $Re$  cases considered in chapter 3. Although the subharmonic frequency of the wake is excited at  $k \approx 0.9$  (figure 4.2), fluctuations associated with this frequency are small compared to the harmonic frequency.

Figure 4.7 shows the time history of  $C_L$  over two oscillation periods of the motion for  $\sigma_x = 0.4$  at  $Re = 1000$ . The plot focusses on the range of  $0.25 < k < 0.75$  where the mean lift increases monotonically with  $k$ . Corresponding flow fields of figure 4.7 are shown in figure 4.8 at four different phases of the motion of  $t/T = 0, 0.25, 0.5,$  and  $1$ . For  $k = 0.38$ , snapshots at  $t/T = 1, 1.25, 1.5,$  and  $2$  are additionally shown, as the flow at this oscillation frequency shows a sub-harmonic response (i.e. it is periodic over every two cycles of streamwise oscillation).

For the lowest frequency of  $k = 0.25$ , the changes in velocity are gradual compared to the vortex dynamics, and the acceleration associated with the motion is apparently not high enough to cause the shear layer to roll-up during the advancing phase of the period. The shear layer rather convects downstream until it reaches the trailing edge and interacts with the TEV exhibiting features that are similar to the non-oscillatory flow at  $\sigma_x = 0$ . Increasing the frequency to  $k = 0.38$ , there exists a large increment of lift associated with the LEV, but only occurring at every two periods of the motion. Flow fields at  $1 < t/T < 2$  show similar wake structures to the case of  $k = 0.25$ , but, at  $0 < t/T < 1$ , the shear layer rolls up and develops a strong LEV at the early phase of the advancing motion, during every other period. Increasing the frequency further to  $k = 0.63$ , a strong LEV is formed at every period of the oscillations. Note that the maximum lift of  $C_L = 4$  is nearly the same for  $0.38 < k < 0.75$ , but the peak covers a much wider portion of the period with increasing  $k$ .

Finally at  $k = 0.75$ , the lift during the retreating portion of the cycle is significantly increased,

leading to an increase in the time-averaged lift. It is similar to what was observed in the low amplitude surging of chapter 3, and corresponds to the ‘attenuation’ regime of fluctuating lift, since the lift enhancement occurs out-of-phase with the surging. The airfoil continuously interacts with the LEV at this frequency, first growing a large vortex at the advancing phase of the motion, and keeping it close after it is shed during the retreating phase. As the incremental lift of LEV covers a wide portion of the period and wake capturing occurs during the retreating phase, there is a peak in the time-averaged lift.

Figure 4.9 shows series of snapshots of the growing LEV at  $k = 0.38, 0.63$  and  $0.75$ . The LEV grows for a much longer portion of the period as the reduced frequency becomes close to the peak of mean lift.

As the portion of the lift attributable to the LEV increases with  $k$ , there seems to be an inherent time scale related to the formation and detachment of the LEV that is not affected by the reduced frequency. Gharib *et al.* (1998) measured the strength of a vortex ring and concluded that the maximum circulation is reached when the formation time is close to 4. In his study, the formation time was defined as  $T^* = L/D$ , where  $L$  is the distance traveled by the piston, and  $D$  the diameter of the nozzle. Various studies were able to generalize this phenomenon to unsteady motion of bluff bodies (Milano & Gharib, 2005; Dabiri & Gharib, 2005; Dabiri, 2009; Chen *et al.*, 2010), and we apply this concept to our surging airfoil. Following Milano & Gharib (2005), a dynamic, non-dimensional formation time is defined as,

$$T_{df}(t) = \int_{t_0}^t \frac{U}{c} (1 + \sigma_x \sin(2k\tau U/c)) d\tau, \quad (4.2)$$

where we have replaced the projected chord length,  $c \sin \alpha$  with the chord itself, as we find that the chord length better describes vortex formation in this flow field. Topologically, the LEV detaches when the rear stagnation point reaches the trailing edge, and the growth of the LEV is limited by the chord length (Rival *et al.*, 2013). In equation 4.2,  $t_0$  is arbitrary, as we are considering the (periodic) steady-state after a certain amount of time has passed. The function  $T_{df}(t)$  is shown schematically

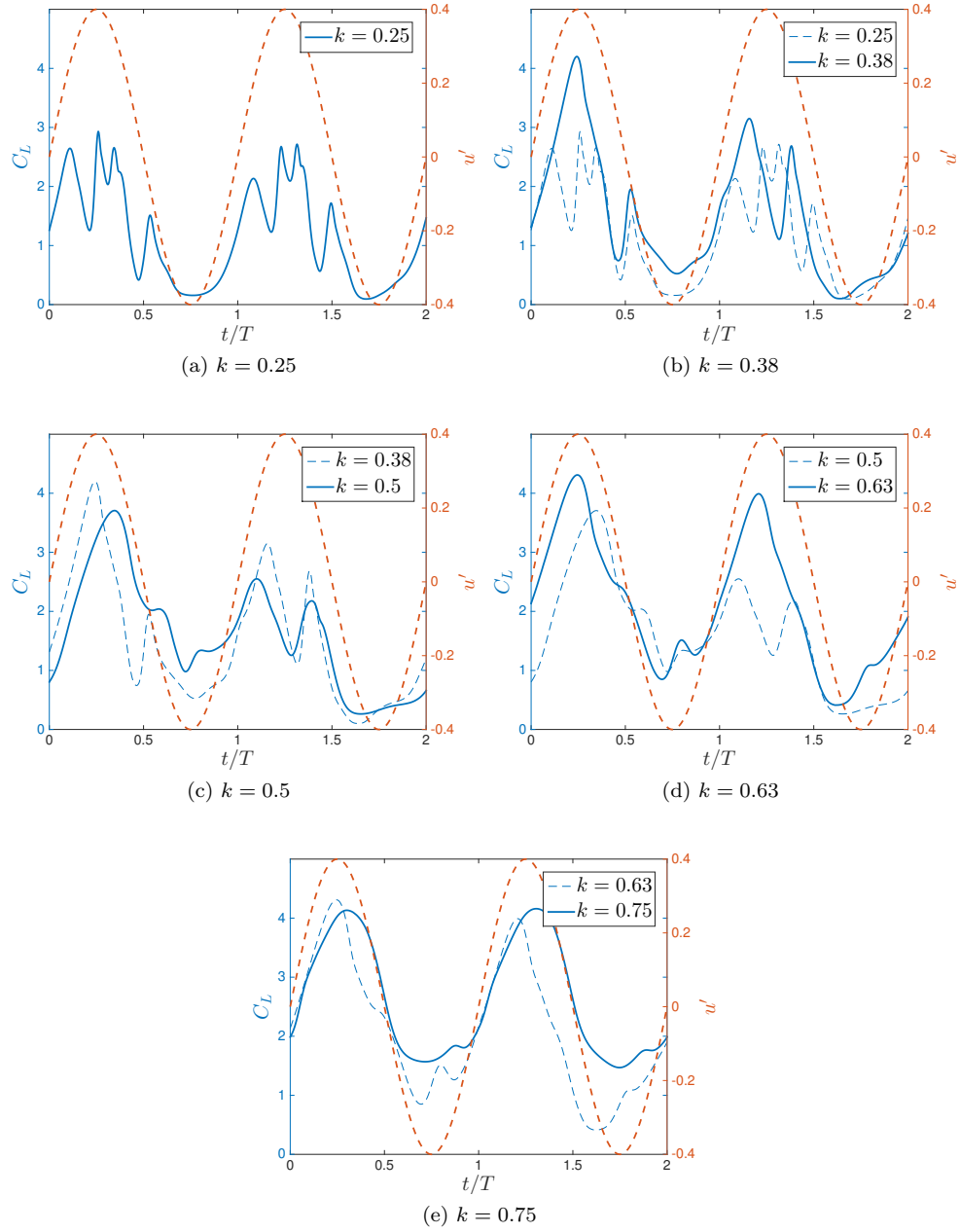


Figure 4.7: Time history of lift coefficient,  $C_L$ , for 2 oscillating periods of the motion. Increasing sequence of reduced frequency from  $k = 0.25$  to  $k = 0.75$ .  $u'$  is the fluctuating velocity of the airfoil's motion.  $\alpha = 20^\circ$ ,  $Re = 1000$ , and  $\sigma_x = 0.4$ .

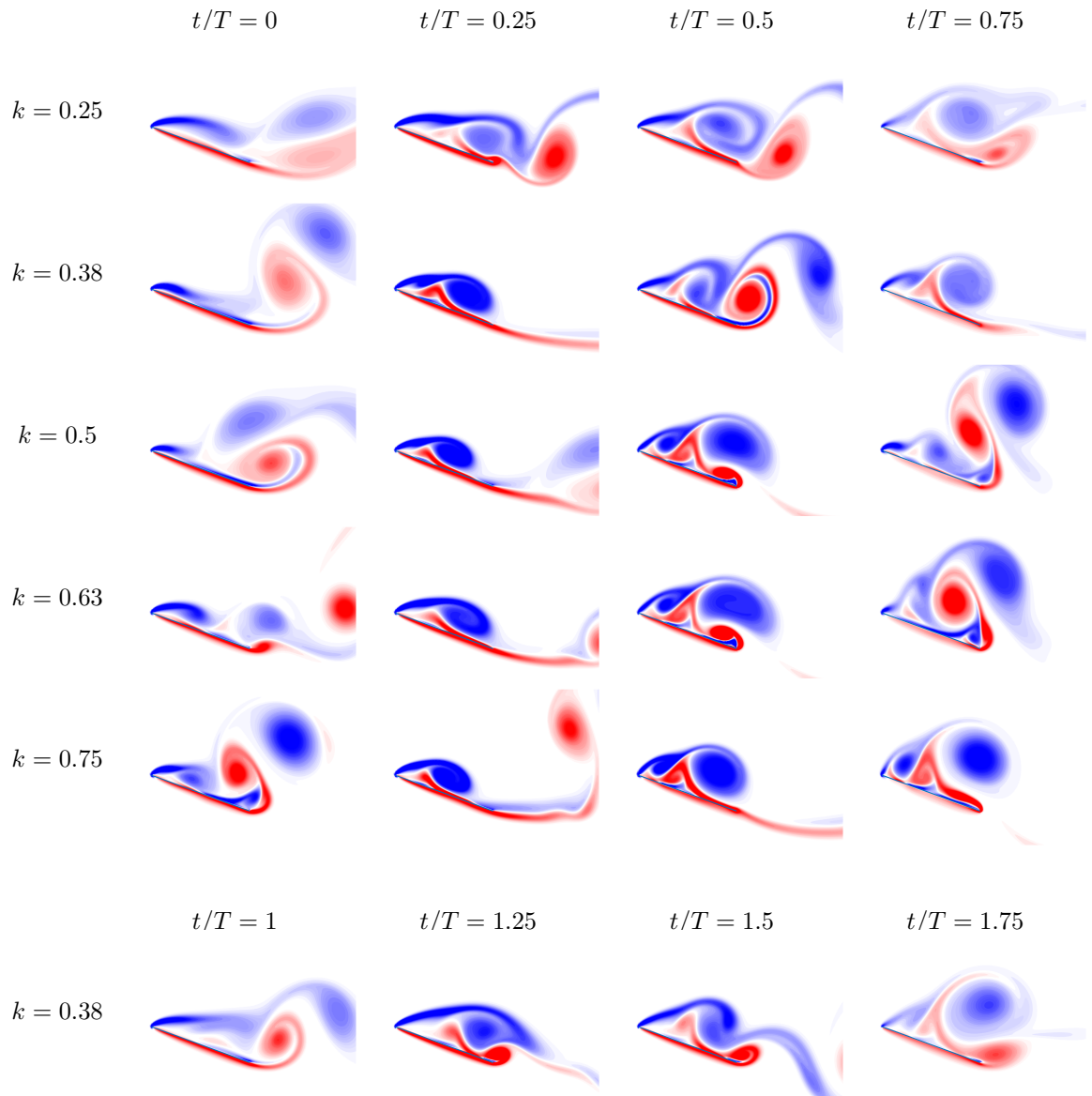


Figure 4.8: Corresponding flow field of figure 4.7.  $\omega c/U \in [-20, 20]$ .

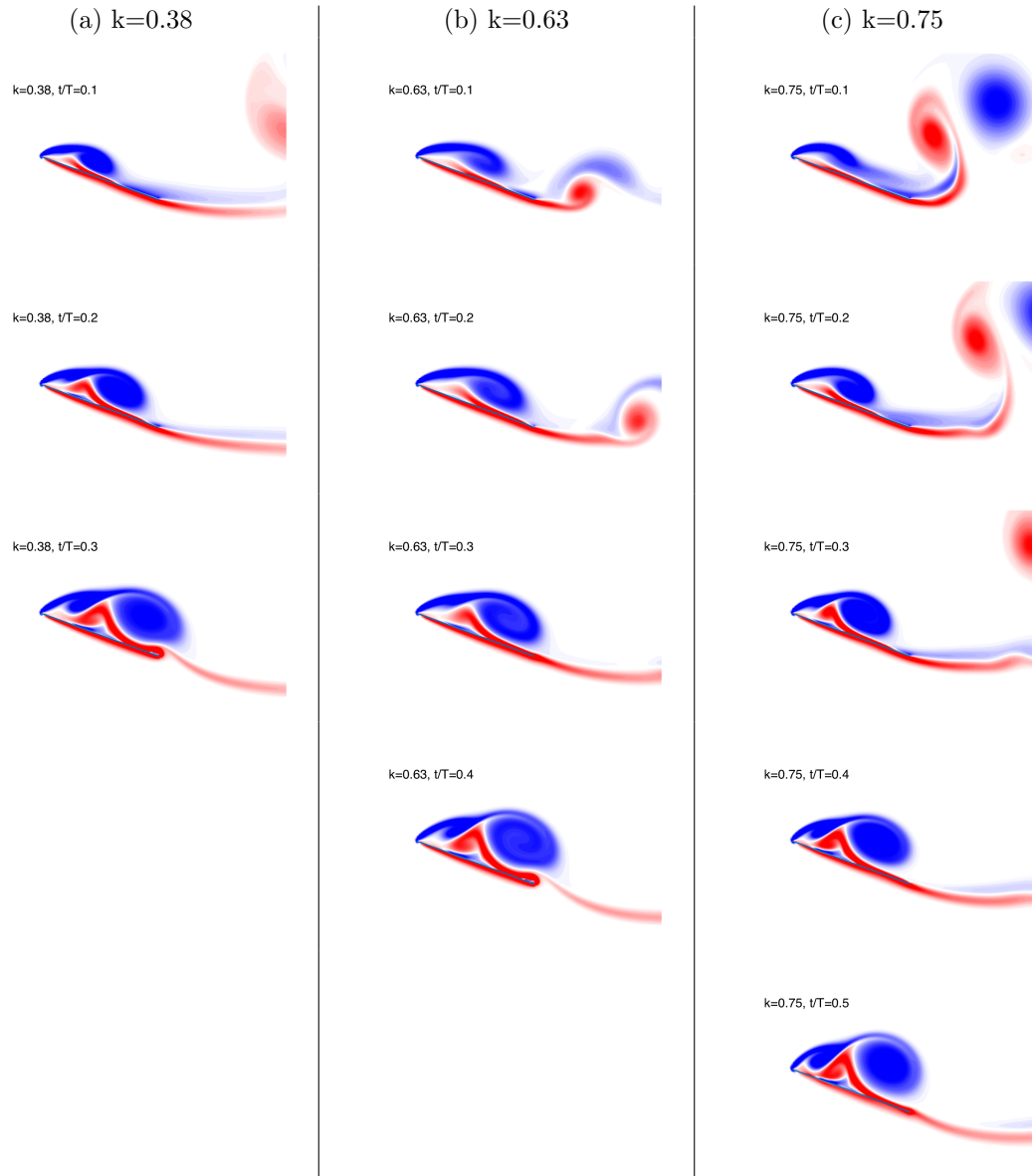


Figure 4.9: LEV formations during the advancing period.  $\alpha = 20^\circ$ ,  $Re = 1000$  and  $\sigma_x = 0.4$ .

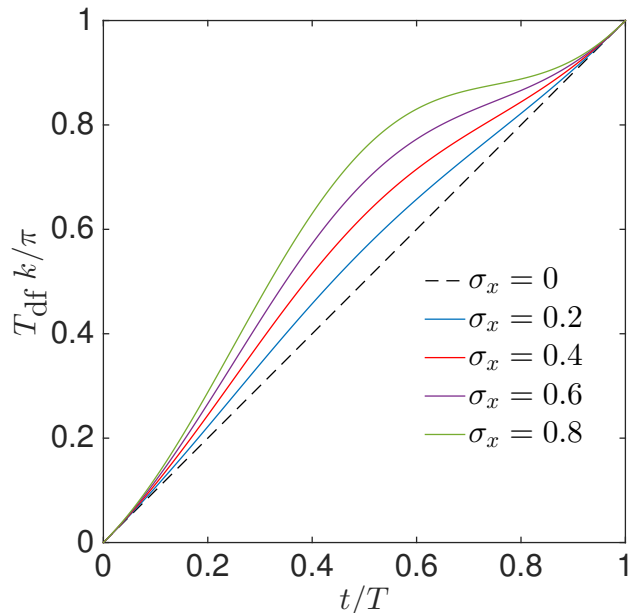


Figure 4.10: The dynamic formation time,  $T_{df}$ , at various  $\sigma_x$ . The dynamic formation time is measured from the start of the advancing phase, i.e.,  $t_0 = 0$ .

for a period in figure 4.10 for various amplitudes of the motion. To determine the formation time of the LEV, there are several different possibilities to consider depending on the values of  $k$  and  $\sigma_x$ . For sufficiently large  $k$  and  $\sigma_x$ , we expect a LEV to be shed once per period. Moreover, the shedding can be initiated by the retreating phase of the motion rather than the LEV having reached its maximum circulation. That is, we evaluate  $T^* = T_{df}(t_0 + T) = \pi/k$ . This limit is depicted in figure 4.11. For values of  $k$  less than a critical value,  $k^*$ , the LEV will reach its critical value and shed before the oscillation cycle is complete. In this case, it is unclear how to choose  $t_0$  and  $t$  in the dynamic formation time since there can be a phase shift between the time at which the nascent LEV is forming and the (arbitrary) phase associated with the beginning of the advancing phase of the motion. However, having measured the strength of the LEV based on the  $\Gamma_2$  criterion (equation 3.4), we can take  $t_0$  and  $t$  as the respective times at which the minimum and maximum circulation are measured.

Figure 4.11 plots the resulting LEV formation time,  $T^*$  as a function of  $k$ . As expected, the LEV formation time reaches a plateau for the lower values of  $k$  and is bounded by the period of

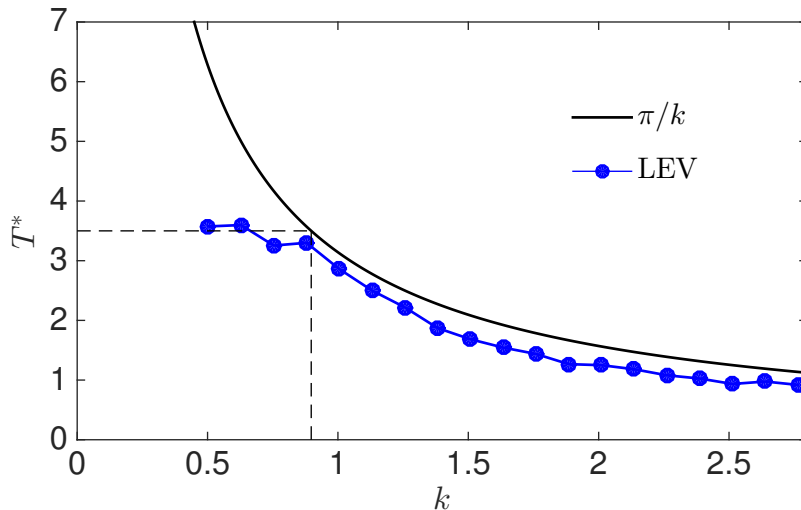


Figure 4.11: LEV formation time,  $T^*$ , is measured at various reduced frequencies (blue circle line). The formation time evaluated using the period of the motion,  $\pi/k$ , is also shown as the upper bound (black solid line). Flat plate,  $\alpha = 20^\circ$  and  $\sigma = 0.4$  at  $Re = 1000$ .

the motion for higher values of  $k$ . Based on the values, we find the limiting “universal” formation number  $T^* \approx 3.5$ , which is well within the range of values observed in previous studies of vortex formation in a variety of different flows (Gharib *et al.*, 1998; Milano & Gharib, 2005; Chen *et al.*, 2010). In figure 4.11, we have restricted the values of  $k$  to  $k \geq 0.38$ , as we find that it becomes more difficult to identify a distinct minimum and maximum circulation during each period of motion. For  $\sigma_x = 0.4$ , when  $k < 0.38$ , we observe instead an oscillating shear layer emanating from the leading edge that does not roll-up into a distinct LEV. We expect this behavior to occur at different threshold values of  $k$  depending on the surging amplitude, but so far we have only analyzed the  $\sigma_x = 0.4$  case in detail.

In figure 4.12, the total amount of (negative sign) vorticity generated at the leading edge during a period (which is  $\Gamma^-$ ) is compared with the maximum strength of shed LEV at various reduced frequencies. For the range of  $0.38 < k < 1$ , as with the LEV formation time, the maximum strength of shed LEV is also nearly constant,  $|\Gamma| \approx 4.3$ .

In figure 4.13 and figure 4.14, snapshots of flow fields are shown at different instants in time for  $0.25 < k < 2.01$ . Time is measured from the start of the advancing motion, and the left and right arrows indicate the advancing and retreating portion of the period, respectively. The double

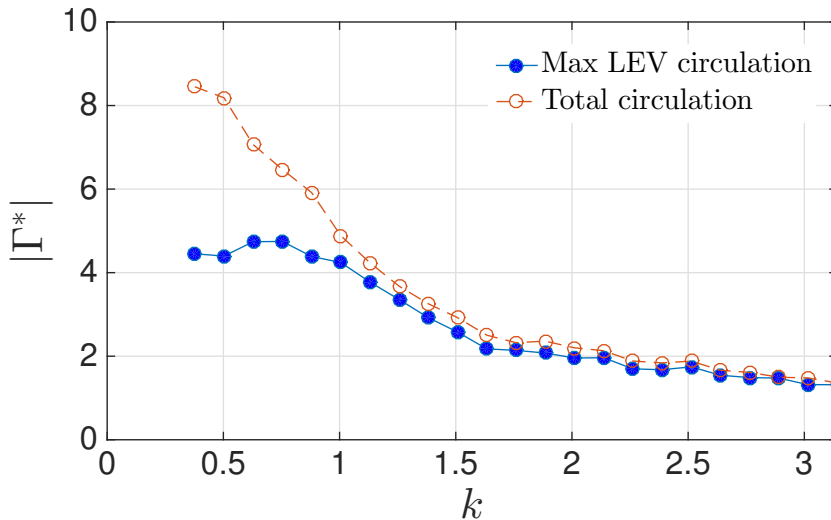


Figure 4.12: Total and max LEV circulation at various reduced frequencies. Flat plate,  $\alpha = 20^\circ$  and  $\sigma = 0.4$  at  $Re = 1000$ . Circulation is non-dimensionalized as  $\Gamma^* = \Gamma/Uc$ . For the range of  $0.38 < k < 1$ , the LEV is grown to its maximum strength and the rest of the total vorticity is analogous to the vortices in the trailing jet in the vortex ring case (Gharib *et al.*, 1998).

horizontal line denotes  $T^*$ , and the single horizontal line, the end of a period. For  $k = 0.5$ , and  $0.75$ , the LEV grows to its maximum strength. For  $k = 1.26$ , and  $2.01$ , the period ends before the formation time, and the LEV is shed before it reaches to its full strength. At  $k = 1 \approx k^*$ , the formation time just coincides with the period of the motion. At the lowest frequency of  $k = 0.25$ , we observe a separated shear layer that does not rollup into a distinct LEV, as discussed above.

## 4.5 Square waveform streamwise velocity

The time-averaged lift and vortical structures are also investigated using a square waveform of streamwise velocity. Unlike sinusoidal waveforms, square waveforms have a large acceleration at the start of the advancing phase and the initial time,  $t_1$ , of a growing LEV in equation 4.2 can be set according to this time. For square waveform velocity, we expect to detect a LEV forming during the advancing period even for the low frequency oscillations,  $k < 0.38$ . The wake structure for the sinusoidal waveform at  $k = 0.25$  was close to the non-oscillatory flow of  $\sigma_x = 0$  (figure 4.13). Figure 4.15 depicts the profile of a sinusoidal and a square wave of  $\sigma_x = 0.4$ . The square wave is smoothed using a cosine function such as,

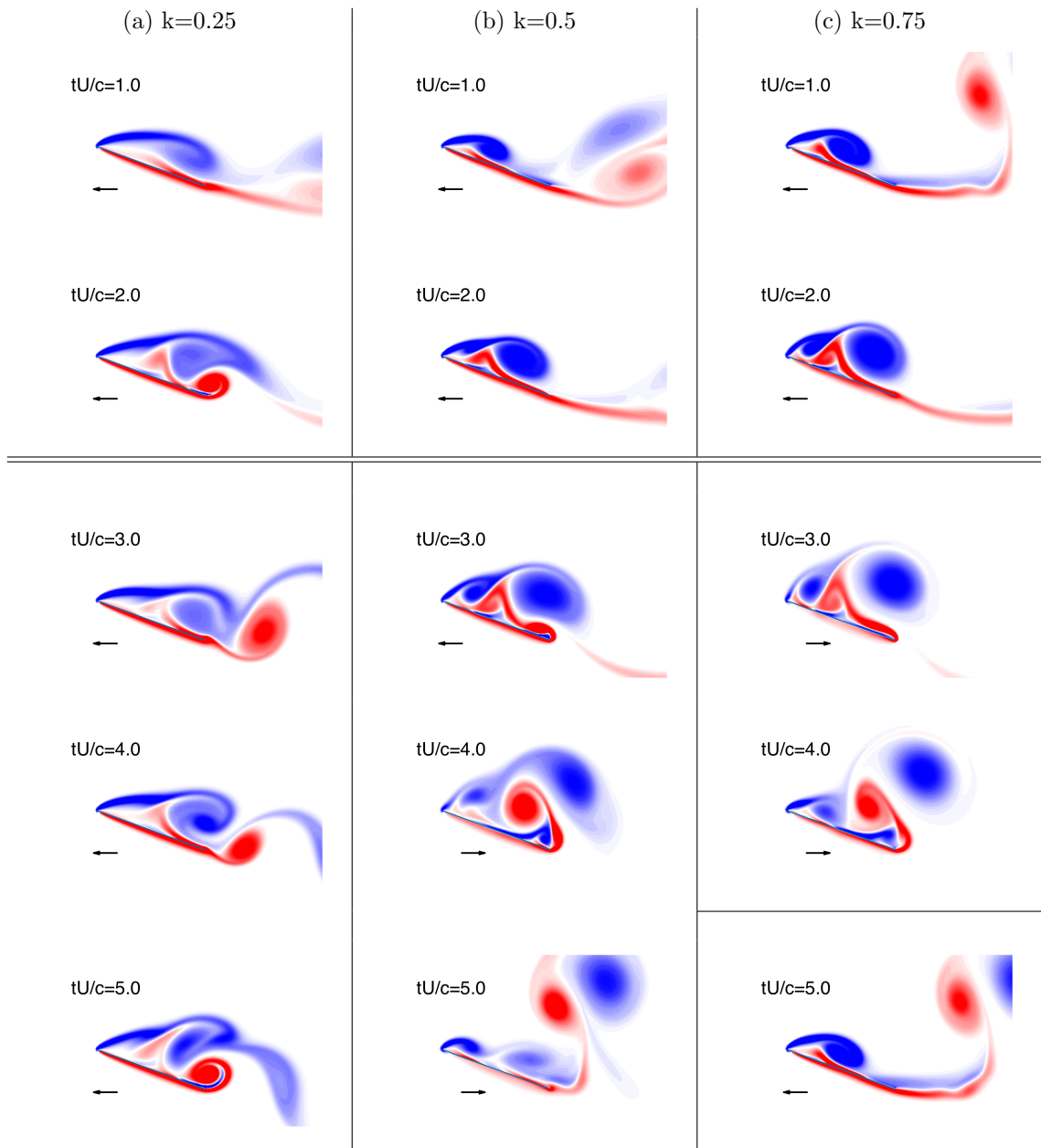


Figure 4.13: Flow fields shown as a series of increasing convective time,  $tU/c$ , for  $k = 0.25$ ,  $k = 0.5$ , and  $k = 0.75$ . Time is measured from the start of the advancing motion. Left and right pointed arrows indicate the advancing and retreating portion of the period, respectively. Double horizontal line is associated with the LEV formation time, which occurs at  $3 < T^* < 4$ . Single horizontal line indicates the end of one period of the motion.  $\alpha = 20^\circ$ ,  $Re = 1000$ , and  $\sigma_x = 0.4$ .

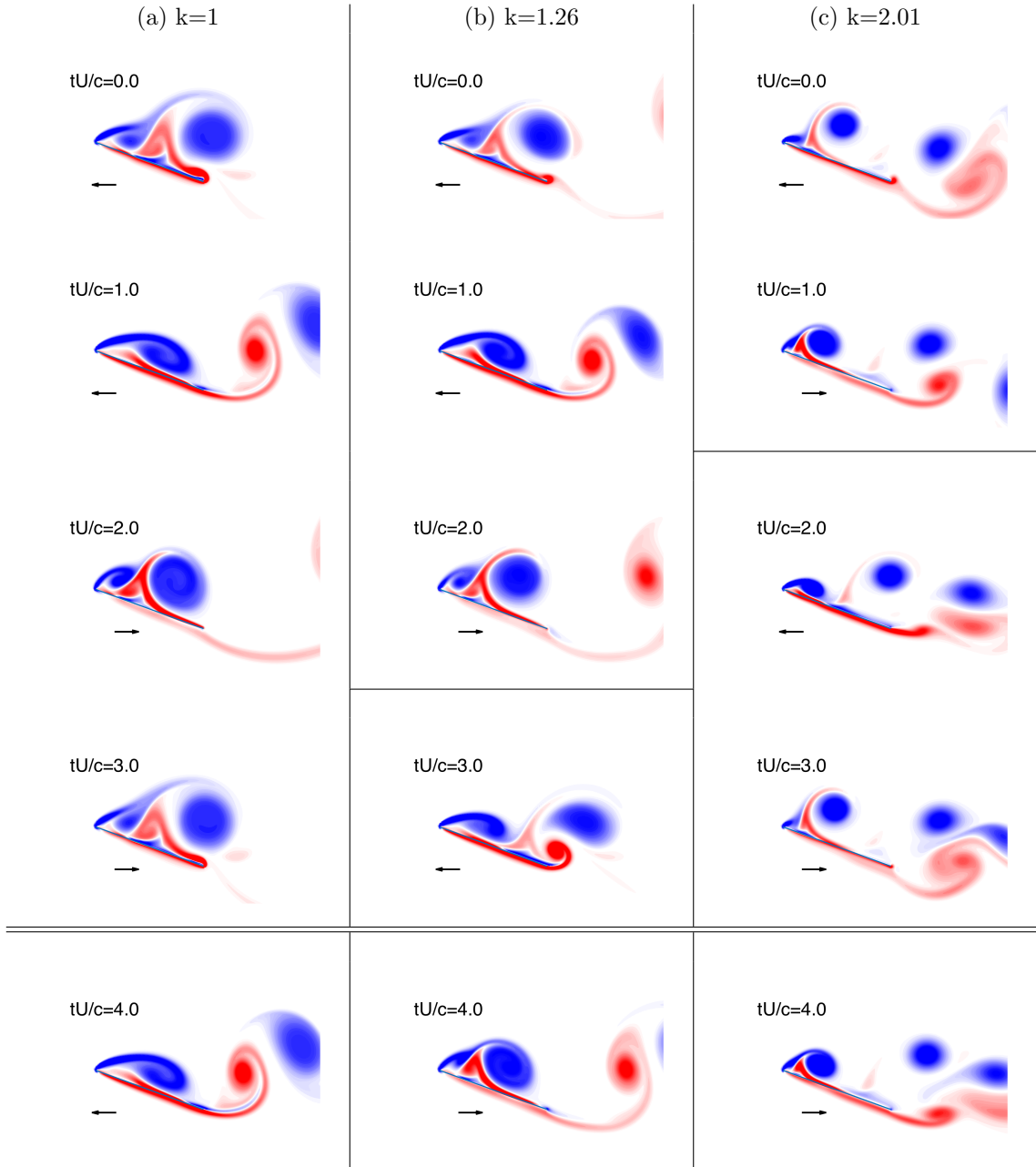


Figure 4.14: Same as figure 4.13, but at  $k = 1, 1.25,$  and  $2.01$ .

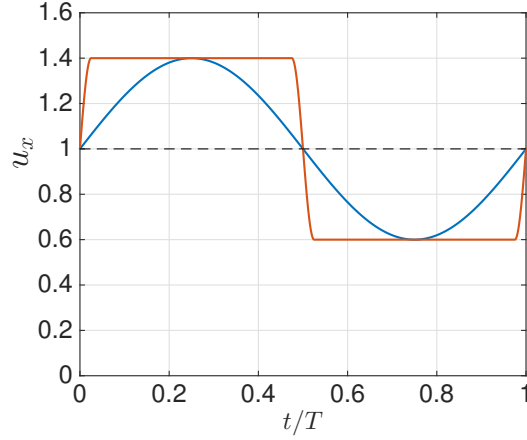


Figure 4.15: Sinusoidal and square waveform of streamwise velocity.  $\sigma_x = 0.4$ .

$$u(t) = \begin{cases} 1 + \sigma_x \cos\left(2\pi f_p t - \frac{\pi}{2}\right) & \text{if } 0 < t \leq \frac{\tau}{4} \\ 1 + \sigma_x & \text{if } \frac{\tau}{4} < t \leq \frac{T}{2} - \frac{\tau}{4} \\ 1 + \sigma_x \cos\left(2\pi f_p \left(t - \frac{T}{2} + \frac{\tau}{4}\right)\right) & \text{if } \frac{T}{2} - \frac{\tau}{4} < t \leq \frac{T}{2} + \frac{\tau}{4} \\ 1 - \sigma_x & \text{if } \frac{T}{2} + \frac{\tau}{4} < t \leq T - \frac{\tau}{4} \\ 1 + \sigma_x \cos\left(2\pi f_p \left(t - T + \frac{\tau}{4}\right) + \frac{\pi}{2}\right) & \text{if } T - \frac{\tau}{4} < t \leq T, \end{cases}$$

where  $f_p$  is the frequency associated with the cosine function used to represent the pulse.  $\tau$  is the period of the pulse ( $= 1/f_p$ ), and the reduced frequency of this pulse is set to be  $k_p = 12.6$ .

Figure 4.16 plots the time-averaged lift coefficients using the square wave as the streamwise velocity. Comparing the results with the sinusoidal case of  $\sigma_x = 0.4$ , there are two noticeable changes in the behavior of the mean lift. The mean lift at low reduced frequencies has substantially increased, while at the peak it has decreased.

The time history of lift of the square wave motion is shown in figure 4.17 over  $0.13 < k < 1.51$ . Only the advancing portion of the period,  $0 < t/T < 0.5$ , is shown to clearly display the results that collapse on the same curve. Acceleration is high enough at the start of the advancing period, and nearly identical flow structures emerge around the airfoil regardless of the reduced frequency. In figure 4.18 and figure 4.19 snapshots of flow fields over  $0.25 \leq k \leq 1.51$  are shown as a series of

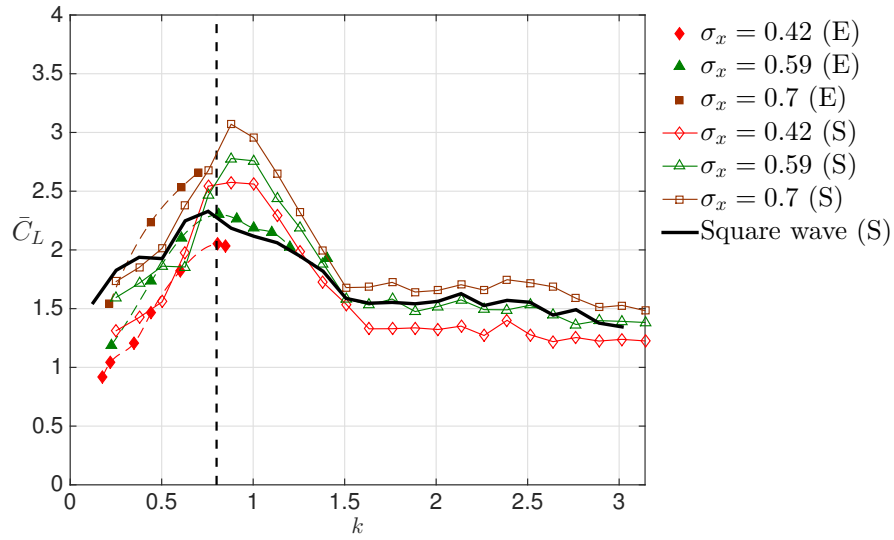


Figure 4.16: Time-averaged lift coefficient,  $\bar{C}_L$ . Black solid line shows the result obtained using the square waveform streamwise velocity.

increasing convective time units, similar to the figure 4.13. The LEV that develops from the early roll-up of a leading-edge shear layer is evident. As all frequencies benefit from LEV lift enhancement at every period, the mean lift resulting from a square wave velocity is higher than the sinusoidal case at low reduce frequencies.

During the retreating portion of the period, the wake capturing phenomenon allowed a further increase in lift over  $0.75 < k < 1$  for the sinusoidal waveforms. Examining the corresponding flow fields of the square wave velocity motion at  $k = 0.75$  and  $k = 1$  in figure 4.19, the abrupt deceleration generates opposite sign vortices on the upper surface of the airfoil. These vortices accumulate near the leading edge and form a dipole with the shed LEV. The self-induced velocity of the dipole moves the vortex pair away from the body, and there is no LEV lift enhancement during the retreating phase. As the incremental lift of LEV is limited only to the advancing period, the mean lift is significantly reduced compared to the sinusoidal motions at  $0.75 < k < 1$ .

The formation time measured for the sinusoidal case was  $T^* \approx 3.14$ , and from equation 4.2, the LEV that starts to form at the beginning of the advancing period is expected to grow until  $t^* = 2.24$  convective time units, which match well with the maximum lift in figure 4.17. The frequency of the motion associated with this time is  $k^* = 0.7$ , and the mean lift peak of the square waveform occurs

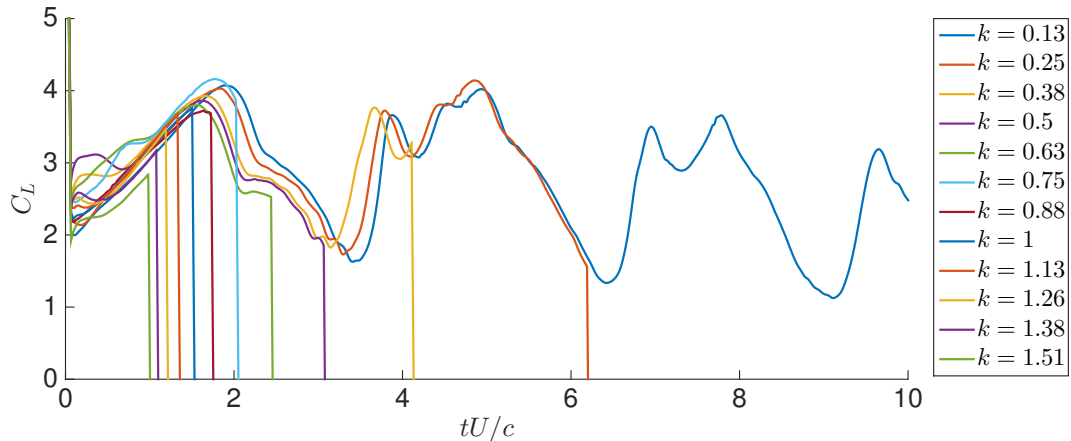


Figure 4.17: Time history of lift coefficient at various reduced frequencies. Only the advancing portion of the period,  $0 < t/T < 0.5$ , is shown.

near this value (figure 4.16). We believe the same mechanism is occurring for the square wave as for the sinusoidal surging. The time-averaged lift increases as a function of  $k$  for  $k < k^*$  as the time scale associated with LEV formation possesses a larger portion of the period, and decreases for  $k > k^*$  as the strength of LEV diminish with increasing reduced frequency.

## 4.6 Summary

The time-averaged forces and LEV strength of a two-dimensional flat plate with high-amplitude streamwise oscillations were investigated to understand the vortical structures that lead to the peak in the mean lift. Comparison with the experiment (Gursul & Ho, 1992) showed good agreement, where the peak occurred at a reduced frequency near  $k = 0.8$ , regardless of the velocity amplitude. The peak seemed to be unrelated to the natural wake instability, but rather closely related to the competing time scales of the airfoils motion and the LEV inherent formation time. From circulation analysis, the formation time of LEV was determined to be  $T^* \approx 3.14$ , where the associated  $k$  value was close to 1. The mean lift peak occurred when the period of the motion was close to the formation time, as the airfoil continuously formed a LEV during the whole period. Above  $k = 1$ , as the period of the motion becomes shorter than the formation time, the strength of the LEV diminished as the motion of the airfoil forced the LEV to shed before it has reached its maximum strength.

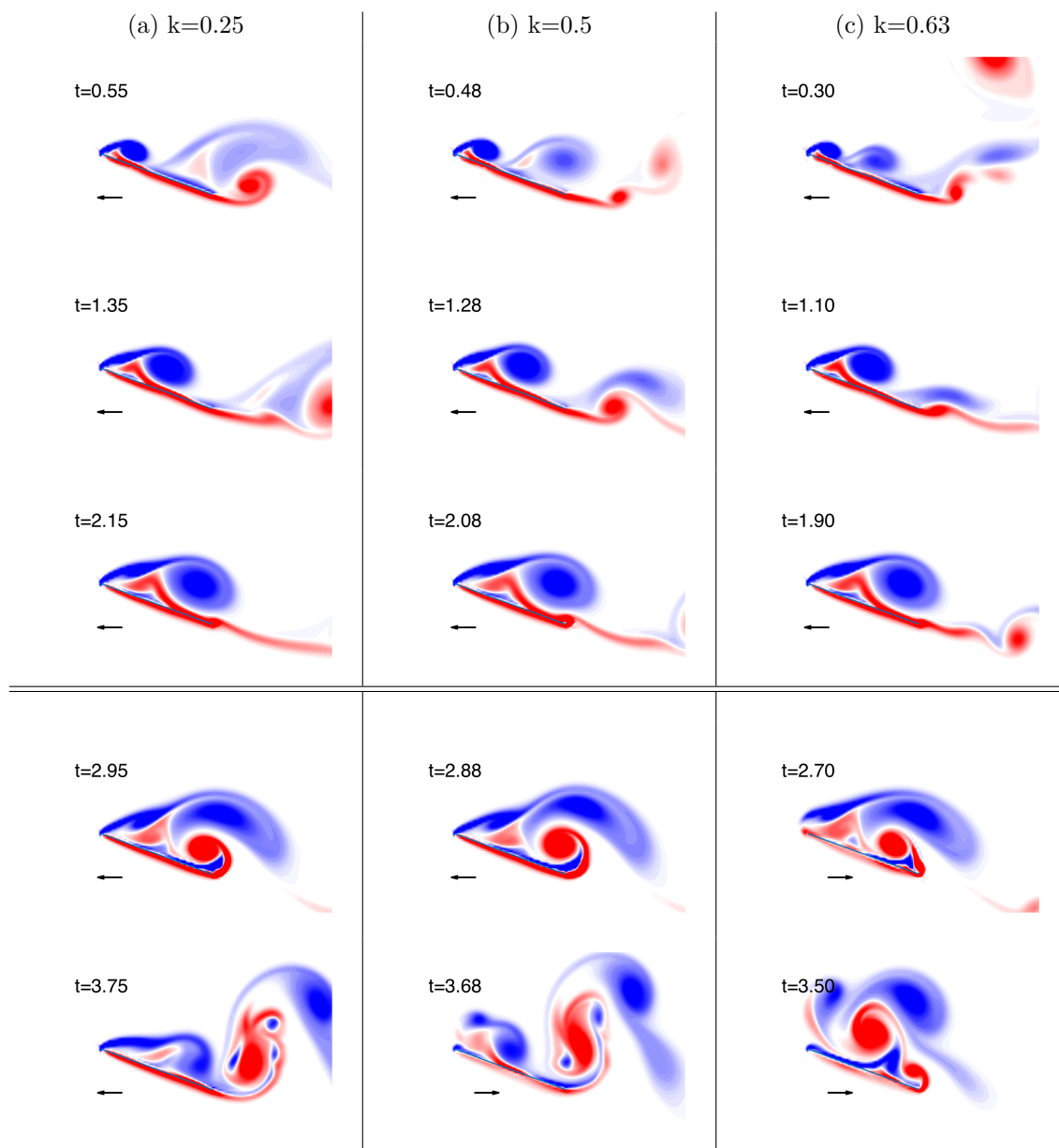


Figure 4.18: Same as figure 4.19, but with square waveform of streamwise velocity. Results are shown at  $k = 0.25, 0.5,$  and  $0.63$ .

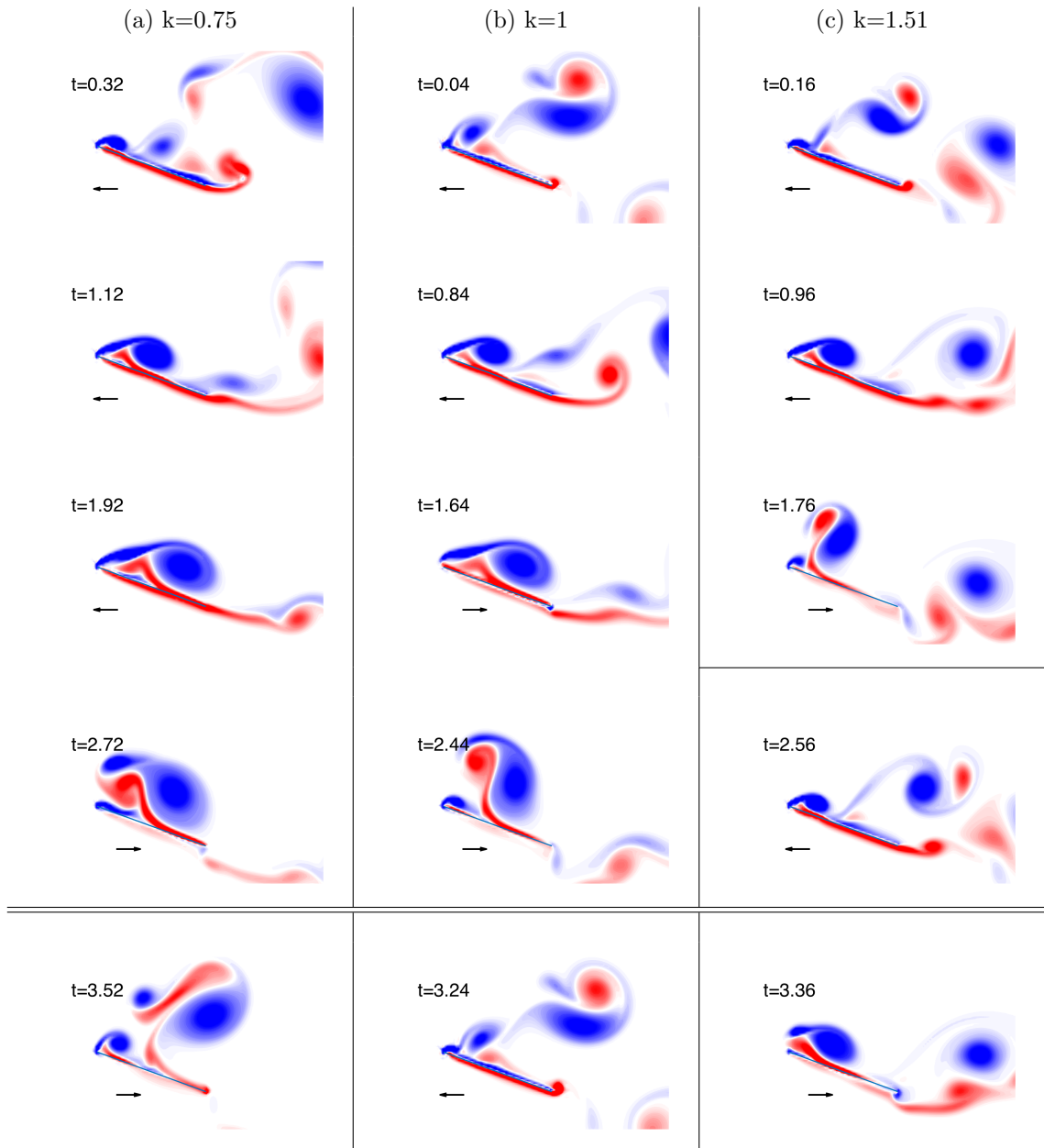


Figure 4.19: Same as figure 4.19, but with square waveform of streamwise velocity. Results are shown at  $k = 0.75, 1, \text{ and } 1.51$ .

Results using square waveform as the streamwise velocity showed that when acceleration is high enough, a LEV is formed even for the low frequency motions, enhancing the mean lift. At the peak frequency, however, the wake capturing phenomenon was no longer apparent and the time-averaged lift was substantially decreased. A dipole was formed during the retreating portion of the period and moved the LEV away from the body.

## Chapter 5

# Optimal Control of an Airfoil

In this chapter, unsteady flow control problems are formulated based on the mathematical framework of chapter 2. Our objective is to maximize the amount of lift on a constantly moving airfoil and also the vertical force on a reciprocating airfoil by controlling the pitch rate of the airfoil. A detailed study of the flow structure associated with the optimized motion is investigated and summarized to understand the mechanism that enhances the aerodynamic forces.

### 5.1 Test problem

For our test problem, we apply adjoint-based optimal control to determine how the (flat plate) airfoil should pitch to maximize lift. The plate is moving at a constant velocity,  $U$ , and the Reynolds number ( $Re = Uc/\nu$ ) is set to 500. If the flow were always steady, the optimization should pitch the plate up to a fixed angle of attack corresponding to the maximum lift (about 45 degrees for this airfoil and Reynolds number). For unsteady flow, it is unclear a priori what the optimal strategy is. Grid resolution (100 grid points per chord) is slightly higher than the ones used in chapter 3, with each of the 5 multiple grid levels having  $200 \times 200$  number of grid points. The domain extends to 32 by 32 chord lengths in the x and y direction. A schematic of the problem is shown in figure 5.1. At high angles of attack, the center of pressure on a symmetric airfoil is known to move towards the rear, and we set the rotational axis 0.3 chord length away from the leading-edge, rather than at the quarter chord. The control is applied after the transient part of the time history is removed.

Before applying control, the static map of the lift and drag coefficients are evaluated at various

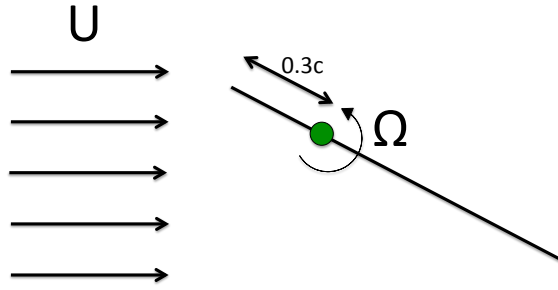


Figure 5.1: Schematic of the test problem. Flat plate moving at a constant velocity,  $U$ , with the rotational axis located 0.3 chord length from the leading-edge.  $\Omega$  is the angular velocity of the body.

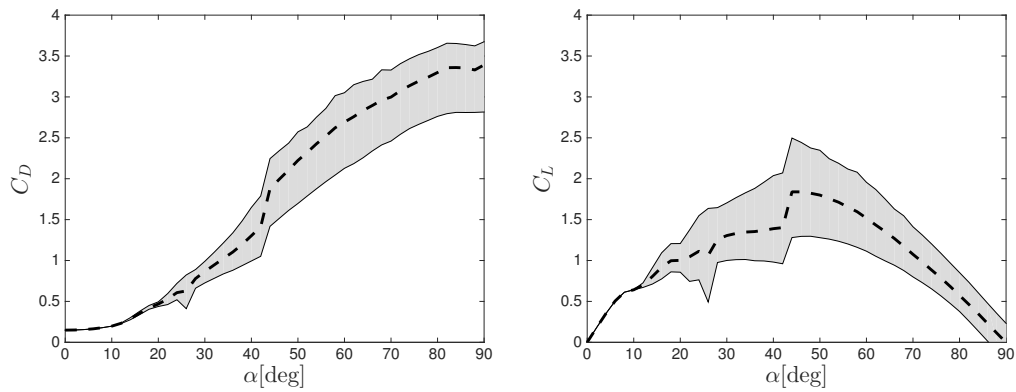


Figure 5.2: Drag and lift coefficient of uniform flow at various angles of attack. Shaded region shows the range of values, and the dash line, the average. Flat plate,  $Re = 500$ . Aerodynamic forces measured at every  $2^\circ$ . Transition from a stable equilibrium to periodic vortex shedding occurs at  $10^\circ$ .

angles of attack (in figure 5.2) to understand the general behavior of the aerodynamic forces. As expected, drag coefficient monotonically increases with increasing angle of attack. At an angle near  $10^\circ$ , the flow undergoes a Hopf bifurcation (refer to the bifurcation diagram of figure 3.2), and the presence of the wake instability becomes more significant as the angles of the inclined plate increase. For the lift coefficient, the maximum time-averaged lift occurs at an angle of  $45^\circ$ . From these observations of static aerodynamic forces, we run several optimization cases at different angles of airfoils and examine whether the optimal solution converges near to the angle of  $45^\circ$  that produces the highest lift.

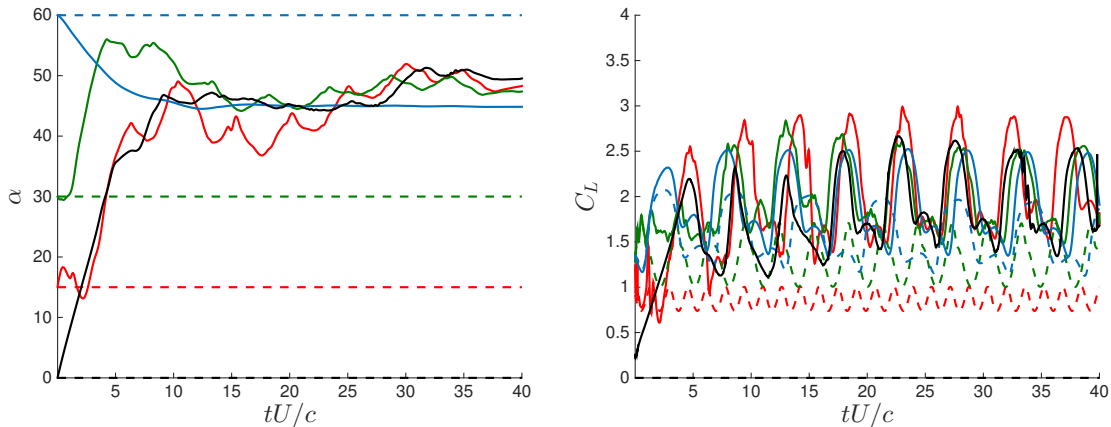


Figure 5.3: Optimization results of a flat plate at  $\alpha = 0^\circ$  (black),  $15^\circ$  (red),  $30^\circ$  (green), and  $60^\circ$  (blue). Angle of attack (left) and lift coefficient (right) is plotted as a function of time. Dashed line indicates the case before control and solid line, after. Optimization leads the airfoil to rotate towards the angle that maximizes lift, which is near  $45^\circ$ . Control time horizon,  $T$ , is 40 convective time units.

The cost function we use is defined as,

$$\mathcal{J}_F = \frac{1}{2} \int_0^T [(F_L - F_{L,\text{ref}})^2 + Q_R \Omega^2] dt. \quad (5.1)$$

$F_L$  is the integrated IB forces in the y direction (lift), and  $F_{L,\text{ref}}$ , the reference lift.  $\Omega$  is the angular velocity, which is used as the control variable. It is penalized in the cost function with the coefficient,  $Q_R$ , to avoid rapid rotations that require a large amount of energy and to avoid unrealistic control solutions such as constant rotations. The performance of each optimization result is quantified by the amount of lift enhancement by setting  $F_{L,\text{ref}}$  to a sufficiently high value.

Figure 5.3 shows time series of the angles and lift coefficients for representative cases at initial angles of  $\alpha = 0^\circ, 15^\circ, 30^\circ$ , and  $60^\circ$ . The cases before the optimization are the ones at constant  $\alpha$ , with zero angular velocity. Applying adjoint-based control, the optimal waveform of the angular velocity,  $\Omega(t)$ , is computed and the corresponding angles are shown in figure 5.3. Consistent with the result shown in figure 5.2, the angle of the airfoil rotates toward a value near  $45^\circ$ . Resulting lift coefficients before and after the optimization are also plotted, where the enhancement of lift is evident.

In table 5.1, we summarize the results (including the ones in figure 5.3) of the case at  $\alpha =$

Table 5.1: Summary of optimization results.  $\bar{C}_L$  is the time-averaged lift coefficient after control, and  $\bar{C}_{L0}$  before. The integrated control cost is defined as  $\int_0^T Q_R \Omega^2 dt$ , and reference lift coefficient normalized as  $C_{L,\text{ref}} = 2F_{L,\text{ref}}/\rho U^2 c$ . T is the control horizon.

$\alpha$	$C_{L,\text{ref}}$	$Q_R$	$\bar{C}_L$	$\bar{C}_L/\bar{C}_{L0}$	Control cost	T
0°	20	10	1.915	-	1.013	40
15°	20	1	1.971	2.289	0.166	40
20°	20	1	2.159	2.151	0.134	40
30°	20	1	1.986	1.509	0.093	40
45°	20	1	1.903	1.006	0.001	40
60°	20	1	1.905	1.215	0.009	40
90°	20	1	1.807	-	4.006	40

0°, 15°, 30°, 45°, 60°, and 90°. For the particular set of parameters in table 5.1, the 20° case reached the highest mean  $C_L$ , and since the 45° case is already at the optimal angle, only a small increment of lift was obtained with negligible control cost. For obvious reasons, the control cost tended to increase when the initial angle of the plate was further from the optimal angle.

Although the results obtained in table 5.1 were for specific values of  $Q_R$ , we believe that for sufficiently large  $Q_R$ , the converged solutions would not differ much from the results above. We also note that the control horizon, T, used in our computations is long enough to capture the important time scales in the flow, e.g., vortex shedding. Only marginal improvements are expected beyond a certain control horizon (Bewley *et al.*, 2001; Protas & Styczek, 2002; Flinois & Colonius, 2015), and for all of our cases, we chose a control horizon that is sufficiently long such that the results were not sensitive.

## 5.2 Flapping flight

Over the past decades, extensive computational and experimental studies of flapping flight have been conducted to reveal the important parameters and mechanisms that control lift, thrust, and propulsive efficiency. For insects and small birds that operate at low Reynolds number ( $Re = O(10^2 - 10^3)$ ) and high angles of attack ( $> 30^\circ$ ), the flow around the wing is vulnerable to flow separation. The unsteady motion of flapping produces much higher lift than the corresponding

steady case (Ellington *et al.*, 1996), and the presence of a leading-edge vortex was found to enhance lift by generating low pressure regions on the suction side of the wing (Dickinson & Gotz, 1993; Ellington *et al.*, 1996). The flapping motion of an insect’s wing, in general, consists of a translational and a rotational motion (pronation and supination), and during rotation, insects are known to use less energy to pitch their wings by capturing the wake generated during the previous stroke cycle (Dickinson *et al.*, 1999; Bergou *et al.*, 2007; Pesavento & Wang, 2009).

In the present study, we investigate the aerodynamic forces and flow structure associated with flapping, and apply optimal control. The adjoint approach is implemented to maximize the force in the vertical direction,  $F_y$ , by finding the optimal pitch angles during flapping. The cost function,  $\mathcal{J}$  is defined as,

$$\mathcal{J}_F = \frac{1}{2} \int_0^T (F_Y - F_{Y,\text{ref}})^2 dt, \quad (5.2)$$

where  $F_{Y,\text{ref}}$  is set to a high value.

The majority of wing motions of insects employ a superposition of heaving and pitching motion (sometimes referred as a “figure-eight” motion), which can be simplified as,

$$x = \frac{A_0}{2} \cos(2\pi ft) \cos(\beta) \quad (5.3)$$

$$y = \frac{A_0}{2} \cos(2\pi ft) \sin(\beta) \quad (5.4)$$

$$\alpha = \frac{\pi}{4} (1 - \sin(2\pi ft)), \quad (5.5)$$

where the schematic of the motion is plotted in figure 5.4 (Wang, 2000). Among various choices of waveforms that describe the flapping motion of a wing, sinusoidal motions are one of the simplest and realistic representation of a flying insect (Azuma *et al.*, 1985).

In our studies, the stroke amplitude,  $A_0$ , is set to be 2.5 times the chord length and the Reynolds number,  $Re(= Uc/\nu)$ , is set to be 100. The reference velocity,  $U$ , is equal to the maximum velocity ( $= A_0\pi f$ ). Assuming a wing of 1 mm chord length in air ( $\nu = 1.8 \times 10^{-5}$  m<sup>2</sup>/s), the frequency

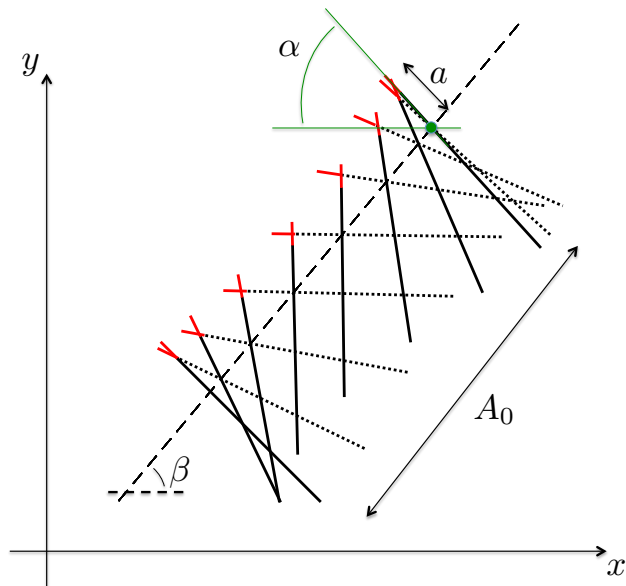


Figure 5.4: Flapping motion of a wing element in 2D. Downstroke phase indicated by the dotted line and upstroke by the solid line. The stroke plane is inclined at an angle  $\beta$ , with an amplitude of  $A_0$ .  $a$  is the distance of the rotating axis from the leading edge, and  $\alpha$ , the pitch angle.

is close to 230 Hz, similar to the beating frequency of a fruit fly (Fry *et al.*, 2005). We set the translational motion (equation 5.3 and equation 5.4) to be prescribed and consider the sinusoidal pitch angles (equation 5.5) as our initial control waveform for cases of  $\beta = 0^\circ, 30^\circ, 60^\circ$ , and  $90^\circ$ .

Table 5.2 summarizes the results of the optimizations. Minimizing the cost function of equation 5.2, optimization results in increasing the net vertical force, with the trade-off of increased input power. However, the effect is beneficial to the efficiency of enhancing  $F_y$ , as the increment of  $F_y$  is significant compared to the increase of required power,  $P$ . The maximum  $F_y$  occurs at  $\beta = 0^\circ$  and  $\beta = 60^\circ$ , and  $\beta = 0^\circ$  requires less power than  $\beta = 60^\circ$ . Figure 5.5 plots the trajectories of the wings before and after optimization.

For  $\beta = 0^\circ$ , the motion of the wing becomes more symmetric for each stroke. Figure 5.6 plots the vorticity field of the optimized wing motion at  $\beta = 0^\circ$ . The airfoil adjusts its angles during the stroke to grow a large LEV, which remains close to the airfoil until it changes the direction. The angle of attack at the middle of the stroke is between  $40^\circ$  and  $60^\circ$ , which according to figure 5.2 is within the regime of maximum static lift. At the time the airfoil changes its direction, the LEV

Table 5.2: Summary of optimization results.  $A_0 = 2.5c$ ,  $a = 0.3c$ , and  $Re = 100$  for all cases. Time-averaged normalized forces,  $\bar{C}_x = 2F_x/(\rho U^2 c)$ , and  $\bar{C}_y = 2F_y/(\rho U^2 c)$ , in the x and y direction are given, respectively. Time-averaged power is also presented in the table, where  $\bar{P}$  includes both the rotational and translational power. The subscript with 0 indicates the values for cases before optimization. Control horizon,  $T$ , is set to 40 convective time units, which is close to 5 flapping period.

$\beta$	$\bar{C}_{0,x}$	$\bar{C}_x$	$\bar{C}_{0,y}$	$\bar{C}_y$	$\bar{P}_0$	$\bar{P}$
$0^\circ$	-0.463	0.019	-0.008	0.850	-0.784	-1.015
$30^\circ$	-0.723	-0.021	0.361	0.764	-0.932	-0.935
$60^\circ$	-0.354	-0.049	0.714	0.849	-0.924	-1.036
$90^\circ$	0.009	0.211	0.465	0.490	-0.786	-0.798

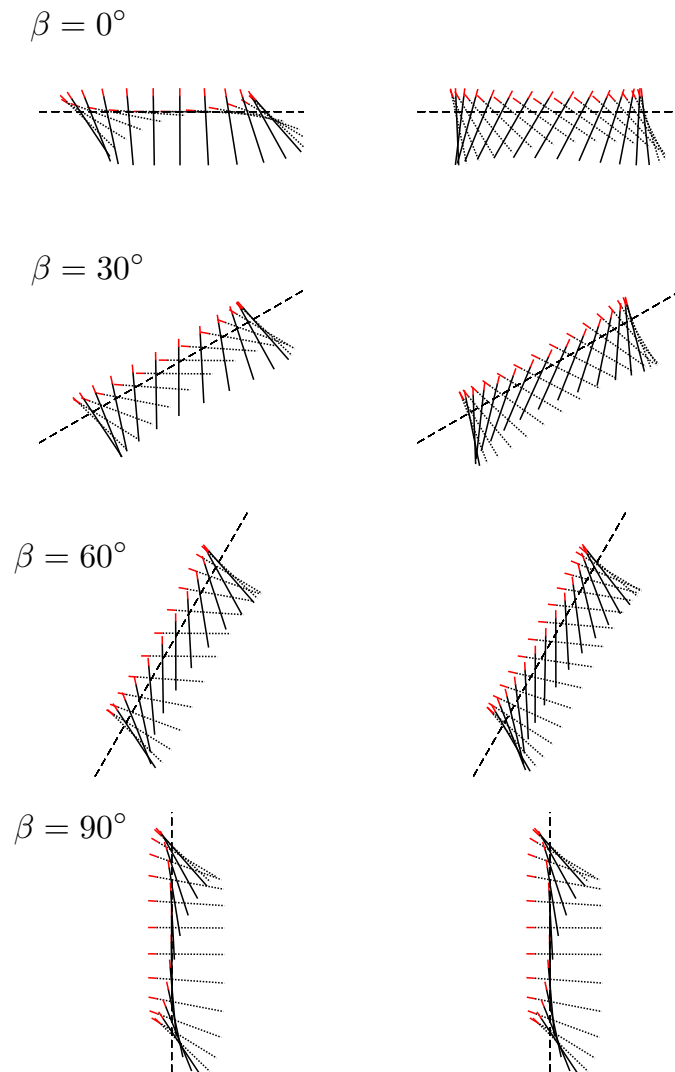


Figure 5.5: Flapping motions before (left) and after (right) optimization.

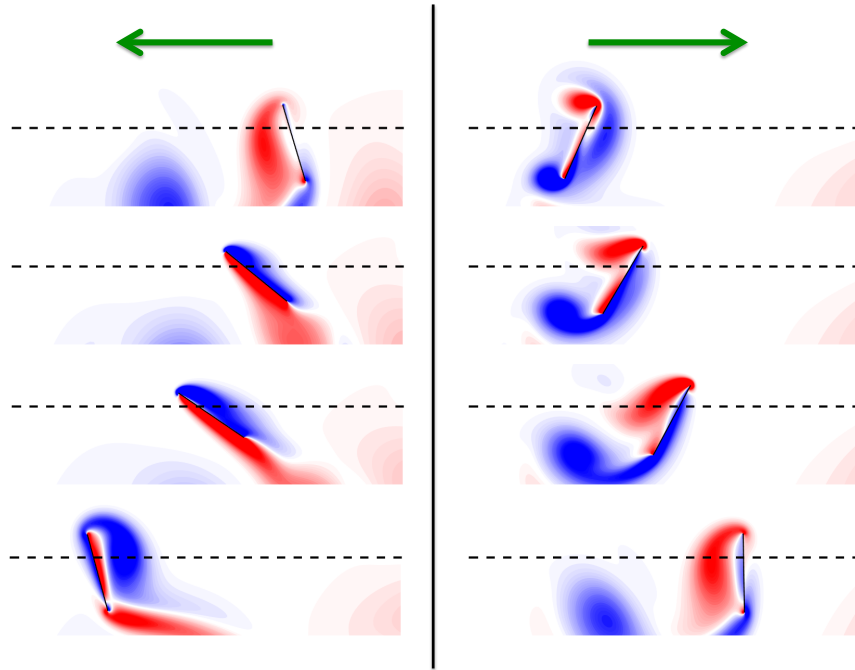


Figure 5.6: Vorticity field of the optimized wing motion at  $\beta = 0^\circ$ .

is shed, and the airfoil grows a new vortex of opposite sign. During stroke reversal, the shed LEV still remains above the airfoil providing beneficial effects, such as reducing the required power of the motion (Dickinson *et al.*, 1999).

To understand the effect of LEV on the aerodynamic forces, time history of the vertical force is plotted in figure 5.7. The figure shows the normalized y-force,  $C_Y(t)$ , for one flapping period, with the first half corresponding to the motion moving from right to left, and the second half, vice versa. The peak force occurs at a time close to the moment when the airfoil moved half of the stroke line.

The power required for the flapping airfoil is also shown in figure 5.8. Power can be decomposed into translational and rotational power, which originates from the heaving and pitching motion, respectively.  $P_{trans}$  and  $P_{rot}$  are defined as follows,

$$P_{trans}(t) = \frac{u_x(t)}{U} \cdot \frac{2\bar{F}_x(t)}{\rho U^2 c} + \frac{u_y(t)}{U} \cdot \frac{2\bar{F}_y(t)}{\rho U^2 c} \quad (5.6)$$

$$P_{rot}(t) = \frac{\Omega(t)c}{U} \cdot \frac{2\tau}{\rho U^2 c^2}, \quad (5.7)$$

where  $u_x$  and  $u_y$  are the translational velocities of the airfoil, and  $\tau$  is the torque measured at

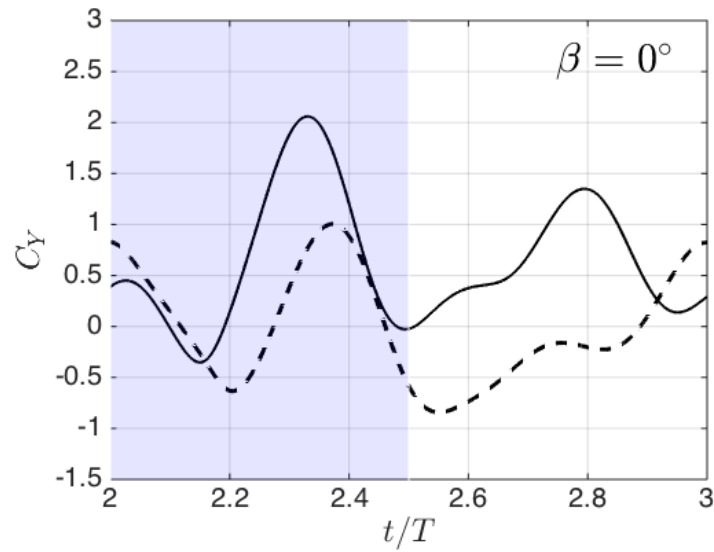


Figure 5.7: Time history of the vertical force coefficient,  $C_y$ , for the optimized result of  $\beta = 0^\circ$ . Dashed line indicates the data before optimization, and solid line, after. Shaded region indicates the stroke moving from right to left.

the rotation axis  $(x_c, y_c)$ ,

$$\tau = \int F_y(t) \cdot (x - x_c) - F_x(t) \cdot (y - y_c) ds.$$

Mostly, the power is negative, indicating that the body requires input of energy to follow the prescribed translational motion; however, at the stroke reversal, due to the suction region created by the previous shed LEV, the resultant force directs to the same direction as the velocity.  $P_{rot}$  is positive during stroke reversal, and the airfoil would be able to change its orientation without using much energy.

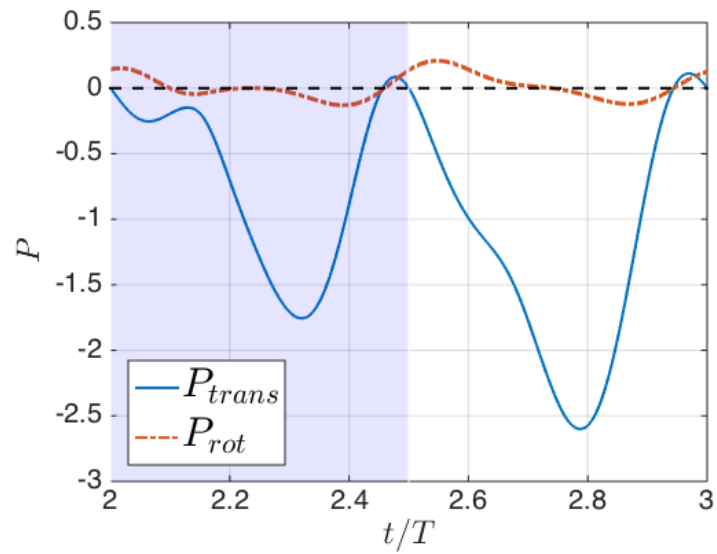


Figure 5.8: Time history of power,  $P$ , for the optimized result of  $\beta = 0^\circ$ . Shaded region indicates the stroke moving from right to left.

## Chapter 6

# Concluding Remarks

### 6.1 Summary and conclusions

In the present work, the flow structures and aerodynamic forces associated with simple harmonic oscillations of an airfoil were investigated. The characteristics of the mean and fluctuating forces were successfully explained by analyzing vortical flow features, and further extended to apply optimal control strategies to unsteady flows.

In chapter 3, the aerodynamic forces and flow structures associated with low-amplitude surging and plunging airfoils were investigated. Flows were limited to low Reynolds number, and high angles such that the flows were fully separated. For the surging motion, the wake instability locked-in to the harmonic frequency of the motion when the reduced frequencies were close to the shedding frequency or its subharmonic. These lock-in regions occurred within a continuous range of reduced frequencies and widened with increasing amplitude,  $\sigma_x$ , consistent with the phenomenon known as the Arnold's tongue. As resonance occurred, the time-averaged forces also increased in this regime.

Fluctuating behavior of lift was also investigated and found to be closely related to the formation and detachment of the leading-edge vortex. The frequency regime of  $k = 0.6$  and  $k = 1.2$ , where the fluctuations were amplified and attenuated, respectively, did not seem to be fundamentally related to the wake instability as it showed no significant dependence on the Reynolds number. Analysis of the flow structure revealed that fluctuating forces were amplified when the incremental force of LEV was added in-phase with the quasi component of velocity, and attenuated when out-of-phase.

At the amplification frequency, the LEV extended to its full strength at the maximum velocity, and separated before the start of the retreating period, whereas at the attenuation frequency, the LEV developed for a much longer portion of the period and separated during the retreating portion of the cycle. After this separation, it remained close to the airfoil and produced additional lift that canceled out the negative component of the quasi-static lift suppressing the fluctuations.

The aerodynamic forces that were associated with plunging motions were also shown to produce similar behavior to the surging case, where lock-in occurred near the vortex shedding frequency and its sub harmonic, and fluctuations amplified or attenuated depending on the phase of LEV acting constructively or destructively with the quasi-steady component of the forces. These frequency regimes coincided with surging.

For high-amplitude surging in chapter 4, the time-averaged lift of a flat plate at  $Re = 1000$  was compared to the experimental results of Gursul & Ho (1992) at  $Re = 50,000$  to understand the mechanism that led to the peak in the mean lift near the reduced frequency of  $k = 0.8$ . Circulation analysis led to an observation that there exists an inherent time scale of the LEV associated with its formation and detachment (LEV formation time), which does not change with the period of the motion. The formation time,  $T^*$ , was associated with a frequency of  $k = 1$ , and below this frequency there was a constant strength of maximum LEV formed during the period. The mean lift peak occurred when the period of the motion was close to the formation time as the portion of LEV lift enhancement increased during the period. For reduced frequency above  $k = 1$ , the LEV was forced to shed before it reached the formation time as the period of the motion became shorter than the formation time. The strength and size of LEV diminished as the total circulation decreased with increasing  $k$ , and as the strength of LEV diminished, the mean lift also decreased until the force associated with the LEV had no substantial contribution to  $\bar{C}_L$ .

Results were also compared with the square waveform of streamwise velocity. The square waveform velocity motion showed that high mean lift is achievable even for the low reduced frequencies as the abrupt change in velocity initiated the roll-up of a shear layer and formed a strong LEV regardless of the reduce frequency. However, at the peak, the dipole formed during the retreating

period moved the LEV away from the airfoil and there was no lift enhancement associated with the wake capturing phenomenon. The formation time obtained from the sinusoidal motion was applied to the square wave case, and the results matched well, showing a time-averaged peak near  $k = 0.7$ .

In chapter 5, adjoint-based optimal control was applied to an airfoil moving at a constant speed. The control objective was to maximize lift by controlling the pitch rate of the airfoil. The static map of lift showed maximum mean lift near the angle of  $45^\circ$ , and all of the optimized results converged to this angle.

The flapping motion of an insect's wing was also considered as a control problem to maximize the vertical force. The translational motion of the flapping wing was prescribed, and by controlling the pitch rate of the airfoil, optimization resulted in increasing the net vertical force, with the trade-off of increased input power required for the optimized flapping motion. For the motion that flaps horizontally ( $\beta = 0^\circ$ ), the optimized motion formed a large LEV, which remained close to the airfoil until the stroke reversal. The angles of the airfoil at the mid stroke was between  $40^\circ$  and  $60^\circ$ , which corresponded to the maximum static lift regime. During stroke reversal, the previous shed LEV still remained above the airfoil reducing the rotational power required for the motion.

## 6.2 Suggestions for future work

The focus of the present study has been on two-dimensional unsteady flows at low Reynolds number. Although the aerodynamic forces and flow fields of the two-dimensional simulations compared well with the high Reynolds number experiments, a firm conclusion must await future three-dimensional simulations at higher Reynolds number. The wake structure of a two-dimensional flow and a three-dimensional flow is essentially different, and a two-dimensional simulation at a higher Reynolds number would not represent the real three-dimensional wake structures as the three-dimensional instabilities develop.

Flow features that emerge in translational oscillating motions have been described in detail, and investigating the effects of the pitch rate on the aerodynamic forces would be an interesting problem to explore. At low reduced frequencies where quasi-steady assumptions are valid, plunging motions

may be considered as pitching as the effective angle changes during their motion; however, at higher pitch rates, the spatial variations of the velocity that occur due to rotation will display different flow structures compared to the translational motions.

Finally, the adjoint equations and gradients were derived for a rigid body that does not deform relative to the grid. Developing a framework to control flexible bodies would be a feature that broadens its application to a more general case, including numerous fluid-structure interaction problems.

## Appendix A

# Flow fields of rigid body motion in non-inertial frame of reference

For moving *rigid* bodies, the external flow around the body is more conveniently and efficiently solved in the non-inertial frame of the body. Usually the origin of the body-fixed frame being fixed at the center of mass, the arbitrary motion of the frame composes of a non-uniform translational,  $\mathbf{U}(t)$ , and rotational velocity,  $\mathbf{\Omega}(t)$ . Figure A.1 depicts the position vectors respect to the fixed and the moving frame of reference. Subscript  $f$  and  $r$  denotes the variables expressed in the fixed and rotational frame of reference, respectively.

The position, velocity, and accelerations vectors expressed in each of the reference frames are

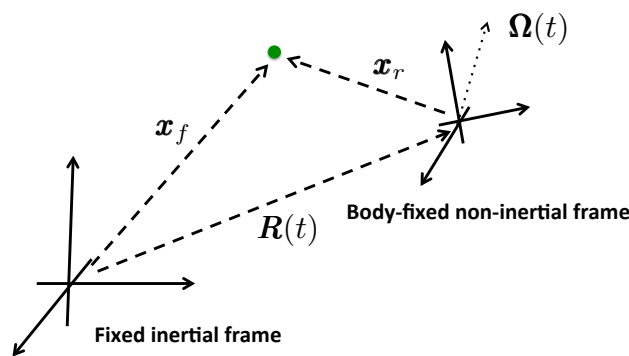


Figure A.1: Coordinate systems of fixed (inertial) and (non-inertial) rotating frame or reference.

related as,

$$\mathbf{x}_f = \mathbf{R}(t) + \mathbf{x}_r \quad (\text{A.1})$$

$$\mathbf{u}_f = \dot{\mathbf{R}}(t) + \mathbf{u}_r + \boldsymbol{\Omega}(t) \times \mathbf{x}_r \quad (\text{A.2})$$

$$\mathbf{a}_f = \ddot{\mathbf{R}}(t) + \mathbf{a}_r + 2 \boldsymbol{\Omega}(t) \times \mathbf{u}_r + \dot{\boldsymbol{\Omega}}(t) \times \mathbf{x}_r + \boldsymbol{\Omega}(t) \times \boldsymbol{\Omega}(t) \times \mathbf{x}_r. \quad (\text{A.3})$$

The Navier-Stokes equation in the non-inertial frame takes the form (Batchelor, 1967),

$$\frac{\partial \mathbf{u}_r}{\partial t} + \mathbf{u}_r \cdot \nabla \mathbf{u}_r = -\nabla p + \frac{1}{Re} \nabla^2 \mathbf{u}_r - \ddot{\mathbf{R}}(t) - 2 \boldsymbol{\Omega}(t) \times \mathbf{u}_r - \dot{\boldsymbol{\Omega}}(t) \times \mathbf{x}_r - \boldsymbol{\Omega}(t) \times \boldsymbol{\Omega}(t) \times \mathbf{x}_r, \quad (\text{A.4})$$

where the boundary conditions satisfy the following conditions:

$$\text{as } |\mathbf{x}_r| \rightarrow \infty \quad \left\{ \begin{array}{l} \mathbf{u}_r \rightarrow -\dot{\mathbf{R}}(t) - \boldsymbol{\Omega}(t) \times \mathbf{x}_r \\ \boldsymbol{\omega}_r \rightarrow -2 \boldsymbol{\Omega}(t) \\ p \rightarrow p_\infty. \end{array} \right.$$

If the body does not deform, i.e., rigid body, it additionally satisfies  $\mathbf{u}_r = 0$  on the surface of the body. Vorticity,  $\boldsymbol{\omega}_r$ , reaching the value of  $-2 \boldsymbol{\Omega}(t)$  at far field can be derived by taking curl of equation A.2,

$$\boldsymbol{\omega}_f = \boldsymbol{\omega}_r + 2 \boldsymbol{\Omega}(t). \quad (\text{A.5})$$

Although the velocity field and pressure can be computed using the non-inertial form of the Navier-Stokes equation (equation A.4) and the time-varying far field boundary conditions, there exists a more compact and convenient way of solving this problem. Substituting equation A.2 and

using vector identities,

$$\mathbf{u}_r \cdot \nabla \mathbf{u}_r = \nabla \left( \frac{1}{2} |\mathbf{u}_r|^2 \right) - \mathbf{u}_r \times \boldsymbol{\omega}_r = \nabla \left( \frac{1}{2} |\mathbf{u}_r|^2 \right) - \mathbf{u}_r \times \boldsymbol{\omega}_f - 2 \boldsymbol{\Omega} \times \mathbf{u}_r \quad (\text{A.6})$$

$$\nabla^2 \mathbf{u}_r = \nabla (\nabla \cdot \mathbf{u}_r) - \nabla \times (\nabla \times \mathbf{u}_r) = -\nabla \times \boldsymbol{\omega}_r = -\nabla \times \boldsymbol{\omega}_f \quad (\text{A.7})$$

$$\boldsymbol{\Omega} \times \boldsymbol{\Omega} \times \mathbf{x}_r = \nabla \left( \frac{1}{2} |\boldsymbol{\Omega} \times \mathbf{x}_r|^2 \right), \quad (\text{A.8})$$

equation A.4 is now written as,

$$\left( \frac{\partial \mathbf{u}_f}{\partial t} \right)_r = -\nabla \phi + (\mathbf{u}_f - \mathbf{u}_a) \times \boldsymbol{\omega}_f - \frac{1}{Re} \nabla \times \boldsymbol{\omega}_f, \quad (\text{A.9})$$

where

$$\mathbf{u}_a(\mathbf{x}_r, t) = \dot{\mathbf{R}}(t) + \boldsymbol{\Omega}(t) \times \mathbf{x}_r \quad (\text{A.10})$$

$$\phi = p + \frac{1}{2} |\mathbf{u}_f - \mathbf{u}_a|^2 - \frac{1}{2} |\mathbf{u}_a|^2. \quad (\text{A.11})$$

$\mathbf{u}_a$  is the translational and rotational velocity associated with the moving axes. The boundary conditions now satisfies,

$$\text{as } |\mathbf{x}_r| \longrightarrow \infty \quad \begin{cases} \mathbf{u}_f \longrightarrow 0 \\ \boldsymbol{\omega}_f \longrightarrow 0 \\ p \longrightarrow p_\infty, \end{cases}$$

and  $\mathbf{u}_f = \mathbf{u}_a$  on the surface of the body. Note that the variables,  $\mathbf{u}_f$  and  $\boldsymbol{\omega}_f$ , that are expressed in the inertial reference frame are computed (rather than  $\mathbf{u}_r$  and  $\boldsymbol{\omega}_r$ ). Also, the dependent variables vanish at the far field, alleviating the boundary condition treatments at infinity.

## Appendix B

# Checkpointing algorithm

In numerical simulation of a dynamical systems, adjoint equations are commonly used to obtain the gradient of a predefined objective function. For a general nonlinear dynamical system,

$$\dot{x} = h(x, t), \quad x(0) = x_0, \quad 0 \leq t \leq T, \quad (\text{B.1})$$

its adjoint equation is a linear dynamical system (in terms of the adjoint variables) that evolves backward in time,

$$\dot{q} = a(x, t)q + b(x, t), \quad q(T) = q_0(x(T)), \quad 0 \leq t \leq T. \quad (\text{B.2})$$

As the coefficients of the term  $a(x, t)$  and  $b(x, t)$  require information of  $x$ , the solution of the forward system must be either already stored in memory or recalculated from the solution at the last sorted time step. Since saving the forward solution at every time step is impractical and even impossible for most cases, the checkpointing scheme, which gives the optimal time steps to minimize the recalculations, is frequently used to solve the adjoint equation.

We implement the method developed by Wang *et al.* (2009), where figure B.1 demonstrates the algorithm. Assuming that the dynamical system has a total of 25 step to evolve from 0 to  $T$ , and the memory is limited to save only 5 time steps, the checkpoint algorithm provides the best / optimal time steps that should be saved to minimize the recalculations. For example, the index number of 8, 13, 18, 22, and 23 would be the time steps that are saved while solving the forward system.

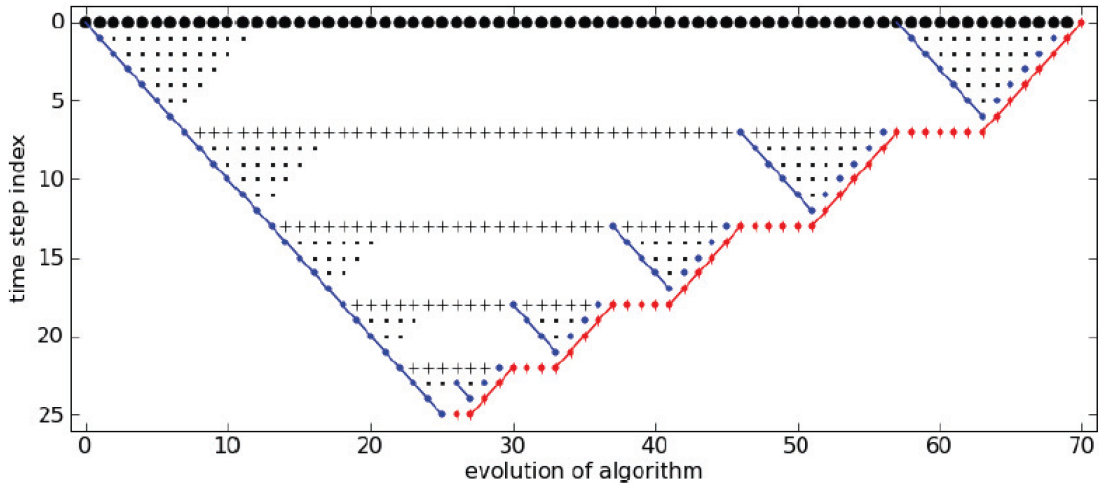


Figure B.1: Checkpointing algorithm developed by Wang *et al.* (2009). Evolution of the algorithm assuming a total of 25 time steps. 5 checkpoints are assigned to save the forward variables. Copyright ©2009 Society for Industrial and Applied Mathematics. Reprinted with permission.

Now, as it solves the adjoint system backwards in time, the forward variables would be loaded from memory if they exist, or else recalculated from one of saved solutions. For example, at the start of the adjoint equation, it requires the forward solution at time step index=24 (assuming that time marching scheme is implicit). Since the closest forward solution saved is at index=23, the forward solution at index=24 is obtained by computing the forward system from index=23 to 24. This can be generalized to any number of time step and saved checkpoints.

As the forward equation is recalculated while solving the adjoint equation, the computation time increases; however, the checkpointing scheme significantly reduces the memory requirement and efficiently solves the adjoint equation.

# Bibliography

- AHUJA, S. & ROWLEY, C. W. 2010 Feedback control of unstable steady states of flow past a flat plate using reduced-order estimators. *Journal of Fluid Mechanics* **645**, 447–478.
- ANDERSON, E. & SZEWCZYK, A. 1997 Effects of a splitter plate on the near wake of a circular cylinder in 2 and 3-dimensional flow configurations. *Experiments in Fluids* **23** (2), 161–174.
- ANDRO, J. Y. & JACQUIN, L. 2009 Frequency effects on the aerodynamic mechanisms of a heaving airfoil in a forward flight configuration. *Aerospace Science and Technology* **13** (1), 71–80.
- AZUMA, A., AZUMA, S., WATANABE, I. & FURUTA, T. 1985 Flight mechanics of a dragonfly. *Journal of experimental biology* **116** (1), 79–107.
- BAIK, Y. S., BERNAL, L. P., GRANLUND, K. & OL, M. 2012 Unsteady force generation and vortex dynamics of pitching and plunging aerofoils. *Journal of Fluid Mechanics* **709**, 37–68.
- BATCHELOR, G. 1967 *An introduction to fluid dynamics*. Cambridge Univ Press.
- BEARMAN, P. & HARVEY, J. 1993 Control of circular cylinder flow by the use of dimples. *AIAA Journal* **31** (10), 1753–1756.
- BEAUDOIN, J.-F. & AIDER, J.-L. 2008 Drag and lift reduction of a 3d bluff body using flaps. *Experiments in Fluids* **44** (4), 491–501.
- BECHERT, D., BRUSE, M. & HAGE, W. 2000 Experiments with three-dimensional riblets as an idealized model of shark skin. *Experiments in Fluids* **28** (5), 403–412.
- BERGOU, A. J., XU, S. & WANG, Z. J. 2007 Passive wing pitch reversal in insect flight. *Journal of Fluid Mechanics* **591**, 321–337.

- BEWLEY, T. R., MOIN, P. & TEMAM, R. 2001 DNS-based predictive control of turbulence: an optimal benchmark for feedback algorithms. *Journal of Fluid Mechanics* **447**, 179–225.
- BOYLAND, P. L. 1986 Bifurcations of circle maps: Arnol'd tongues, bistability and rotation intervals. *Communications in Mathematical Physics* **106** (3), 353–381.
- BROWN, C. & MICHAEL, W. 1954 Effect of leading edge separation on the lift of a delta wing. *J. Aero. Sci* **21** (10), 690–694.
- CALDERON, D. E., WANG, Z. & GURSUL, I. 2013 Lift-enhancing vortex flows generated by plunging rectangular wings with small amplitude. *AIAA Journal* **51** (12), 2953–2964.
- CHEN, K. K., COLONIUS, T. & TAIRA, K. 2010 The leading-edge vortex and quasisteady vortex shedding on an accelerating plate. *Physics of Fluids* **22** (3), 033601.
- CHOI, J., JEON, W.-P. & CHOI, H. 2006 Mechanism of drag reduction by dimples on a sphere. *Physics of Fluids* **18** (4), 041702.
- CLEAVER, D. J., WANG, Z. & GURSUL, I. 2012 Bifurcating flows of plunging aerofoils at high Strouhal numbers. *Journal of Fluid Mechanics* **708**, 349–376.
- CLEAVER, D. J., WANG, Z. & GURSUL, I. 2013 Investigation of high-lift mechanisms for a flat-plate airfoil undergoing small-amplitude plunging oscillations. *AIAA Journal* **51** (4), 968–980.
- CLEAVER, D. J., WANG, Z., GURSUL, I. & VISBAL, M. R. 2011 Lift enhancement by means of small-amplitude airfoil oscillations at low Reynolds numbers. *AIAA Journal* **49** (9), 2018–2033.
- COLONIUS, T. & TAIRA, K. 2008 A fast immersed boundary method using a nullspace approach and multi-domain far-field boundary conditions. *Computer Methods in Applied Mechanics and Engineering* **197** (25–28), 2131–2146.
- DABIRI, J. O. 2009 Optimal vortex formation as a unifying principle in biological propulsion. *Annual Review of Fluid Mechanics* **41**, 17–33.

- DABIRI, J. O. & GHARIB, M. 2005 Starting flow through nozzles with temporally variable exit diameter. *Journal of Fluid Mechanics* **538**, 111–136.
- DARAKANANDA, D., ELDREDGE, J., COLONIUS, T. & WILLIAMS, D. R. 2016 A vortex sheet/point vortex dynamical model for unsteady separated flows 2016–2072.
- DENNY, M. 2009 Dynamic soaring: aerodynamics for albatrosses. *European Journal of Physics* **30**, 75–84.
- DICKINSON, M. H. & GOTZ, K. G. 1993 Unsteady aerodynamic performance of model wings at low Reynolds numbers. *Journal of Experimental Biology* **174**, 45–64.
- DICKINSON, M. H., LEHMANN, F.-O. & SANE, S. P. 1999 Wing rotation and the aerodynamic basis of insect flight. *Science* **284** (5422), 1954–1960.
- DUNNE, R. & MCKEON, B. J. 2015 Dynamic stall on a pitching and surging airfoil. *Experiments in Fluids* **56** (8), 1–15.
- ELDREDGE, J. D., WANG, C. & OL, M. 2009 A computational study of a canonical pitch-up, pitch-down wing maneuver. *AIAA Paper* 2009–3687.
- ELLINGTON, C. P., VAN DEN BERG, C., WILLMOTT, A. P. & THOMAS, A. L. R. 1996 Leading-edge vortices in insect flight. *Nature* **384**, 626–630.
- FAGE, A. & JOHANSEN, F. C. 1927 On the flow of air behind an inclined flat plate of infinite span. *Proceedings of the Royal Society of London. Series A, Containing Papers of a Mathematical and Physical Character* **116** (773), 170–197.
- FLINOIS, T. L. & COLONIUS, T. 2015 Optimal control of circular cylinder wakes using long control horizons. *Physics of Fluids* **27** (8), 087105.
- FRY, S. N., SAYAMAN, R. & DICKINSON, M. H. 2005 The aerodynamics of hovering flight in drosophila. *Journal of Experimental Biology* **208** (12), 2303–2318.

- GHARIB, M., RAMBOD, E. & SHARIFF, K. 1998 A universal time scale for vortex ring formation. *Journal of Fluid Mechanics* **360**, 121–140.
- GILES, M. B., DUTA, M. C., M-UACUTE, J.-D., LLER & PIERCE, N. A. 2003 Algorithm developments for discrete adjoint methods. *AIAA Journal* **41** (2), 198–205.
- GRAFTIEAUX, L., MICHARD, M. & GROSJEAN, N. 2001 Combining PIV, POD and vortex identification algorithms for the study of unsteady turbulent swirling flows. *Measurement Science and Technology* **12** (9), 1422–1429.
- GRANLUND, K., MONNIER, B., OL, M. & WILLIAMS, D. 2014 Airfoil longitudinal gust response in separated vs. attached flows. *Physics of Fluids* **26** (2), 027103.
- GREENBERG, J. M. 1947 Airfoil in sinusoidal motion in a pulsating stream. *NACA Technical Report* (1326).
- GREENBLATT, D. & WYGNANSKI, I. J. 2000 The control of flow separation by periodic excitation. *Progress in Aerospace Sciences* **36** (7), 487–545.
- GRIEWANK, A. 1992 Achieving logarithmic growth of temporal and spatial complexity in reverse automatic differentiation. *Optimization Methods and Software* **1** (1), 35–54.
- GRIEWANK, A. & WALTHER, A. 2000 Algorithm 799: revolve: an implementation of checkpointing for the reverse or adjoint mode of computational differentiation. *ACM Transactions on Mathematical Software* **26** (1), 19–45.
- GURSUL, I. & HO, C. M. 1992 High aerodynamic loads on an airfoil submerged in an unsteady stream. *AIAA Journal* **30** (4), 1117–1119.
- GURSUL, I., LIN, H. & HO, C. M. 1994 Effects of time scales on lift of airfoils in an unsteady stream. *AIAA Journal* **32** (4), 797–801.
- HEMATI, M. S., ELDREDGE, J. D. & SPEYER, J. L. 2014 Improving vortex models via optimal control theory. *Journal of Fluids and Structures* **49**, 91–111.

- HUANG, R. F. & LIN, C. L. 1995 Vortex shedding and shear-layer instability of wing at low Reynolds numbers. *AIAA Journal* **33** (8), 1398–1403.
- JAMESON, A. 1988 Aerodynamic design via control theory. *Journal of Scientific Computing* **3** (3), 233–260.
- JOE, W. T., COLONIUS, T. & MACMYNOWSKI, D. G. 2010 Optimized waveforms for feedback control of vortex shedding. In *Active Flow Control II* 391–404. Springer.
- JONES, K. D., DOHRING, C. M. & PLATZER, M. F. 1996 Wake structures behind plunging airfoils: a comparison of numerical and experimental results. *AIAA Paper* 1996–78.
- KARNIADAKIS, G. E. & TRIANTAFYLLOU, G. S. 1989 Frequency selection and asymptotic states in laminar wakes. *Journal of Fluid Mechanics* **199**, 441–469.
- KERSTENS, W., PFEIFFER, J., WILLIAMS, D., KING, R. & COLONIUS, T. 2011 Closed-loop control of lift for longitudinal gust suppression at low Reynolds numbers. *AIAA Journal* **49** (8), 1721–1728.
- LANGELAAN, J. W. 2009 Gust energy extraction for mini and micro uninhabited aerial vehicles. *Journal of Guidance, Control, and Dynamics* **32** (2), 463–472.
- LEWIN, G. C. & HAJ-HARIRI, H. 2003 Modelling thrust generation of a two-dimensional heaving airfoil in a viscous flow. *Journal of Fluid Mechanics* **492**, 339–362.
- LIAN, Y. & OL, M. 2010 Computation and experiments on a low aspect ratio pitching flat plate. In *AIAA Paper* 2010–0385.
- LIECHTI, F., WITVLIET, W., WEBER, R. & BÄCHLER, E. 2013 First evidence of a 200-day non-stop flight in a bird. *Nature Communications* **4**.
- LISSAMAN, P. 1983 Low-Reynolds-number airfoils. *Annual Review of Fluid Mechanics* **15** (1), 223–239.
- LISSAMAN, P. 2005 Wind energy extraction by birds and flight vehicles. *AIAA Paper* 2005–241.

- LISSAMAN, P. B. S. & PATEL, C. K. 2007 Neutral energy cycles for a vehicle in sinusoidal and turbulent vertical gusts. *AIAA Paper* 2007–863.
- LUCHINI, P. & BOTTARO, A. 2014 Adjoint equations in stability analysis. *Annual Review of Fluid Mechanics* **46** (1), 493.
- MILANO, M. & GHARIB, M. 2005 Uncovering the physics of flapping flat plates with artificial evolution. *Journal of Fluid Mechanics* **534**, 403–409.
- MUNDAY, P. M. & TAIRA, K. 2013 On the lock-on of vortex shedding to oscillatory actuation around a circular cylinder. *Physics of Fluids* **25**, 013601.
- OL, M. V., ELDREDGE, J. D. & WANG, C. 2009 High-amplitude pitch of a flat plate: an abstraction of perching and flapping. *International Journal of Micro Air Vehicles* **1** (3), 203–216.
- PEROT, J. B. 1993 An analysis of the fractional step method. *Journal of Computational Physics* **108** (1), 51–58.
- PESAVENTO, U. & WANG, Z. J. 2009 Flapping wing flight can save aerodynamic power compared to steady flight. *Physical Review Letters* **103** (11), 118102.
- PESKIN, C. S. 1972 Flow patterns around heart valves: a numerical method. *Journal of Computational Physics* **10** (2), 252–271.
- PESKIN, C. S. 2002 The immersed boundary method. *Acta Numerica* **11**, 479–517.
- POLAK, E. 1970 *Computational methods in optimization. A unified approach*. Academic Press, CF Winter.
- POST, M. L. & CORKE, T. C. 2006 Separation control using plasma actuators: dynamic stall vortex control on oscillating airfoil. *AIAA Journal* **44** (12), 3125–3135.
- PROTAS, B. & STYCZEK, A. 2002 Optimal rotary control of the cylinder wake in the laminar regime. *Physics of Fluids* **14** (7), 2073–2087.

- PULLIAM, T. H. & VASTANO, J. A. 1990 Chaotic flow over an airfoil. In *Twelfth International Conference on Numerical Methods in Fluid Dynamics* 106–110. Springer.
- REUTHER, J. J., JAMESON, A., ALONSO, J. J., RIMLLINGER, M. J. & SAUNDERS, D. 1999 Constrained multipoint aerodynamic shape optimization using an adjoint formulation and parallel computers, part 2. *Journal of Aircraft* **36** (1), 61–74.
- RIVAL, D. E., KRIEGSEIS, J., SCHAUB, P., WIDMANN, A. & TROPEA, C. 2013 A criterion for vortex separation on unsteady aerodynamic profiles. *AIAA Paper* 2013–836.
- ROMA, A. M., PESKIN, C. S. & BERGER, M. J. 1999 An adaptive version of the immersed boundary method. *Journal of Computational Physics* **153** (2), 509–534.
- SCHMITT, N. P., REHM, W., PISTNER, T., ZELLER, P., DIEHL, H. & NAVÉ, P. 2007 The awiator airborne lidar turbulence sensor. *Aerospace Science and Technology* **11** (7), 546–552.
- SHEWCHUK, J. R. 1994 An introduction to the conjugate gradient method without the agonizing pain. Technical Report CMU-CS-94-125, Carnegie Mellon University. Department of Computer Science.
- SREENIVASAN, K. R., STRYKOWSKI, P. J. & OLINGER, D. J. 1987 Hopf bifurcation, Landau equation, and vortex shedding behind circular cylinders. In *Forum on Unsteady Flow Separation, ASME FED*, vol. 52 1–13.
- TAHA, H. E., HAJJ, M. R. & BERAN, P. S. 2014 State-space representation of the unsteady aerodynamics of flapping flight. *Aerospace Science and Technology* **34**, 1–11.
- TAIRA, K. & COLONIUS, T. 2007 The immersed boundary method: a projection approach. *Journal of Computational Physics* **225** (2), 2118–2137.
- TCHIEU, A. & LEONARD, A. 2011 A discrete-vortex model for the arbitrary motion of a thin airfoil with fluidic control. *Journal of Fluids and Structures* **27** (5–6), 680–693.
- THEODORSEN, T. 1935 General theory of aerodynamic instability and the mechanism of flutter. *NACA Technical Report* (496).

- TOKUMARU, P. & DIMOTAKIS, P. 1991 Rotary oscillation control of a cylinder wake. *Journal of Fluid Mechanics* **224**, 77–90.
- TSAI, H. C. & COLONIUS, T. 2015 Coriolis effect on dynamic stall in a vertical axis wind turbine. *AIAA Journal* **54**, 216–226.
- VON KARMAN, T. & SEARS, W. R. 1938 Airfoil theory for non-uniform motion. *Journal of Aeronautical Sciences* **5** (10), 379–390.
- WANG, C. & ELDREDGE, J. D. 2013 Low-order phenomenological modeling of leading-edge vortex formation. *Theoretical and Computational Fluid Dynamics* **27** (5), 577–598.
- WANG, Q., MOIN, P. & IACCARINO, G. 2009 Minimal repetition dynamic checkpointing algorithm for unsteady adjoint calculation. *SIAM Journal on Scientific Computing* **31** (4), 2549–2567.
- WANG, Z. J. 2000 Two dimensional mechanism for insect hovering. *Physical Review Letters* **85** (10), 2216.
- WANG, Z. J. 2005 Dissecting insect flight. *Annu. Rev. Fluid Mech.* **37**, 183–210.
- WEIMERSKIRCH, H., CHASTEL, O., BARBRAUD, C. & TOSTAIN, O. 2003 Flight performance: frigatebirds ride high on thermals. *Nature* **421**, 333–334.
- WILLIAMS, D. R., KERSTENS, W. & QUACH, V. 2011 Drag-power measurements of a plunging wing in an oscillating freestream 3255.
- WU, J.-Z., LU, X.-Y., DENNY, A. G., FAN, M. & WU, J.-M. 1998 Post-stall flow control on an airfoil by local unsteady forcing. *Journal of Fluid Mechanics* **371**, 21–58.
- YOUNG, J. & LAI, J. C. S. 2007 Vortex lock-in phenomenon in the wake of a plunging airfoil. *AIAA Journal* **45** (2), 485–490.
- ZHANG, M., CHENG, L. & ZHOU, Y. 2004 Closed-loop-controlled vortex shedding and vibration of a flexibly supported square cylinder under different schemes. *Physics of Fluids* **16** (5), 1439–1448.